**Microfluidic biosensor devices for disease monitoring and cancer study**

*By*

***Zhiru Zhou***

*A dissertation submitted to the faculty of the*

***Worcester Polytechnic Institute***

*In partial fulfillment of the requirements of the degree of*

***Doctor of Philosophy***

*In*

***Chemical Engineering***

**April 2022**

Committee members:

Prof. Hong Susan Zhou, Primary Advisor, Chemical Engineering Department, WPI

Prof. Qi Wen, Co-Advisor and Dissertation Committee, Physics Department, WPI

Prof. Susan Roberts, Dissertation Committee, Chemical Engineering Department, WPI

Prof. Jeannie Coburn, Dissertation Committee, Biomedical Engineering Department, WPI

## ACKNOWLEDGEMENTS

First and foremost I am extremely grateful to my PhD advisor Dr. Susan Zhou and my PhD co-advisor Dr. Qi Wen for their invaluable advice, continuous support, and patience during my PhD study. Their immense knowledge and plentiful experience have encouraged me in all the time of my academic research and daily life. I would like to express gratitude to Dr. Feiyun Cui for his treasured support which was really influential in shaping my experiment methods and critiquing my results. I would like to thank my lab mates-Feiyun Cui, Minh Ho Thanh, Will Linthicum, Jiazhang Chen, Pengbo Wang for a cherished time spent together in the lab. It is their kind help and support have made my lab time a wonderful time.

I would like to thank my committee members Dr. Susan Roberts and Dr. Jeannie Coburn for the thoughtful comments and recommendations on my proposal, defense and dissertation. I am also thankful to chemical engineering department and all its staff for all the considerable guidance. I was very lucky to pursue my PhD in WPI and met with all these kind and professional people.

I would like to thank my friends who have cherished with me every great moment and supported me. Finally, I would like to thank family, for the unconditional love and support through the way, without you I will not be here.

# Abstract

With the recent advances in nanomaterials, biosensor design, and microfluidic technology, the point-of-care devices have shown a potential to revolutionize the future health care diagnostics and therapy practices.

The intelligent use of nanomaterials is predicted to solve the challenge of efficient signal capture of the recognition event and signal amplification of the biosensor. Cu-CuO nanoparticles decorated $TiO_2$ nanotubes were synthesized and fabricated as the electrode for non-enzymatic glucose sensor. The glucose biosensor showed great sensor performance such as high sensitivity, great specificity and wide linear detection range toward glucose. While nanomaterials modified electrode showed promising analytical performance, reliable and low-cost mass production of nanostructured electrode will further facilitate the real application for biosensors. A novel and simple method was proposed to prepare nanopattern in polymer-based electrode for biosensors. The repeatability of our method was better than traditional ones because of using a predefined mold. A polyurethane (PU) nanospiked gold electrode-based label-free electrochemical immunosensor for *Clostridium difficile (C. difficile)* toxin B detection was developed. The PU nanospiked gold electrode-based immunosensor showed detection limit as low as 0.5 pg/mL, good specificity and repeatability. Benefiting from its low cost and simple processing, the fabricated immunosensor can be used as a disposable electrochemical sensor for toxin B rapid detection.

Microfluidic device merged as a powerful platform for the manipulation of different chemical and physical factors, mimicking physiological microenvironment, study of cell migration and metastasis, on-chip diagnostics and monitoring. I designed and fabricated a PDMS microfluidic device for the study of vimentin effect in cell migration and cancer metastasis. Using this microchannel assay, it was demonstrated that the knockdown of vimentin decreases 3T3 fibroblast cell directional migration speed in confined microchannels, meanwhile leading-edge morphologies of 3T3 fibroblast and 3T3 vimentin knockdown cells were observed to be different during migration.

The integration of biosensors in microfluidic devices has great potential in stand-alone or hand-held systems for point-of-care diagnostics. Glycol-modified polyethylene terephthalate (PETG)-based microfluidic devices with embedded channels and gold film electrode (GFE) are developed by a one-step, low-cost, straightforward, and mass-producible method, and are sealed by a

reversible hydrophilic tape-based mechanism. The PETG/GFE device was fabricated for simultaneous detection of cytokines on chip. Mxene nanomaterial was proposed as the probe material due to its great electron transfer ability, excellent catalytic ability and good biocompatibility.

This work provides insights into nanomaterials synthesis, nanofabrication and microfabrication for microfluidic biosensor device, enhances our understanding point-of-care diagnostics platforms for disease diagnostics, cancer metastasis study and treatment, and offers a variety of diagnostics platforms for future clinical use.

# Table of Contents

# List of Figures

**Figure 3.1:** Virous receptors for electrochemical biosensors applied in infectious diseases biomarker detection and size distribution covering all the analytes in this study, including small molecular, toxin protein, virus, bacteria and fungal cells as plotted on a nanometer scale chart.

**Figure 3.2:** Schematic diagram of the soft lithography fabrication procedure for PU nanospiked electrode and schematic diagram of electrochemistry biosensor. (A) Irradiating by laser pulses, (B) Form anti-stiction coating and cast PDMS; (C) Cure PDMS and peel away from the silicon; (D) Cutting PDMS template into the special shape and fitting them into the acrylic mold; (E) Cast PU glue and cure under UV light for 40 min; (F) Peel away PU nanospikes from PDMS template; (G) Sputter 3 nm Cr and 100 nm Au; (H) Schematic diagram of electrochemical sensor.

**Figure 3.3:** FESEM images of nanospiked silicon substrates (A) and PU nanospiked gold electrode (B); all images were viewed at 35°. (C) XRD spectrum of bare PU nanospiked gold electrode. (D) CV of bare PU nanospiked gold electrode and flat PU gold electrode in 1 M KCl containing 5 mM K3 [Fe(CN)6 ]/K4 [Fe(CN)6 ], with a scan rate of 0.05 V/s

**Figure 3.4:** FESEM images of nanospiked silicon substrates (A) and PU nanospiked gold electrode (B); all images were viewed at 35°. (C) XRD spectrum of bare PU nanospiked gold electrode. (D) CV of bare PU nanospiked gold electrode and flat PU gold electrode in 1 M KCl containing 5 mM K3 [Fe(CN)6 ]/K4 [Fe(CN)6 ], with a scan rate of 0.05 V/s. (E) DPV of bare PU nanospiked gold electrode and flat PU gold electrode 1 M KCl containing 5 mM K3 [Fe(CN)6 ]/K4 [Fe(CN)6 ], with a step of 50 mV, a modulation amplitude of 25 mV, a modulation time of 0.05 s, and an interval time of 0.5 s. (F) Six times amplified DPV tests of bare PU nanospiked gold electrode.

**Figure 3.5:** Peak current comparison of PU nanospiked gold electrode (A) and flat PU gold electrode (B) based immunosensor before/after incubating with 100 pg/mL Tcd B solution.

**Figure 3.6:** DPV plots for characterizing the immunosensor construction process. Bare PU nanospiked electrode (a), cystamine dihydrochloride modified PU nanospiked electrode (b), sdAb fixed on cystamine dihydrochloride modified PU nanospiked electrode (c), BSA filling non-specific binding sites (d), after incubating Tcd B 100 pg/mL (e).

## CHAPTER 1: Introduction

Early and timely detection of biomarker have proved significant value to clinical application. It can prevent the spread of infectious disease, provide early diagnosis and clinical treatment for cancer and other diseases. Conventional diagnosis methods such as immunological methods and histopathological techniques often require high cost, long turnaround time and experienced operating personnel. These traditional assays will be difficult to operate for point-of-care diagnosis and at-home diagnosis by patients themselves. With the recent advances in nanomaterials, biosensor design, and microfluidic technology, the point-of-care devices have shown a potential to revolutionize the future health care diagnostics and therapy practices.

Biosensors have the potential to be alternative tools since they can provide fast, accurate, sensitive early detection; monitor cancer metastasis and angiogenesis; measure and analyze effectiveness of anticancer chemotherapy drugs in a non-invasive style. Among various biosensors, electrochemical biosensors possess the advantages of low cost, simplicity, easier to be miniaturized and mass fabricated. They also can be used as point-of-care (POC) devices at home or doctor's office. Extensive efforts have been devoted to developing ultrasensitive electrochemical biosensors for detection of cancer markers with high selectivity. These efforts include discovery of the bioreceptors with high specificity and affinity, design of novel redox tags to conduct multiplex bioassay and ratiometric electrochemical assay, development of signal amplifiers based on nanomaterials, and integration of electrochemical biosensors with microfluidic chips. With the recent advances in nanomaterials, biosensor design, and microfluidic technology, the point-of-care devices have shown a potential to revolutionize the future health care diagnostics and therapy practices.

### 1.1 Nanomaterials in Biosensor

The biosensor refers to an analytical device for wide range of applications such as diagnosis, drug delivery, biomedicine, food safety and environmental monitoring. An electrochemical biosensor is a sensing device that incorporates a biological sensing element and a physicochemical transducer to yield a digital electrical signal which is proportional to the concentration of analyte. In general, as it is showed in Figure 1.1, biosensors are comprised of: (A) a bioreceptor (biosensing element), to which the analyte has a highly specific binding affinity; (B) a biosurface/biointerface architecture, which provides an environment for the proper

functioning of the bioreceptor; (C) a transducer converting the physical phenomenon or chemical response resulting from the analyte's interaction with the biological element into readable signals (e.g., physicochemical, optical, piezoelectric, electrochemical, etc.). The latter can be reproducibly measured, quantified and processed (D) an associated electronics comprising of signal amplifier, signal processor and an interface, like a display, which finally allows a user-friendly visualization and evaluation of the data. During the past 20 years, numerous of research have been done within the biosensor field with large number of literatures on the topic of "ultrasensitive", "early detection" and "cost effective" biosensor device. These advantageous attributes are the driving force toward the design and development of an advanced electrochemical sensor, which converged interdisciplinary research areas of chemistry, material science, biomedical engineering and medical industries.

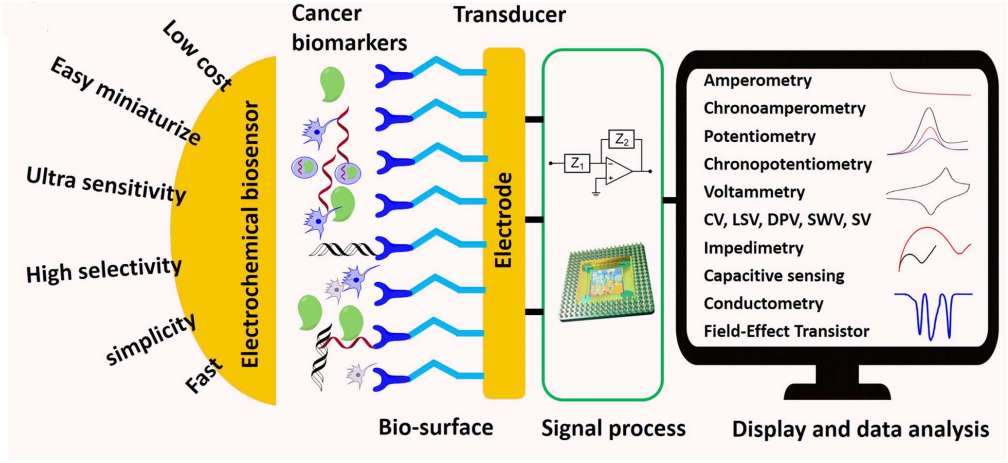


Figure 1.1: Schematic diagrams of advantages, component parts, and various measurement methods of electrochemical biosensor

Nanomaterials refers to small sized materials with size down to sub nanometer or several hundred nanometers. The controlled synthesis and tuning properties of nanomaterial make it excellent candidate to construct high performance electrochemical biosensors with a wide variety of functionality. Nanomaterials have many advantageous properties that can improve the sensitivity of electrochemical sensor and amplify the electrical signal: (1) nanomaterials with high surface areas can increase the effective reaction surface area of the electrode and facilitate the electron transfer[1] (2) nanomaterials exhibit catalytic property and can be used as electrocatalyst or redox probes to generate responding electrochemical signals[2] (3) nanomaterials

can be used as nanocarriers for receptor molecules by conjugated with biomolecules through electrostatic, hydrophobic or $\pi - \pi$ stacking interactions[3].

Nanomaterial based electrochemical sensor can be broadly classified into labeled and label-free sensor. Labeled electrochemical sensor reply on the specific interaction between the biological recognition elements such as antibody, nucleotide, enzyme[4] and the target analyte. Label free electrochemical sensor, on the other hand, directly capturing target analyte without molecular recognition element but with intrinsic redox couples or redox-active amino acids. Nanotechnology played an important role in both labeled and label-free biosensor. Gold nanoparticles (Au NPs) are mostly used in biosensing applications. AuNPs can provide a stable immobilization of biomolecules while retaining their bioactivity in labeled electrochemical biosensor[5], also it have the ability to transfer electrons between redox species and bulk electrode materials in label free electrochemical biosensor[6]. Labeled biosensor has high specificity and sensitivity because of utilizing the biorecognition reaction. Given that, no signal should be observed in the absence of an antigen-antibody interaction, but a small signal is always obtained due to the non-specific binding of other proteins on the substrate. Label free biosensor are alternatives of labeled biosensor, it mainly rely on the intrinsic redox-active properties of protein or DNA[7], or based on the hybridization reaction[8]. For instance, the voltametric oxidation potential for all four DNA monophosphate nucleotides were tested using differential pulse voltammetry[9], the result showed that the purines guanine (G) and adenine (A) can be oxidized at much lower potentials than pyrimidines thymine (T) and cytosine (C). The label-free electrochemical sensor have demonstrated improved detection accuracy and sensitivity by integrating with signal amplification strategies. To amplify signal and increase high sensitivity, label free biosensor electrodes are often modified with functional nanomaterials to amplify signal.

## 1.2 Microfluidic device for biomedical applications

Microfluidics refers to the system able to handle low amount of fluid and manipulate microscale level of fluid, meanwhile the rapid heat and mass transfer enables higher throughput and faster reaction process. Microfluidic devices can be made of various materials such as polymer, metal and silicon, depending on different biological and chemical applications. Numerous research have been made in the field of microfluidic design, modeling and fabrication method. The microfabrication process utilizes techniques in sequence to produce the desired

structure. The most important techniques are photolithography, soft lithography, film deposition and etching.

The first application of microfluidic device in biomedical field is drug delivery. Efficient and controlled drug delivery plays a crucial role in disease treatment, microfluidic device can perform as controllable platforms for precise drug delivery. Microfluidic device not only act as a reservoir to store the drug, an implantable or transdermal platform for drug delivery, but also can increase dosing range, avoid drug degradation, reduce pain and possibly increase patient adherence. Microneedle patch have been approved by FDA for clinical trials, different types of microneedles such as solid microneedles, coated microneedles, biodegradable microneedles, or hollow microneedles were developed by companies for drug delivery and monitoring. Microfluidic device is also a high-throughput screening device for drug discovery. A micron-sized bilayer lipid membranes with integrated membrane proteins and ion channels were used for ligand-binding studies[10], microelectrodes were imbedded to measure the membrane potential. By flowing or injecting lipid solution or buffer, this device can be used as a high-throughput drug screening device.

The second application of microfluidic device is for cell analysis, cell manipulation and cell sorting. As the extracellular matrix (ECM) is an important component in providing mechanical support for tissues and cells, generating cell signals that are capable of affecting cell adhesion and migration, and establishing the cellular environment[11]. *In vivo,* cells exist in a complex and information-rich three-dimensional (3D) environment that contains multiple ECM components[12]. Most research to date has been performed on 2D platforms to understand individual cellular phenomena; however, the simplicity of the 2D culture does not faithfully capture the physiological behavior of cells *in vivo*. Thus, a 3D platform will elicit a more complicated environment with physiological cues containing mechanical cues[13], adhesive cues[14], ECM-bound cues[15] and topographical cues[16]. Many bioengineering models have been built for the study of cells in 3D spaces, such as polydimethylsiloxane (PDMS) microfluidic devices[17], 3D hydrogels[18], and microcontact printed islands[19]. The PDMS microfluidic device currently has the most potential as it is capable of providing precise control[20] of mechanical, physical, chemical and topographic cues. Other than mimicking ECM and cell analysis inside microfluidic device, microfluidics can be used to detect, focus, mix, count, lyse and sort cells. Cell sorting on microfluidic device can be divided into three principle categories[21]: (1) fluorescent label-based

(2) bead-based (3) label-free cell sorting. Fluorescent label-based cell sorting relies on the fluorescent labeling of cells by immunoassay. Bead-based cell sorting relies on conjugation of cells with nanoparticles or microbeads. Label-free cell sorting have drawn a lot of interests because it is non-invasive and non-labeling process of cells. Label-free cell sorting are based on physical properties of cells such as size, shape, polarizability and elasticity, or biophysical properties of cells such as invasiveness, adherence and migration properties. Separation of cancer cells (MCF-7, MDA-MB-231 and MDA231-LM2) with different deformability was achieved using a microfluidic device with microstructure-constricted filtration and pneumatic microvalves[21]. Mixture of less flexible cells MCF-7 and flexible cells (MDA-MB-231 and MDA231-LM2) can be well separated with more than 75% purity. The device can be used to separate cancer cells from the blood sample with 90% cell recovery and more than 80% purity. Impedance measurement of cell is based on multiple discrete frequencies of AC voltage applied to cell. A microfluidic device with T-shape microchannel and two on-chip electrodes were used for discrimination of flowing cells. As cell membrane fluidity were changed with treatment of polyvinyl alcohol (PVA), capacitance of cell decreased to zero after treated with 2% PVA[22]. Deterministic lateral displacement cell sorting microfluidic device are based on cell flow differently depending on their size, shape and deformability. Microfluidic device composed of arrays of posts placed within a microfluidic channel with low Reynolds number laminar flow[23]. By adjusting rh critical size of micropost array, CTC and WBCs followed different flow trajectories. This device allows high-throughput sorting of cells with only flow interaction. Cell sorting using magnetic field is one of the most standard method for cell sorting using external force fields. Until now most of the magnetic cell sorting devices relies on the magnetic nanoparticles and antibodies conjugated with cells, which will be covered in next section in this paper. A microfluidic device with magnetic field was used to separate larger Hela cells from smaller blood cells as forces exerted on cells resulted in larger vertical deflection[24]. Label-free magnetic cell sorting is based on the inherent magnetic properties of cells. For example, white blood cells behave as diamagnetic microparticles in blood, while red blood cells can exhibit diamagnetic or paramagnetic behavior depending on whether they are oxygenated or deoxygenated[25].

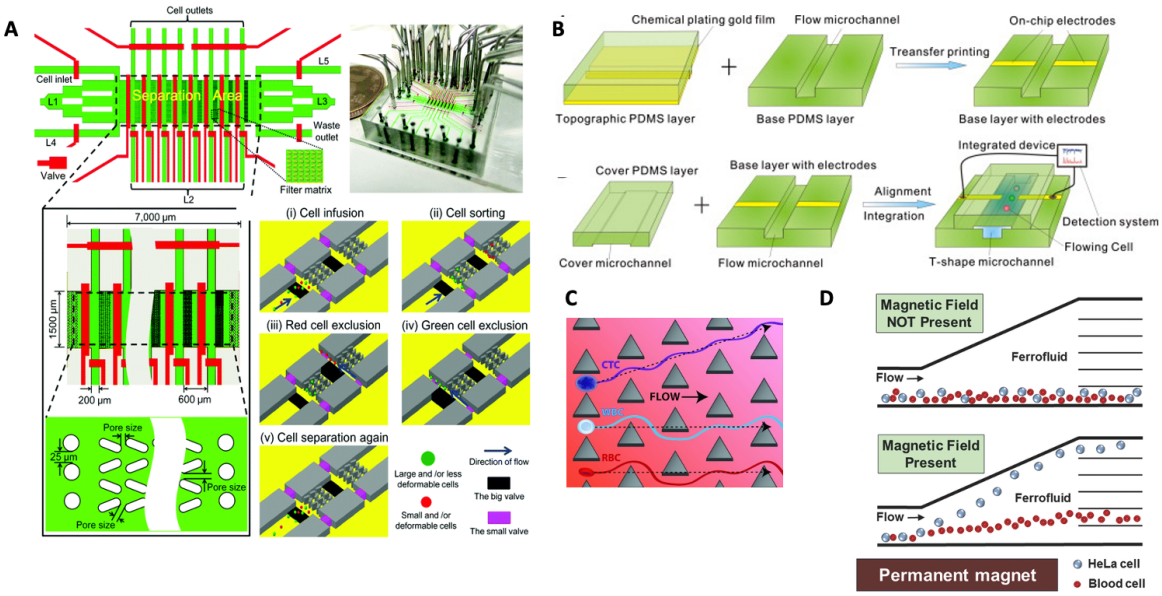


Figure 1.2: Review of microfluidic device for biomedical applications. (A) Cell sorting based on size and deformation: the cell sorting device contains three main parts: cell infusion, cell sorting and cell exclusion. A separation area (1500 μm wide, 25 μm high and 7000 μm long) with funnel-like filter matrices was designed and fabricated for cell sorting[21] (B) Cell sorting based on impedance: the cell sorting device contains a T-shape microchannel and a pair of integrated gold electrodes located horizontally on each side of microchannel. Electrical signals of flowing-through cells were detected by connecting the gold electrodes to a resistance and capacitance measurement system[22] (C) Cell sorting based on deterministic lateral displacement: A microfluidic device with deterministic lateral displacement triangular microposts arrays capable of separating CTC from blood cells[23] (D) Cell sorting based on magnetic field: When magnetic field are applied, larger HeLa cells are deflected from their laminar flow paths toward upper outlets by magnetic buoyancy forces[24]

## 1.3 Lab-on-chip Technology and microfluidic biosensor device

A microfluidic biosensor device is an integrated, downscaling biosensor device that is constructed by incorporating electrochemical electrodes into microfluidic systems. The integration of biosensor with microfluidics converts it into an efficient miniaturized alternative to conventional laboratory analysis and point-of-care (POC) diagnostic. The microfluidics technology reduces sample volume, allows continuous sampling and sample treatment, allows

real-time and simultaneous analysis on a single platform. Given that advantages, microfluidic devices have been combined with different detection techniques to produce different types of readout including optical, magnetic, electrical, distance and temperature readout. Below is a figure adapted from a review paper[26], which summarized the signal transduction and output methods in microfluidic-based biosensing. Among these detection methods, electrochemical detection is an ideal technique to be integrated with microfluidic system as the biosensor electrode fabrication technology shows great compatibility with microfabrication technology.

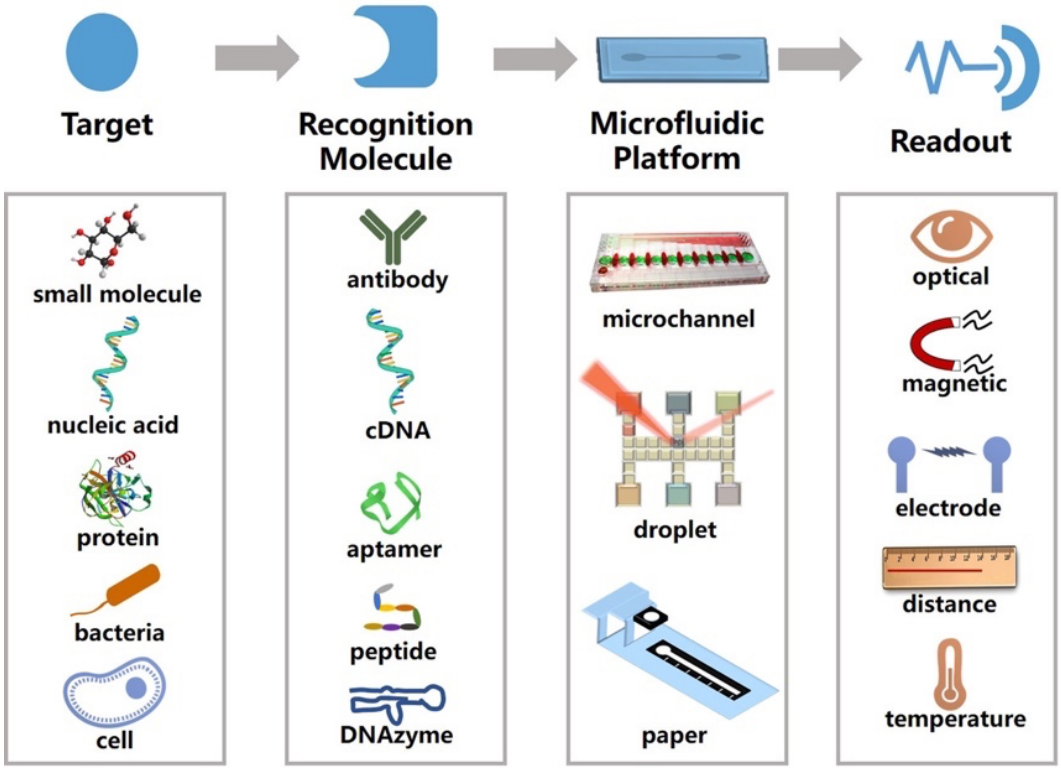


Figure 1.3: Schematics of different parts of microfluidics-based biosensor including biological recognition element, microfluidic device and signal readout. Adapted from [26]

Microfluidic combined with nanotechnology can promote electrochemical biosensor analytical performance. A microfluidic-multiplexed platform that integrates electrochemical sensors for detection of pathogenic viral DNA and genomic DNA was developed by Zribi et el[27]. By operating the fluidic device under high flow (150 µL/min), the formation of a very thin

depletion layer at the sensor surface enhanced the capture rate compared to capture rate in a static regime without flow, thus enhancing the detection limit of the electrochemical sensor from picomolar to femtometer. Moreover, the microfluidic device working under high flow allows selective direct detection of genomic DNA. Integration of microfluidic paper-based analytical devices with electrochemical sensor can allow for detection of different compounds with high accuracy in a simple way. A electrochemical paper-based microfluidic device was applied for simultaneous detection of uric acid and creatinine in human urine samples[28]. The working electrode was divided into two spots, spot 1 surface was modified with graphene quantum dots for direct uric acid oxidation while spot 2 surface was modified with graphene quantum dots, creatininase enzyme and a ruthenium electrochemical mediator to creatinine oxidation. A droplet-based microfluidic enzyme sensor for detection of glucose was developed using platinum-black (Pt-black) microelectrode. The droplet-based microfluidic system can generate concentration gradient for dose-response enzyme activity assay and glucose sensing in flowing droplets.

Biosensor incorporating microfluidic system enable it great candidate for point-of-care diagnosis and wearable sensor device. Li et al developed a multifunctional biosensor based on polyaniline (PAni)/enzyme hybrid electrode[29]. While the PAni hydrogel provide hierarchically porous, nanostructured matrices and solvated surfaces, it provides favorable molecule permeability. The sample fluid flow through microchannels to a sensing zone containing working electrodes where different kinds of enzymes were printed on the surface for simultaneous detection of various metabolites on one chip. Biosensor on soft microfluidics substrates such as fiber and paper can be used as wearable sensor. Many wearable sensors based on fiber and paper were proposed for swear glucose monitoring[30]. Due to the intrinsic good stretchability of fiber and paper material, these sensors exhibit reliable chrono and continuous for sweat glucose monitoring. Currently, there are some commercial microfluidic sweat sensors such as Epicore Biosystems and Eccrine Systems that combined colorimetric analysis and image processing technology, aiming to offer customer hydration recommendations based on detected sweat rate.

Microfluidic combining with electrochemistry can be used for many other applications other than biosensor. Jha et al[31] developed an integrated PCR microfluidic chip that incorporates an electrochemical cell lysis zone, a continuous flow PCR module and capillary electrophoresis

amperometric detection system. The PCR microfluidic chip was used for on-chip PCR amplification of SMAD4 gene from human cell lines, while the amperometric detection of guanosine was achieved by in-channel three gold electrode electrochemical system. The microchip was showed to only need 40 min in total for the whole processing (22 min for cell lysis to PCR and 15-20 min to detect PCR amplification). Meanwhile, their microchip can quantify DNA amplicons on a single analysis. Paper based microfluidic device are widely used in colorimetric analysis as it is based on color-responsive agents. Koh et al[32] developed a flexible and stretchable microfluidic device with wireless electronic interface what can bond to skin surface and connect to digital image capture hardware. Chemical analysis based on colorimetric are done on chloride ions, glucose and lactate.

## 1.4 Motivation for Research and Organization of Dissertation

Although nanomaterials have been widely used in electrochemical biosensor, there is an increasing demand and need for using biosensor for rapid analysis in matrix conditions with cost effectiveness and long-term use. We aim to develop a point-of-care system for future clinical uses by integrating electrochemical biosensor on a chip. The motivation for this dissertation is therefore to conduct a comprehensive, systematic investigation of biosensor and microfluidic device. The novelty of this work will be demonstrated by developing a new set of biosensor and microfluidic devices to understand and advance the current state of point-of-care systems. The dissertation, following this introductory chapter (chapter 1), is organized as follows:

Chapter 2: Describes a non-enzymatic glucose sensor based on the use of CuO-Cu/TNT nanomaterials. The electrode was fabricated by coating the CuO-Cu nanospheres onto the TNT array through electrochemical deposition. The CuO-Cu nanospheres with a diameter of ~200 nm are well dispersed on the TNT surface, which warrants smooth interaction and a 3D nanostructure with high uniformity. The modified electrode was then used for amperometric determination of glucose in 0.1 M NaOH solution. The glucose sensor showed great performance with a linear range as wide as from 0.2–90 mM, good sensitivity (234 μA $mM^{-1}$ $cm^{-2}$), and a 19 nM lower detection limit. The sensor is selective over ascorbic acid (AA), dopamine (DA), uric acid (UA), lactose, sucrose, and fructose.

Chapter 3: Describes A polyurethane (PU) nanospiked gold electrode-based label-free electrochemical immunosensor for *Clostridium difficile* (*C. difficile*) toxin B detection. Different

from nanomaterial-modified electrodes, the PU nanospiked gold electrode was fabricated by soft lithography directly. the PU nanospiked gold electrode-based immunosensor was developed by fixing antitoxin B single domain antibody on the electrode surface as the receptor. DPV was used as a detection technology for *C. difficile* toxin B detection. It revealed that the immunosensor has good specificity, repeatability, and stability. Even in a label-free style, the limit of detection for toxin B was 0.5 pg/mL. In the concentration range of 1–130 pg/mL, the linear regression equation $\Delta I = -1.216[C] - 41.62$ was found; the correlation coefficient $R^2$ was 0.9839. Compared with the flat PU electrode-based immunosensor, the detection signal of the PU nanospiked gold electrode-based immunosensor was amplified about 6 times. Benefiting from its low cost and simple processing, the PU nanospiked gold electrode-based immunosensor can be used as a disposable electrochemical sensor for toxin B rapid detection.

Chapter 4: Describes the design and development of a microfluidic device for cell migration study. A microfluidic device with cell culture chamber and collagen-coated microchannels was developed as an *in vitro* model for physiological confinement environments. Using this microchannel assay, we demonstrated that the knockdown of vimentin decreases 3T3 fibroblast cell directional migration speed in confined microchannels. Additionally, as cells form dynamic membranes that define the leading edge of motile cells, different leading edge morphologies of 3T3 fibroblast and 3T3 vimentin knockdown cells were observed. The leading edge morphology change under confinement can be explained by the effect of vimentin on cytoskeletal organization and focal adhesion. The microfluidic device integrated with a time-lapse microscope provided a new approach to study the effect of vimentin on cell adhesion, migration, and invasiveness.

CHAPTER 5: Describes the design and development of a polymer-based electrochemical microfluidic device, named electrochemical 6-well plate. Polyethylene terephthalate glycol (PETG) is used as a substrate and laser-cut polyester (PET) film is used as a mask for patterning the electrodes. Acrylic mold with wells (60 µL) was bonded to the PETG substrate. The results demonstrated that PETG can be an excellent substrate for fabricating the electrode. The electrochemical stability and morphology of the device are investigated.

CHAPTER 6: Describes the mechanical cues in tumor environment and current approaches of mimicking mechanical cues on chip. A sandwich type device was developed for vertical

confinement on MCF-10A and MDA-MB-231 cell line. qPCR analysis was done to understand the impact of physical confinement on gene expression of IL-6 and TNF-a in breast cancer cell line MDA-MB-231.

CHAPTER 7: Provides an outlook for future work, possible challenges and solutions of applying microfluidic biosensor device to clinical application.

## CHAPTER 2: Fabrication of CuO/Cu-TNT nanomaterials based electrochemical glucose sensor

### 2.1 Introduction

During the past few decades, due to the need of glucose monitoring in blood diagnosis[33], biopharmaceutical industry[34] and food industry[35], the development of a highly sensitive and selective glucose sensor with wide detection range has attracted a lot of attention. Enzymatic glucose sensor based on glucose oxidase (GO) is most widely used in the entire sensor market mainly due to its high selectivity toward glucose and the wide detection range. However, it suffers from several drawbacks such as limited durability, high cost, critical operation conditions, complicated electrode construction, and challenges in direct electron transfer. Nanozyme emerged as next generation artificial enzyme for biosensing by mimicking natural enzyme. They possess both enzymatic catalytic properties and inherent nanomaterial properties. Recently, many efforts have been devoted to explore nanozyme material as the enzyme alternatives[36]. For instance, transitional metals (Pd[37], Pt[38], Au[39], Ni[40] and Cu[41]), metal alloys (Pt-Ni[42], Pt-Au[43]), and metal oxide. Among these materials, copper and its oxide-based nanomaterials were found to mimic the enzymatic properties of GOx and showed great electrochemical catalytic properties toward glucose detection. The composite material of nanostructured copper oxide (CuO and $Cu_2O$) and Cu was found to promote the redox reactions due to multiple valences and redox couples on the surface oxide layer. Meanwhile, as the inherent conductivity of copper oxide is very poor, electrode based on copper oxide only is not favorable for the charge transfer, introducing metallic Cu can facilitate electron transfer of electrode. Thus, catalytic nanoparticles combining both Cu and copper oxide can help promote the electrochemical glucose sensing and increase conductivity. Titania ($TiO_2$) nanotube arrays are excellent candidates to serve as supporting matrix for loading catalytic metal/metal oxide nanoparticles due to its large specific surface area, excellent thermal stability and biocompatibility. Its vertically aligned nanostructures not only facilitate catalysts absorbed onto the surface of $TiO_2$ nanotubes but also promote rate of electron transfer. Other than the selection of material, the morphology of assembled nanozyme in terms of shape and size is another contributing factor. It was found that an electrode consisting of homogeneous particle contributed to electrochemical properties by forming a regular network. Well-ordered nanostructured anode materials can reduce the diffusion length of $Li^+$ and improve the cycling performance for lithium-ion battery.

Current nanozyme based glucose sensors show major drawbacks of linear range outside physiological range and poor selectivity to glucose in presence of other sugars . In this paper, we successfully fabricated Cu-CuO/$TiO_2$ nanozyme by depositing the Cu-CuO nanoparticles onto $TiO_2$ nanotube arrays surface through electrochemical deposition method, which is easy to operate and is a fast procedure. The Cu-CuO modified electrode were then used as the working electrode, while Ag/AgCl as reference electrode and Pt wire as counter electrode. The electrochemical properties of the electrode toward glucose oxidation were studied under alkaline condition in 0.1M NaOH solution. The sensor exhibited a wide linear range between 0.2-90 mM with high sensitivity of 234 μA $mM^{-1}$ $cm^{-2}$ toward glucose sensing. This wide linear range is very promising in real application as blood glucose concentrations are typically in the range of 4.9-6.9 mM for healthy patients, increasing to up to 40 mM in diabetics after glucose intake; Moreover, glucose concentration can increase up to 80 mM for biopharmaceutical industry. In light of this information, the proposed nanozyme based glucose sensor has great potential for continuous monitoring of glucose in most clinical and biopharmaceutical applications.

2.2 Preparation of CuO-Cu/TNT electrode (CuO-Cu/TNT)

Vertically oriented TiO2 nanotubes arrays were synthesized on the surface of Ti alloys by electrochemical anodization. It is a low-cost method which allows direct control of nanotube size with a great reproducibility. CuO-Cu nanoparticles were deposited onto $TiO_2$ nanotubes by two-step electrodeposition method. Cu nanoparticles were first electrochemically deposited onto the TiO2 nanotubes array using the constant-potential film-plating technique and then oxidized *in situ* into CuO nanoparticles by the cyclic potential sweep technique.

2.2.1 Synthesis of TiO2 nanotubes array (TNT)

Preparation of $TiO_2$ nanotube array (TNT): A sheet of titanium (99.7% trace metals basis, Aldrich) was cut into several small foils with the size of 2.5 cm by 2 cm. Then the foils were polished manually with sandpaper (220-400-800 assorted grit, 3M Wetordry) for 30 minutes and cleaned sequentially with methanol, acetone, ethanol, and deionized water (DI water) using an ultrasonic cleaner for 15 minutes each. After that, 5 mL of DI water, 15 mL of 70% $HNO_3$ acid, and 5 mL of 50% HF acid was mixed to make 25 mL of HF/$HNO_3$ mixed acid (1:3:1 ratio in volume). The cleaned titanium foils were then immersed into the mixed acid for 15 seconds and rinsed by DI water.

3.351 g of $NH_4F$ solid was dissolved in 270 mL of ethylene glycol and 30 mL of DI water (1 wt% $NH_4F$ in ethylene glycol electrolyte containing 10 vol% of water) to make the electrolyte solution for anodization. A piece of cleaned Ti foil and a platinum mesh (1.5 cm × 2 cm) were carefully immersed in parallel into the electrolyte to form a two electrodes electrochemical cell and connected to a direct current (DC) power supply station (DCS80-13E, Sorensen). Ti foil was anodized under different pairs of voltages and times under stirring (reaction area: 1.5 cm × 1.5 cm). The attempted voltage range was between 20 V and 30 V, and anodizing time varied from 20 to 100 minutes. The anodized foils were rinsed with DI water. Finally, the final foils were annealed at 350 ºC for 1.5 hours and then cooled naturally to room temperature.

2.2.2 Electrodeposition of CuO-Cu nanoparticles

CuO-Cu NPs were deposited onto the $TiO_2$ nanotube array electrode through a two-step electrodeposition method. A constant potential of -0.37 V was first applied to the $TiO_2$ nanotube in a solution of 50 mM $CuSO_4$ + 0.5 M $H_2SO_4$ for 100 s to deposit Cu first. Then, the electrode was scanned in 0.1 M NaOH with cyclic voltammetry (CV) under the potential range of -0.5 to 0.3 V at 100 mV $s^{-1}$ for 10 cycles to allow the partly oxidization of Cu to CuO nanospheres.

2.3 Characterization of CuO-Cu/TNT

The structural and morphological information were carefully studied by XRD and SEM. Figure 2.1 A and B shows the XRD patterns of $TiO_2$ nanotube arrays and CuO-Cu nanospheres deposited $TiO_2$ nanotubes respectively. The observed diffraction peaks can be assigned to Cu, CuO, anatase $TiO_2$ and Ti substrate. The diffraction peak at 25.4° can be easily indexed to the (1 0 1) plane of $TiO_2$ anatase phase (JCPDS card NO.21-1272), while peaks at 40.3°, 53.1°,63.0°, 70.8° and 76.4° can be attributed to Ti substrate. After electrodeposition, Peaks density at $2\theta$ = 35.5°, 38.4° is much higher, which is corresponded to CuO crystallites (JCPDS card no.65-2309 and JCPDS card NO.44-0706). Aside from that, peaks at $2\theta$ = 43.5° , 50.5° attributed to the (111) (200) planes of Cu with cubic phase (JCPDS card NO.04-0836). Thus, the presence of CuO-Cu was confirmed in the sample after deposition.

The morphology of bare $TiO_2$ nanotube arrays and CuO-Cu/TNT are characterized by SEM and displayed in Figure 2.1C and D. $TiO_2$ nanotubes with a diameter of ~100 nm formed a smooth supporting substrate surface. After the electrodeposition, CuO-Cu nanospheres with a diameter ~200 nm was well dispersed on TNT surface, forming a 3D nanostructure with high uniformity.

The intimate interface between the highly electrocatalytic material (CuO-Cu) and conductive supporting substrate $TiO_2$ nanotubes array (TNT) for electron transfer reactions in the electrode, thus increasing current signal in the electrode. The uniform 3D nanostructure may lower the adsorption of the intermediates after oxidation, which possibly leads to a larger detection range.

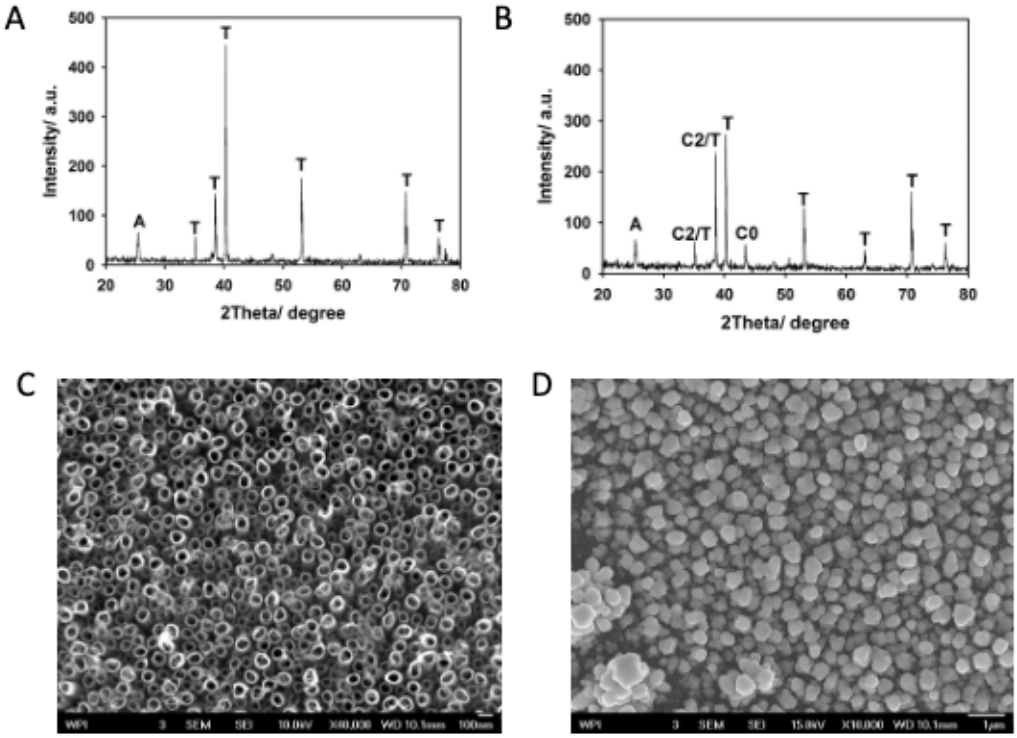


Figure 2.1: XRD pattern of (A) $TiO_2$ (B) CuO-Cu/TiO2. SEM images of (C) $TiO_2$ nanotubes (D) CuO-Cu nanospheres decorated $TiO_2$ nanotubes

## 2.4 Electrochemical performance of fabricated CuO-Cu/TNT based glucose sensor

### 2.4.1 Electrochemical oxidation of glucose on CuO-Cu/TNT electrode

The electrochemical properties of Bare TNT and CuO-Cu/TNT electrode was examined by cyclic voltammetry (CV) in 0.1M NaOH at a scan rate of 100 mV $s^{-1}$. It was performed in the potential range of 0 to 0.8 V. Figure 2.2A shows the CV of bare $TiO_2$ nanotube arrays and CuO-Cu/$TiO_2$ in absence and presence of glucose. $TiO_2$ nanotubes as supporting matrix showed no electrocatalytic activity toward glucose as there is no reduction and oxidation peak observed (Line a and b). After modifying the TNT with CuO-Cu nanospheres, only reduction peak appeared in blank NaOH solution (line c) while oxidation peak appeared after the addition of glucose (line d). The reduction peak at about +0.55 V in NaOH correlates with the redox couple Cu(II)/Cu(III):

$CuO + OH^- \rightarrow CuOOH^-$, which was reported by previous researchers. After addition of glucose solution, a single oxidation peak occurred corresponding to the glucose oxidation process. The oxidation process starts at approximately +0.2 V with broad peak around +0.45 V. This may be attributed to electro-oxidation of glucose to gluconolactone catalyzed by thermodynamically unstable Cu(III) species according to previous reports. CV responses of CuO-Cu/TNT electrode with different concentration of glucose (0, 0.5, 2, 5 mM) are shown in Figure 2.2B. Figure 2.2C shows the effect of scan rate (20-100$mV/s$) of CuO-Cu/TNT in 0.1 M NaOH solution in the presence of 2 mM glucose. It was found that the current peaks of glucose oxidation increases linearly with square root of scan rate (Left inlet) in accordance with the Randles-Sevcik equation, indicating a surface-controlled electrochemical process.

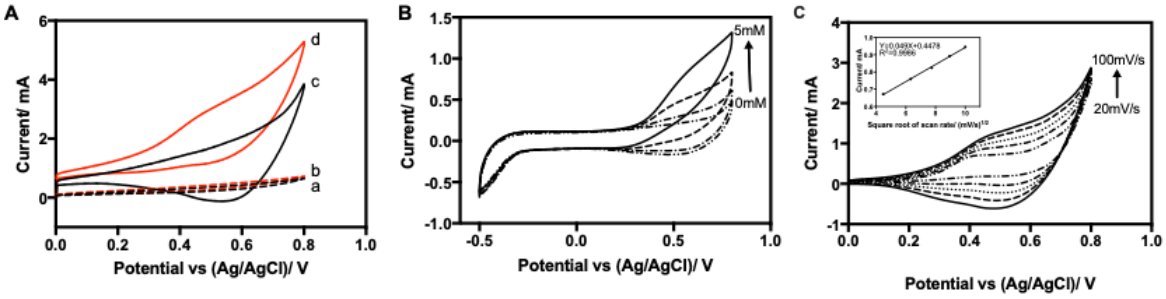


Figure 2.2: The electrochemical properties of Bare TNT and CuO-Cu/TNT electrode was examined by cyclic voltammetry (CV) in 0.1M NaOH at a scan rate of 100 mV $s^{-1}$. It was performed in the potential range of 0 to 0.8 V. (A) CV of bare $TiO_2$ nanotube arrays and CuO-Cu/$TiO_2$ in absence and presence of glucose (B) CV responses of CuO-Cu/TNT electrode with different concentration of glucose (0, 0.5, 2, 5 mM) (C) effect of scan rate (20-100$mV/s$) of CuO-Cu/TNT in 0.1 M NaOH solution in the presence of 2 mM glucose

2.4.2 Sensitivity, LOD and linear detection range

To test the analytical performance of glucose sensor, amperometric measurements were performed in 0.1 M NaOH solution with magnetic stirring. Figure 2.3A shows the amperometric response under +0.65 V with step-wise addition of glucose solution (0.2-8 mM) with an interval time of 30 s. The linear relationship between current and concentration is settled in a wide range of 0.2-90.4 mM, which is much superior to other non-enzymatic glucose sensor. Figure 2.3B shows the corresponding calibration plot (current response *versus* glucose concentration), which exhibited a linear dependence on glucose concentration (I=0.0117C+0.1391, $R^2$=0.9996). From

linear regression equation, the sensitivity(S) of CuO-Cu/$TiO_2$ is calculated as 234 $\mu$A $mM^{-1}$ $cm^{-2}$ by dividing the slope of linear calibration plot with electrode surface area. Limit of detection is calculated as 0.019 $\mu$M according to LOD = 3 $S_b$/S, where 3 is the noise to signal ratio (S/N), $S_b$ is the standard deviation of blank solution, and S is the sensitivity. The good sensitivity and low LOD may be attributed to three significant factors: (i) multi redox couples of CuO/Cu composite nanospheres improve the electrocatalytic properties (ii) the presence of Cu provides good conductivity to the CuO-Cu/$TiO_2$ electrode. (iii) High uniformity of nanostructure facilitates the mass transport of glucose onto the electrode.

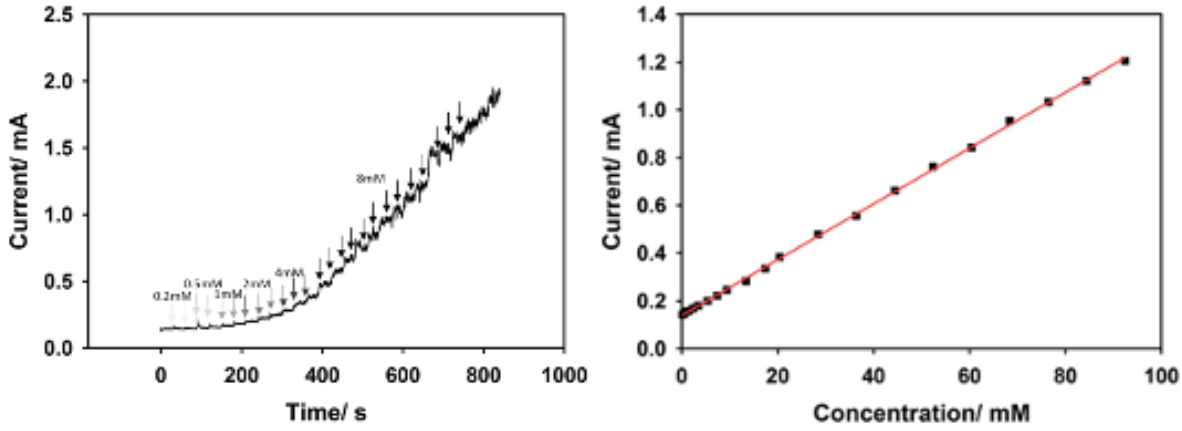


Figure 2.3: (A) Amperometric measurement of CuO-Cu/$TiO_2$ electrode responses to stepwise addition of glucose (0.2 mM-8 mM) in 0.10 M NaOH solution at potential at 0.65 V. (B) The calibration plot of the current response versus glucose concentration.

2.4.2 Selectivity and short-term stability

The selectivity of CuO-Cu/$TiO_2$ was tested with various interference species. Ascorbic acid (AA), Uric acid (UA) and dopamine (DA) are representative electroactive interferences coexisting with glucose in blood. The normal physiological level of glucose in human blood is 3-8 mM compared to about 0.1 mM of interfering species (with Glucose/interferents ratio of more than 30:1), however the Glucose/interferents ratio is much lower in food samples and biopharmaceutical industry (with glucose/interferents ratio of 10:1). In food industry and biopharmaceutical industry, there are many other sugars commonly coexisting with glucose as well. Therefore, the interference experiments were carried out by successive injection of 4.0 mM glucose, 0.4 mM Ascorbic acid (AA), Dopamine (DA), Uric acid (UA), Lactose, Sucrose, and

Fructose. According to amperometry results (Figure 2.4A), there was a vivid response of glucose while insignificant responses to interfering species. And the current response to glucose maintained consistent even after adding all the interference species. Thus, it confirms the suitability of CuO-Cu/$TiO_2$ electrode for the selective detection of glucose in presence of other easy oxidative species and sugars possibly included in blood or bioreactor. The high selectivity makes it a good candidate for both clinical application and biopharmaceutical application. The long-term stability of the sensor was investigated by measuring its sensitivity(S)/initial sensitivity($S_0$) over successivively five days, about 87% of its initial sensitivity was obtained with the fabricated electrode at the fifth determination(Figure 2.4B).

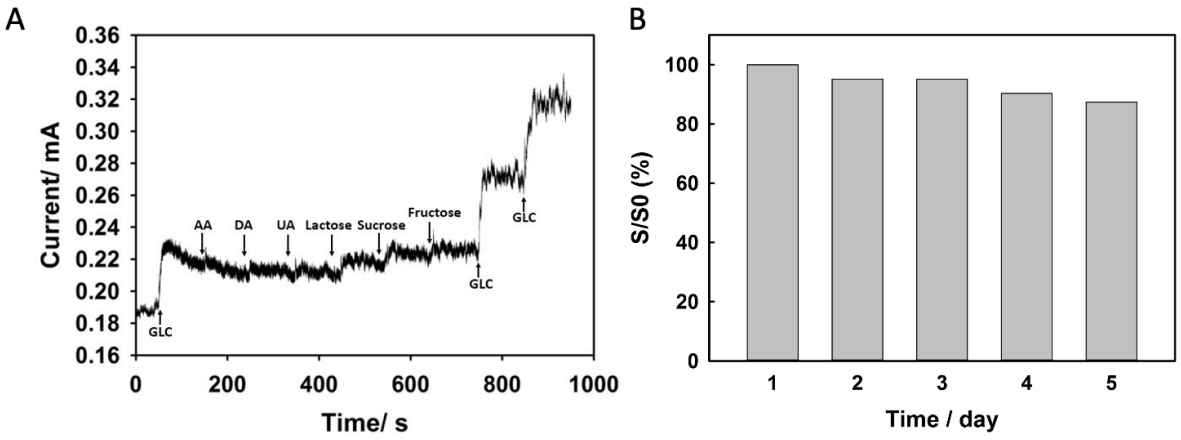


Figure 2.4: (A) Amperometric measurement of the CuO-Cu/$TiO_2$ electrode responses to successive addition of 4 mM glucose, 0.4 mM Ascorbic acid (AA), 0.4 mM Dopamine (DA), 0.4 mM Uric acid (UA), 0.4mM Lactose, 0.4 mM Sucrose and 0.4 mM Fructose in 0.10 M NaOH solution at 0.65 V. (B) Stability measurements of electrode for continuous five days

2.4.3 Reproducibility, reusability and long-term stability

Furthermore, reproducibility, repeatability, and long-term stability are also vital paramaters for nanozyme glucose sensor. To evaluate the electrode-to-electrode reproducibility, five electrode were prepared under same conditions, as shown in Figure 2.5A, a good relative standard deviation of 4.1% was achieved. The repeatability of Cu-CuO/TNT electrode was also measured with one electrode to detect 4 mM glucose five times and a relative standard deviation(RSD) of 2.12% was obtained. (Figure 2.5B). The long-term stability of the sensor was investigated by measuring its sensitivity(S)/initial sensitivity($S_0$) over successivively five days, about 87.38% of its initial sensitivity could be obtained with the fabricated electrode at the fifth determination (Figure 2.5C).

The good reproducibility, repeatability and long-term stability makes Cu-CuO/TNT applicable for practical use.

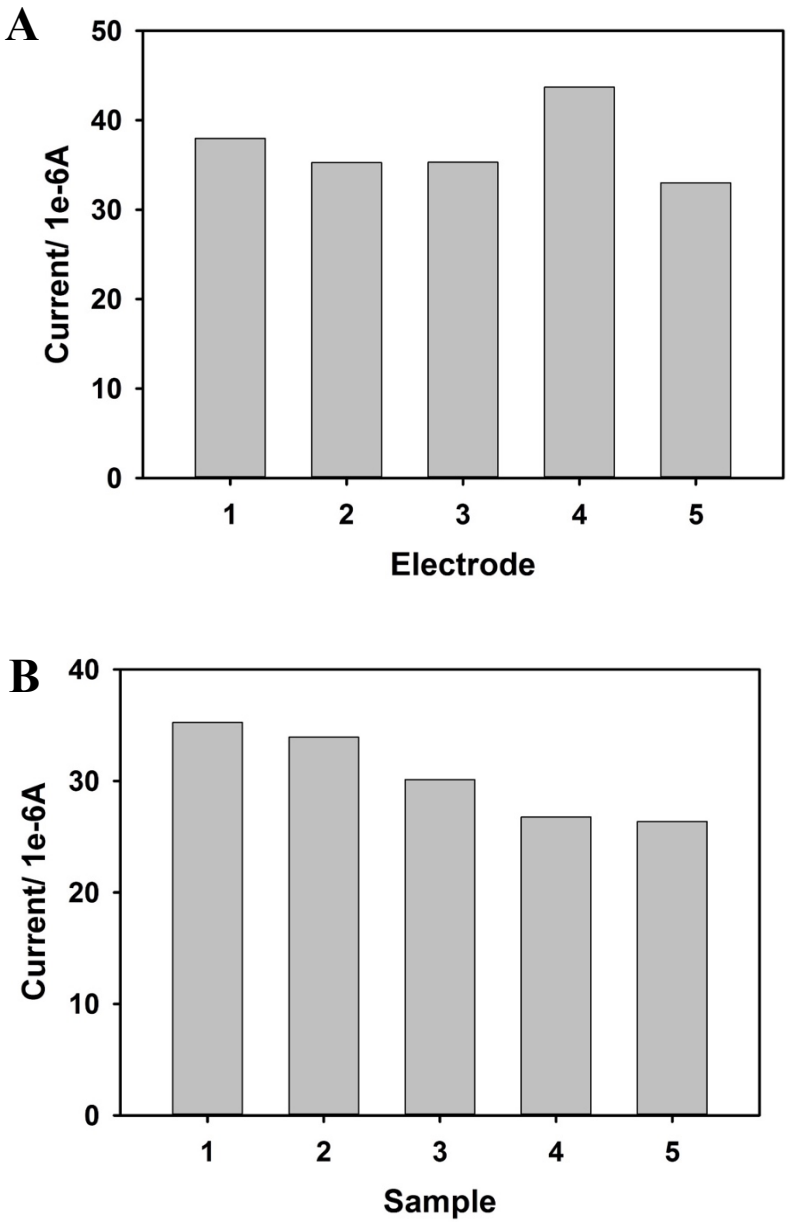

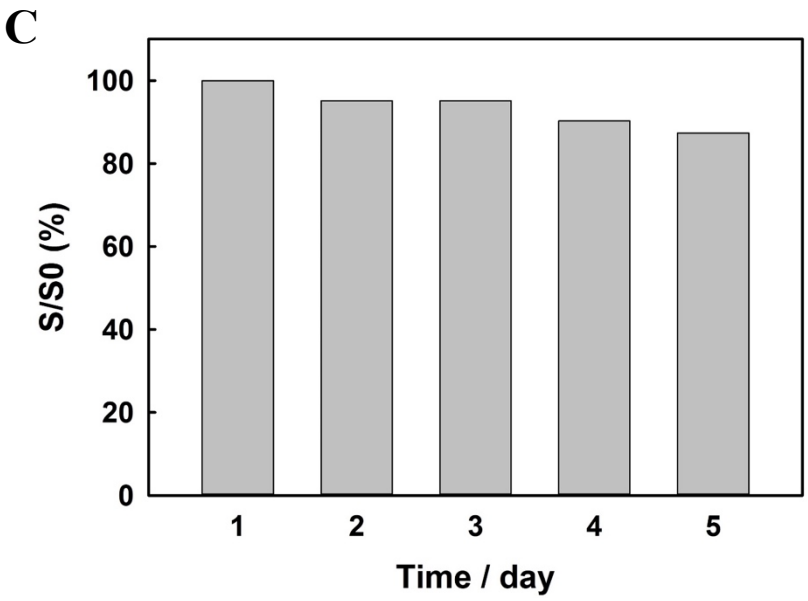


Figure 2.5: Reproducibility of five electrodes for detection of 4 mM glucose (B) Repeatability of one electrode for detecting 4 mM glucose for five times (C) Stability measurements of electrode for continuous five days

## 2.5 Conclusions

In summary, a nonozyme based glucose sensor was developed by fabricating well-alligned $TiO_2$ nanotubes with well dispersed Cu-CuO nanoparticles on it. The hiretical 3D structure of nanotubes and nanoparticles with high uniformity could facilitate electron transfer for electrochemical process . Well dispersed Cu-CuO nanospheres onto substrate generates a smooth electrode surface which could facilitate analyte glucose solution diffusion into electrocatalytic catalyst. Overall, the electrochemical performance of this electrode exhibited wide linear detection range up to 90mM with high sensitivity and low limit of detection. Meanwhile, it showed good selectivity, stability, and reproducibility. Those excellent sensing performance originate from (a) improved eletrochemical properties because of the presence of nanohybrid Cu/CuO, which possess the synergistic effect between Cu and CuO; (b) high uniformity of nanostructures which simultaneously minimizes the electron transfer resistance for elctrode and diffusion resistance between electrode and electrolyte interface. Becase of the exellent electrochemical performance,

this nanozyme glucose sensor has great potential for continuous glucose monitoring in different areas such as biopharmacuetical industry and clinical usage.

## CHAPTER 3: Disposable polyurethane nanostructured gold electrode-based immunosensor

### 3.1 Introduction

Infectious diseases can be disseminated widely by various ways. They are mainly caused by pathogenic microorganisms, such as viruses, bacteria, fungi or parasites. Despite great achievements in diagnosis, treatment, and prevention, infectious diseases remain as a serious global health threat [44, 45]. The challenges of controlling infectious diseases include irrational use of antibiotics, increase of multidrug-resistant pathogens, emergence of new pathogenic microorganisms and rapid spread owing to globalization and overpopulation [46]. Timely diagnosis and targeted antimicrobial treatment are important for successful clinical control of infectious diseases. Current diagnostic methods for infectious diseases mainly relies on laboratory-based tests including culture, microscopy, enzyme-linked immunosorbent assay ( ELISA) and polymerase chain reaction (PCR) [47]. These methods are time consuming, expensive and need to be operated by specialist. Biosensors are ideal alternative methods for timely diagnosis of infectious diseases. They have many merits such as high sensitivity, quick read-out time, easier to be mass fabricated and miniaturized. They also can be used as point-of-care (POC) devices at doctor's office or home because of their simplicity and affordable. Therefore, extensive researches have been published to report ultrasensitive electrochemical biosensors for infectious diseases detection with excellent performance.

Receptor and transducer are two main components of biosensors. The receptor recognizes the analyte specifically and the transducer converts the binding activity into a measurable signal sensitively. Electrodes are used as transducer in electrochemical biosensors [48]. Natural receptors (Figure 1), like antibody, DNA, aptamer, phage, lectin and peptide are used as receptors. They have high affinity to their targets, but huge challenges in practical applications because of their poor durability and repeatability at high temperature, pressure and in organic solvents, and also low stability in low or high pH solutions. Alternatively, molecular imprinting technique has been reported to overcome most of these drawbacks. Molecular imprinted polymers (MIPs) [49] and surface imprinted polymers (SIPs) [50, 51] have a great potential to be robust artificial receptor (also called plastic antibody) [52]. Due to its chemical and physical stability, MIPs/SIPs have provided a new insight for creating receptors by forming specific cavities for binding analytes in the polymeric matrix. In contrast to natural receptors, MIPs/SIPs offer an inexpensive, rapid,

sensitive, easy-to-use, and highly selective receptors for sensors, typically for the electrochemical biosensors. Hence, MIPs/SIPs based electrochemical biosensors have become very attractive for infectious diseases.

Several related reviews have been reported. Lahcen et al. [53] mainly presented the development of MIPs modified with nanomaterials for electrochemical biosensors. Good electrical catalytic properties and excellent conductivity of the nanomaterials combine with the comparable selectivity of MIPs endow them powerful performance for various kinds of biomarkers. The magnetic nanoparticles, carbon dots, multi/single-walled carbon nanotubes, and graphene oxides modified MIPs for electrochemical sensing were highlighted in their review paper. Origins, preparation methods and applications of SIPs applied in larger biomarkers were reviewed by Eersels and coworkers [54]. They pointed out that the measurement of larger biomarkers such as virus, bacteria, or cells met challenges when using the classical MIPs concept. SIPs can form binding cavities directly on the surface of cured polymers, thus make it easier to remove the templates and better use in larger biomarkers (Figure 3.1).

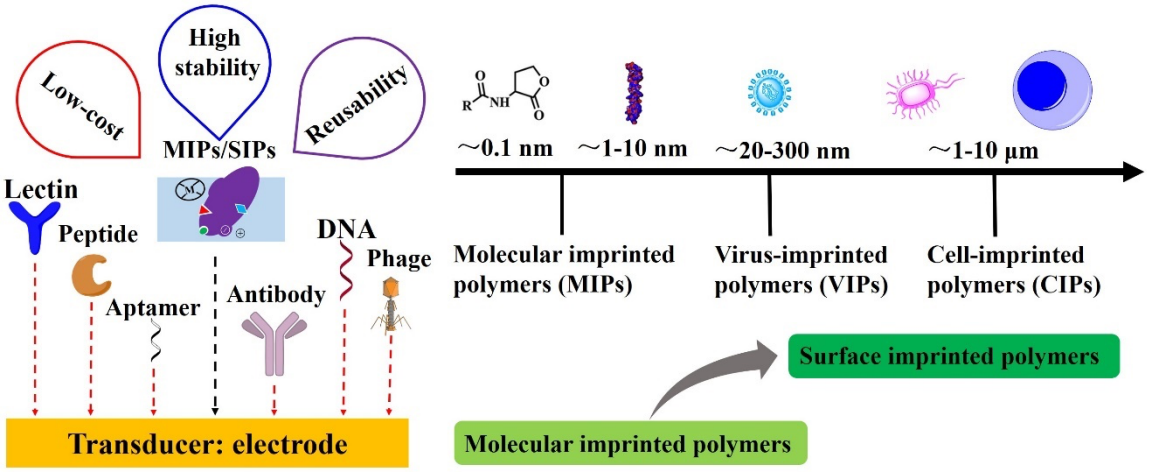


**Figure 3.1:** Virous receptors for electrochemical biosensors applied in infectious diseases biomarker detection and size distribution covering all the analytes in this study, including small molecular, toxin protein, virus, bacteria and fungal cells as plotted on a nanometer scale chart.

*Clostridium difficile* infection (CDI) is increasing globally and dramatically during past few years. It is associated with diseases ranging from mild diarrhea to severe pseudomembranous colitis resulting in colectomy and even death [55]. An U.S. prevalence survey of health care-

associated infections (HAI) found that *C. difficile* was the most commonly reported pathogen, causing 12.1% of HAI [56]. A rapid, simple, accurate, and on-site diagnosis is essential to guide treatment and to prevent transmission. It has been shown that rapid positive diagnosis is good for patient's care by reducing delays in isolation and treatment for confirmed CDI cases. A negative diagnosis will also result in rapid discontinuation of empirical therapy and isolation [57, 58]. Disease caused by *C. difficile* infection is mainly due to the effects of two large protein exotoxins, toxins A and B [59, 60]. Although detection of toxins or detection of toxigenic organisms remains controversial [55], many preliminary studies have revealed that disease severity has been correlated to stool toxin levels, suggesting that the ability to quantify toxin levels in stool could potentially be clinically valuable in predicting treatment outcomes and identifying those who need aggressive therapy.

Traditional methods for detecting toxins include cell culture cytotoxicity assay (CTA) and qualitative enzyme immunoassays (EIAs) [61, 62]. The CTA method requires 24 to 48 h of incubation, which is too long to obtain outcomes. The EIAs provide relative fast results. However, many studies showed it lacks of sensitivity [62]. Due to the above reasons, some novel ultra-sensitive *C. difficile* toxin detection approaches have been reported. Pollock and coworkers developed digital enzyme-linked immunosorbent assay for *C. difficile* toxin detection [63]. Sandlund et al reported an automated single-molecule counting technology for detecting *C. difficile* toxin A and B (Tcd A and Tcd B) [64]. Both of the methods achieved low limit of detection (LOD). Nevertheless, the approaches need fluorescence labeling, which makes the operation complicated. As we all know, electrochemical biosensors have the advantages of fast response time, high sensitivity, easy for integration and miniaturization. It has the potential to be a powerful tool for *C. difficile* toxin rapid and on-site detection. Electrochemical biosensors can be in either label or label-free style [65]. Fang and coworkers developed a sandwich-type electrochemical immunosensor for *C. difficile* toxin B detection, they used horseradish peroxidase (HRP) and HRP-Tcd B functionalized graphene oxide (GO) as label agent for signal amplification [66]. Our previous work reported a sandwich-type impedimetric immunosensor for Tcd A and Tcd B measurement, we used The  coated gold nanoparticles as label material for signal enhancement. Although both of the electrochemical biosensor achieved low analytical LOD of ≤ 1pg/ml, they are similar with fluorescence-based detection methods and have relatively complex test process.

Compared with label-based electrochemical biosensors, label-free electrochemical biosensors have the advantage of simple, low cost and no need to modify the biological samples. They have been widely developed for bioanalysis [67-70], but rarely for *C. difficile* toxin detection. In this work, we developed a label-free electrochemical biosensor for Tcd B detection. What's more, we prepared polyurethane (PU) electrodes with nanospiked surface structure as transducer. Different from mostly reported nanomaterials-modified electrode [71, 72], silicon master mold and soft lithography technology were used for preparing this type of polymer nanoelectrode. Owing to their low cost, PU nanospiked electrodes can be used for disposable electrochemical sensor.

## 3.2 Fabrication of PU nanostructured electrode

### 3.2.1 Preparation of PU nanospiked gold Electrode

Silicon nanospikes were fabricated by irradiating the surface of the silicon substrates in distilled water by femtosecond laser pulses [73, 74]. Then the nanospiked silicon substrates were used as the master mold for soft lithography [75, 76] fabrication. The schematic diagram of the procedure is shown in Figure 3.2. After rinsing in HF solution to remove the rough layer on silicon nanospikes and oxygen plasma treatment for about 5 min, the as-prepared nanospiked silicon substrates were coated trichloro(1H,1H,2H,2H-perfluorooctyl) silane in a vacuum chamber which forms a silane monolayer with low surface energy on the surface of the silicon wafer as an anti-sticking layer (Fig 3.2-A). The poly(dimethylsiloxane) (PDMS) template was made with a spin-coated hard-poly(dimethylsiloxane) (h-PDMS) (~100 μm thick) as the contact layer with the nanospiked surface, and a layer of soft-poly(dimethylsiloxane) (s-PDMS) (0 ~ 2 mm thick, Sylgard 184 Silicone Elastomer, Dow Corning) as a back layer. We cured the h-PDMS in an oven at 65 °C for about 10 min, and successively poured the s-PDMS and continued curing at 65 °C for additional 2 h. Then the PDMS template was peeled away from the silicon substrate (Fig 3.2-C). In order to make the prepared PU electrode have a fixed reaction area and match with the electrode hold (PT-3, Gaoss Union), the h-PDMS/s-PDMS templates were cut into a special shape which consists of a rectangle (length 0.82 cm and wide 0.60 cm) and a semicircle (diameter 0.54 cm). The PDMS templates were fit into an acrylic mold, and made the h-PDMS on top (Fig 3.2-D/E). The nanospiked structures were replicated on the surface of a UV curable PU polymer (NOA 73, Norland Optical Adhesives) and UV curing for about 40 min (Fig 3.2-F/G). The acrylic mold was used to make the PU nanospikes into the special shape and

control the thickness of PU to 2 mm. In our experiment, about five of PU replicas were fabricated from the same PDMS template. Subsequently, 3 nm Cr and 100 nm Au films were sputter-coated on the nanospiked PU (ATC ORION sputtering system, AJA International, Inc.). Insulating tape was used to make sure the semicircle area be fixed electrochemistry reaction area.

As a control, flat PU electrode was prepared by using same acrylic mold and sputtering same Cr/Au films.

The cleaned PU nanospiked electrode was first placed into a 30 mM cystamine dihydrochloride solution overnight and then rinsed with PBS solution to remove physically adsorbed dithiols. Subsequently, the cystamine self-assembled monolayers modified electrode was immersed into the sdAb solution (0.045 μg/μL, EDC/NHS-activated) and allowed to react at 4 °C for 3 h. After sufficiently rinsing with PBS, the electrode was dipped in a 1% BSA solution for 1 hour to block the remaining adsorption reactive sites.

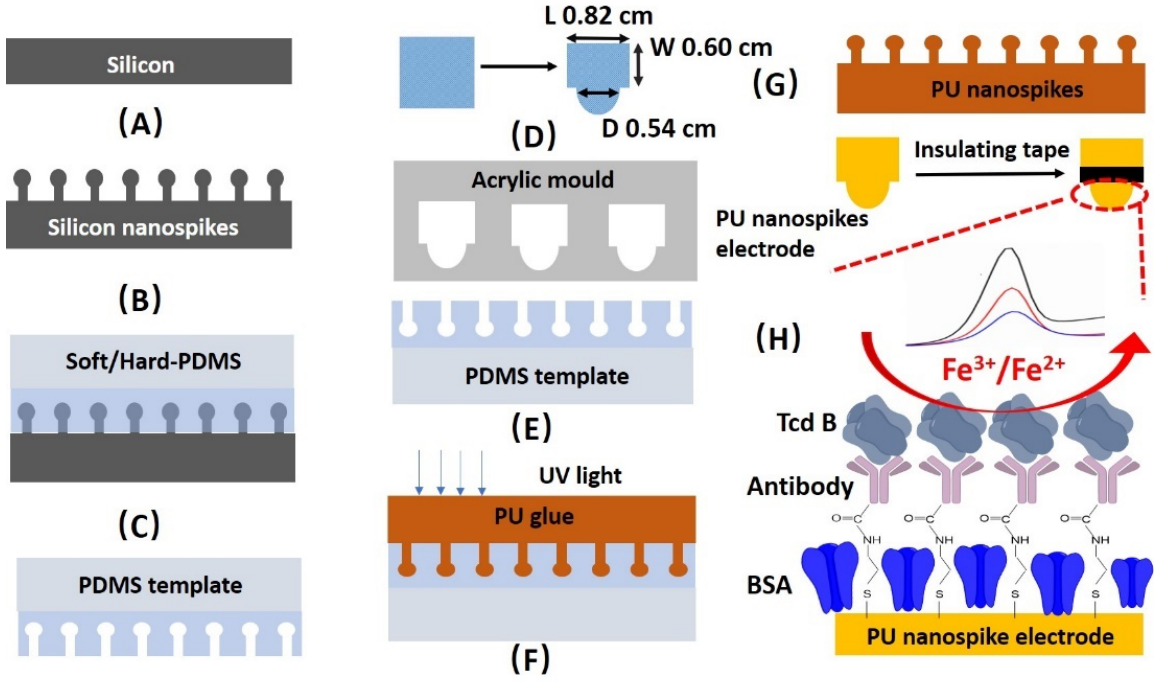


**Figure 3.2:** Schematic diagram of the soft lithography fabrication procedure for PU nanospiked electrode and schematic diagram of electrochemistry biosensor. (A) Irradiating by laser pulses, (B) Form anti-stiction coating and cast PDMS; (C) Cure PDMS and peel away from the silicon;

(D) Cutting PDMS template into the special shape and fitting them into the acrylic mould; (E) Cast PU glue and cure under UV light for 40 min; (F) Peel away PU nanospikes from PDMS template; (G) Sputter 3 nm Cr and 100 nm Au; (H) Schematic diagram of electrochemical sensor.

3.2.2 Characterization of PU nanospiked gold electrode

The morphologies of the nanospiked silicon substrates (Figure 3.3A) and the as-fabricated PU nanospiked gold electrode (Figure 3.3B) were characterized by a scanning electron microscope (SEM) (JEOL JSM-7000) with a tilted angle of 35°to the normal surface. As shown in Figure 3.3 A and B, the morphology of the PU nanospiked gold electrode and the morphology of the nanospiked silicon substrate are consistent. Both of them presented spikelike nanostructures with relatively uniform spacing. It showed our method can successfully reproduce the nanostructure of the silicon wafer surface. The elemental composition and phase structures of the PU nanospiked gold electrode were confirmed by using X-ray diffraction (XRD, Bruker AXS D8, USA). As displayed in Figure 3.3C, all the peaks can be indexed to the Au (111), (200), (220), (311), and (222) crystal faces.

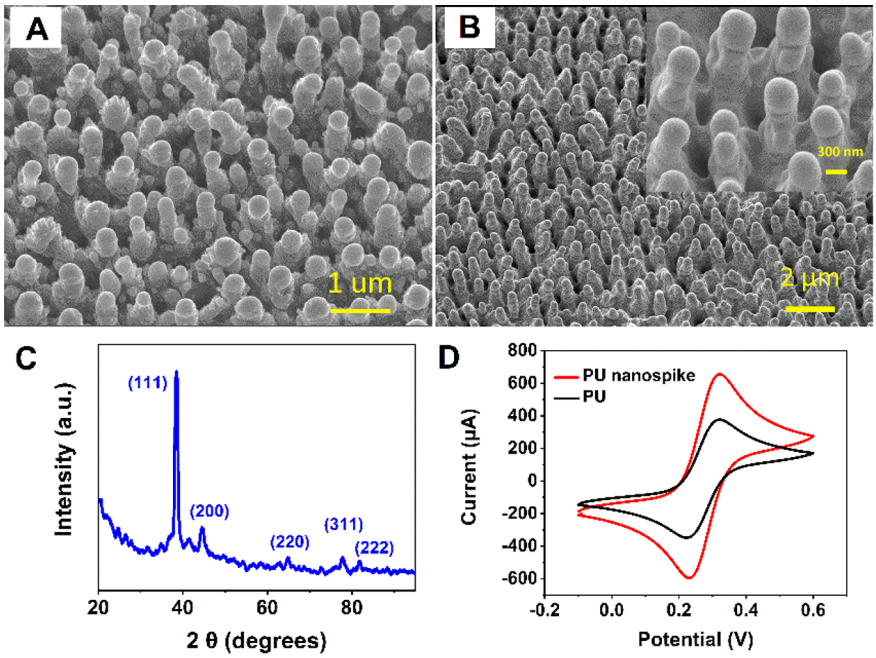


**Figure 3.3:** FESEM images of nanospiked silicon substrates (A) and PU nanospiked gold electrode (B); all images were viewed at 35°. (C) XRD spectrum of bare PU nanospiked gold

electrode. (D) CV of bare PU nanospiked gold electrode and flat PU gold electrode in 1 M KCl containing 5 mM K3 [Fe(CN)6 ]/K4 [Fe(CN)6 ], with a scan rate of 0.05 V/s

### 3.3 Electrochemical characterization of PU nanostructured electrode vs flat electrode

#### 3.3.1 Increased surface area of nanostructured PU gold electrode

Nanospiked PU electrode surface provides a higher total surface area and electroactive surface area than the flat surface. Because of an improved signal-to-background ratio, the nanospiked electrodes are electrochemically favorable to use. Thus it would be suitable for the detection of electrochemical and electrocatalytic behaviors. The electrochemical processes occurring at the electrodes were found to be linear-diffusion-driven processes, the peak current is proportional to the electrochemically active surface area.

The PU nanospiked electrode was characterized by conducting cyclic voltammogram measurement in 0.5 M $H_2SO_4$ with scan rate of 50 mV/s, scan voltage of -0.1~1.5 V. Compared with flat PU electrode, the redox peak of PU nanospiked electrode was obviously larger (Figure 3.4B). The cyclic voltammogram (Figure 3.4B) and differential pulse voltammogram (Figure 3.4C) of reversible redox couple $[Fe(CN)_6]^{3+/2+}$ in KCl solution was studied from −0.1 V to 0.6 V at a scan rate of 50 mV/s to characterize bare PU nanospiked electrode. As shown in Figure 3.4B, the current of PU nanospiked electrode was larger than current of flat PU. All of them indicate that PU nanospiked electrode had a larger active electrochemical surface area. Larger active area helps to immobilize more antibody molecules, and improve the analytical performance of electrochemical sensors, such as sensitivity, linear range, and detection limit [77]. In order to prove the stability of the PU nanospiked electrode, six groups of differential pulse voltammogram of the same electrode were continuously measured. The DPV plot shown in Figure 3.4D reveal that the prepared PU nanospiked electrode exhibited good electrochemical stability.

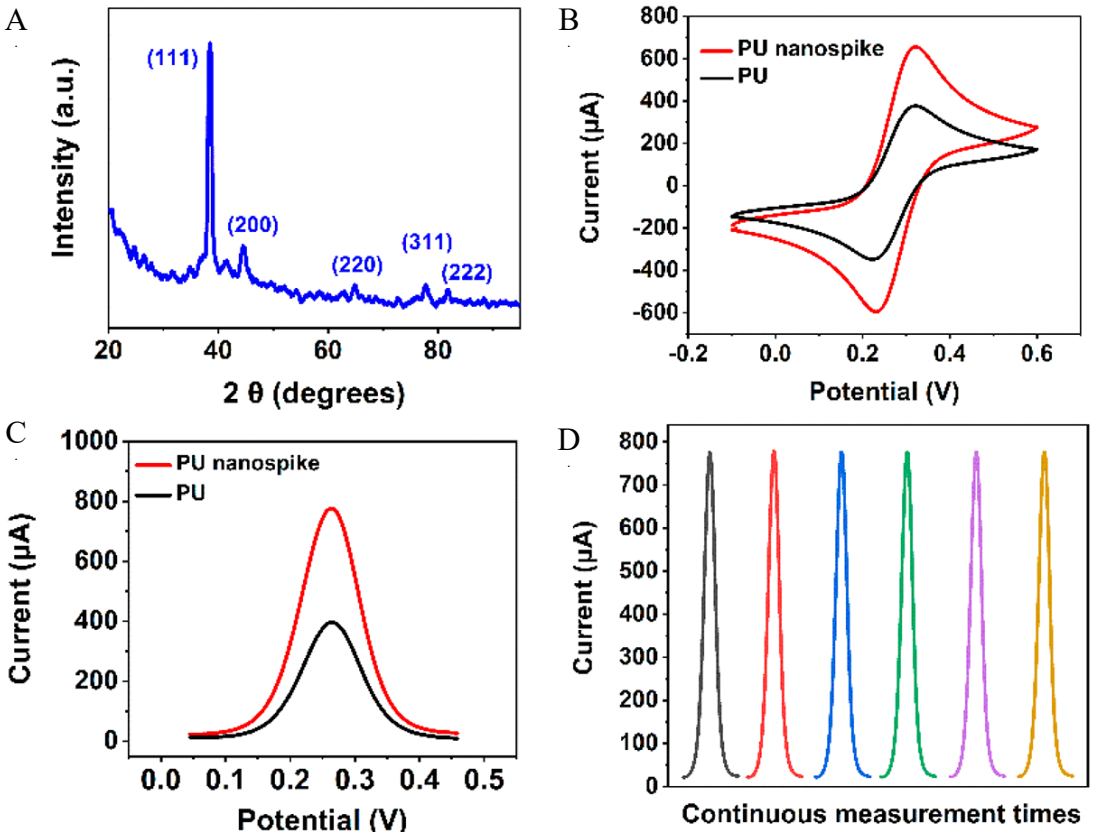


**Figure 3.4:** FESEM images of nanospiked silicon substrates (A) and PU nanospiked gold electrode (B); all images were viewed at 35°. (C) XRD spectrum of bare PU nanospiked gold electrode. (D) CV of bare PU nanospiked gold electrode and flat PU gold electrode in 1 M KCl containing 5 mM K3 [Fe(CN)6 ]/K4 [Fe(CN)6 ], with a scan rate of 0.05 V/s. (E) DPV of bare PU nanospiked gold electrode and flat PU gold electrode 1 M KCl containing 5 mM K3 [Fe(CN)6 ]/K4 [Fe(CN)6 ], with a step of 50 mV, a modulation amplitude of 25 mV, a modulation time of 0.05 s, and an interval time of 0.5 s. (F) Six times amplified DPV tests of bare PU nanospiked gold electrode.

### 3.3.2 Electrochemical Signal Amplification Effect of PU Nanospiked Gold Electrode

The nanoelectrode or nanomaterial-modified electrode can greatly amplify the electrochemical detection signal. The reaction processes on the electrode surface should become faster, and this can enhance the current signal and improve the resolution for many analytes. Here, both the PU nanospiked gold electrode and flat PU gold electrode-based immunosensor were constructed and incubated in 100 pg/mL Tcd B toxin solution. For the PU nanospiked gold electrode-based immunosensor, the peak current difference before and after incubating with Tcd B solution was

126.1 µ A (Figure 3.5A). For the PU electrode, the peak current difference was 21.46 µ A (Figure 3.5B). It showed that the detection signal was amplified about 6 times.

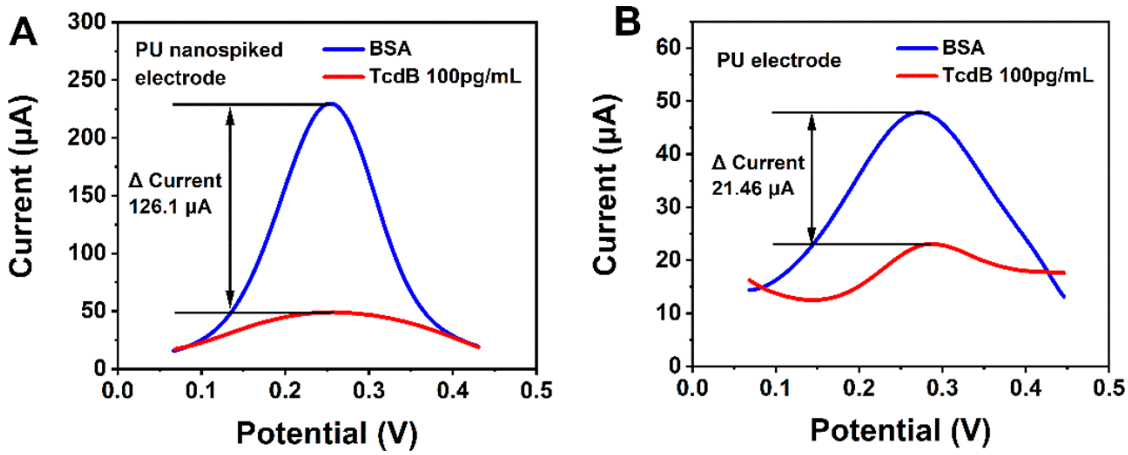


**Figure 3.5:** Peak current comparison of PU nanospiked gold electrode (A) and flat PU gold electrode (B) based immunosensor before/after incubating with 100 pg/mL Tcd B solution.

3.4 Electrochemical characterization of PU nanospiked electrode based immunosensor

DPV detection technique was used to characterize the construction process of the PU nanospiked electrode-based immunosensor. Figure 3.6 showed the differential pulse voltammograms obtained at bare PU nanospiked electrode (a), cystamine dihydrochloride modified PU nanospiked electrode (b), sdAb fixed on cystamine dihydrochloride modified PU nanospiked electrode (c), BSA filling non-specific binding sites (d), and incubating Tcd B of 100 pg/mL (e) in 5 mM $K_3[Fe(CN)_6]/K_2[Fe(CN)_6]$ redox probe solution containing 1 M KCl under identical conditions. As we can see, the PU nanospiked electrode had the highest peak current of 737.9 µA. When PU nanospiked electrode was modified with cystamine dihydrochloride and formed self-assembled monolayers (SAMs), the electron transfer of $[Fe(CN)6]^{3+/2+}$ was hindered, so the peak current decreased to 399.7 µA. In the same way, immobilization of sdAb and BSA also blocked the electron transfer, the peak current decreased to 311.6 µA and 150.1 µA respectively. At this time, the PU nanospiked electrode based immunosensor was completed. In order to confirm to the as-fabricated immunosensor can be effective for detecting of Tcd B, the immunosensors were incubated in Tcd B solutions 100 pg/mL concentrations. The results were shown in Figure 3.6e, the peak current further decrease to 24.33 µA. It revealed that Tcd B have

been successfully captured by the immunosensor. The as-fabricated immunosensor was effective for detecting of Tcd B.

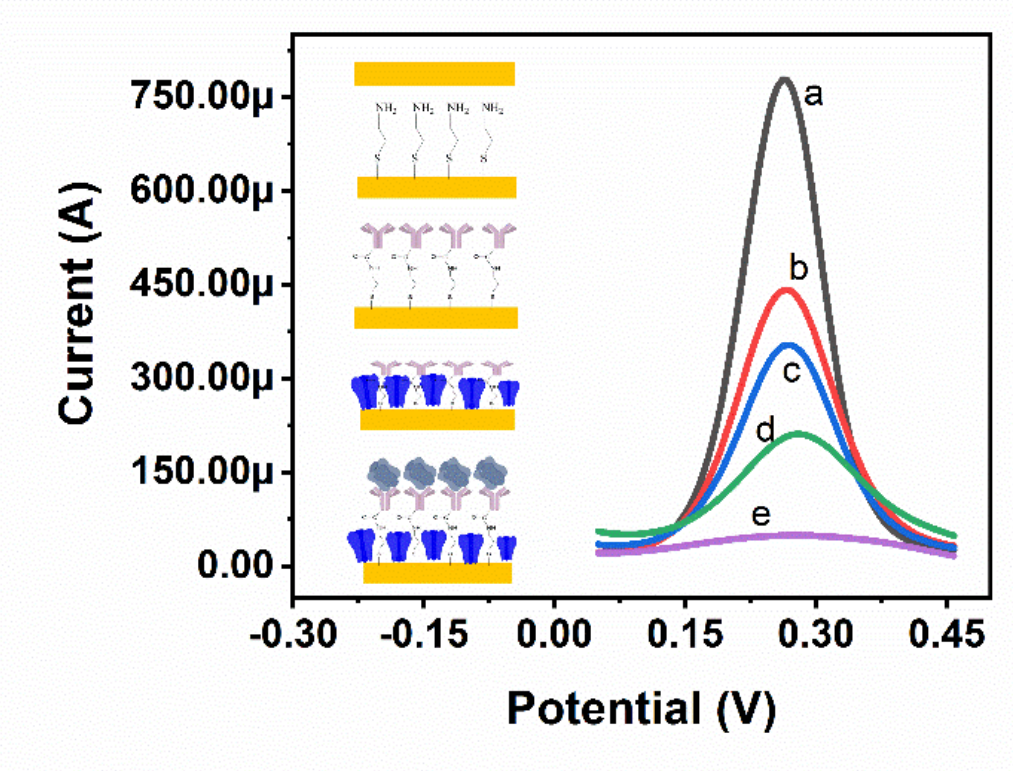


**Figure 3.6:** DPV plots for characterizing the immunosensor construction process. Bare PU nanospiked electrode (a), cystamine dihydrochloride modified PU nanospiked electrode (b), sdAb fixed on cystamine dihydrochloride modified PU nanospiked electrode (c), BSA filling non-specific bingding sites (d), after incubating Tcd B 100 pg/mL (e).

3.5 Specificity, Repeatability, Stability, and Sensitivity of the Immunosensor

Specificity is one of the most important performances of biosensors. The specificity of the PU nanospiked gold electrode-based immunosensor has been studied by testing other protein samples. All concentrations of the tested protein samples were 100 pg/mL. The incubated time was 2 h. As shown in Figure 3.7A, other protein samples such as BSA, GO (glucose oxidase), Shiga toxin 2, and thrombin only have few peak current changes, but for Tcd B, the peak current change was distinct. It demonstrated that the immunosensor possesses good specificity. The repeatability and stability of the immunosensor were also evaluated. Six PU nanospiked gold electrode-based immunosensors were fabricated; three of them were used to test Tcd B

immediately, and the other three were stored in PBS at 4 °C for 2 weeks and then were used to detect the Tcd B. The results are presented in Figure 3.7B. The peak current of the immunosensor retained 85.12% of its initial response after storage for 2 weeks. Both fresh and stored immunosensors can effectively detect the Tcd B. To investigate the sensitivity of the PU nanospiked gold electrode-based immunosensor, the peak current of the working electrode after incubating with different concentrations of Tcd B solutions was measured. Figure 3.7C shows the DPV plot of the immunosensor and after being incubated with various concentrations of Tcd B solution. The peak current change is defined as $\Delta I = I(i) - I(BSA)$ , where I (BSA) is peak current after the PU nanospiked gold electrode was incubated with BSA; it is the base signal of the immunosensor. I (i) is the peak current of the immunosensor after being incubated in Tcd B solution at different concentrations. As shown in Figure 3.7D, from 1 to 130 pg/mL, the $\Delta I$ has a good linear correlation with the concentration ([C]) of Tcd B. The linear regression equation was $\Delta I = -1.216[C] - 41.62$, with $R^2$ of 0.9839. The LOD was measured to be 0.5 pg/mL. Compared with other electrochemical biosensor for *C. difficile* toxin, this work achieve a raletively lower LOD (Table 1).

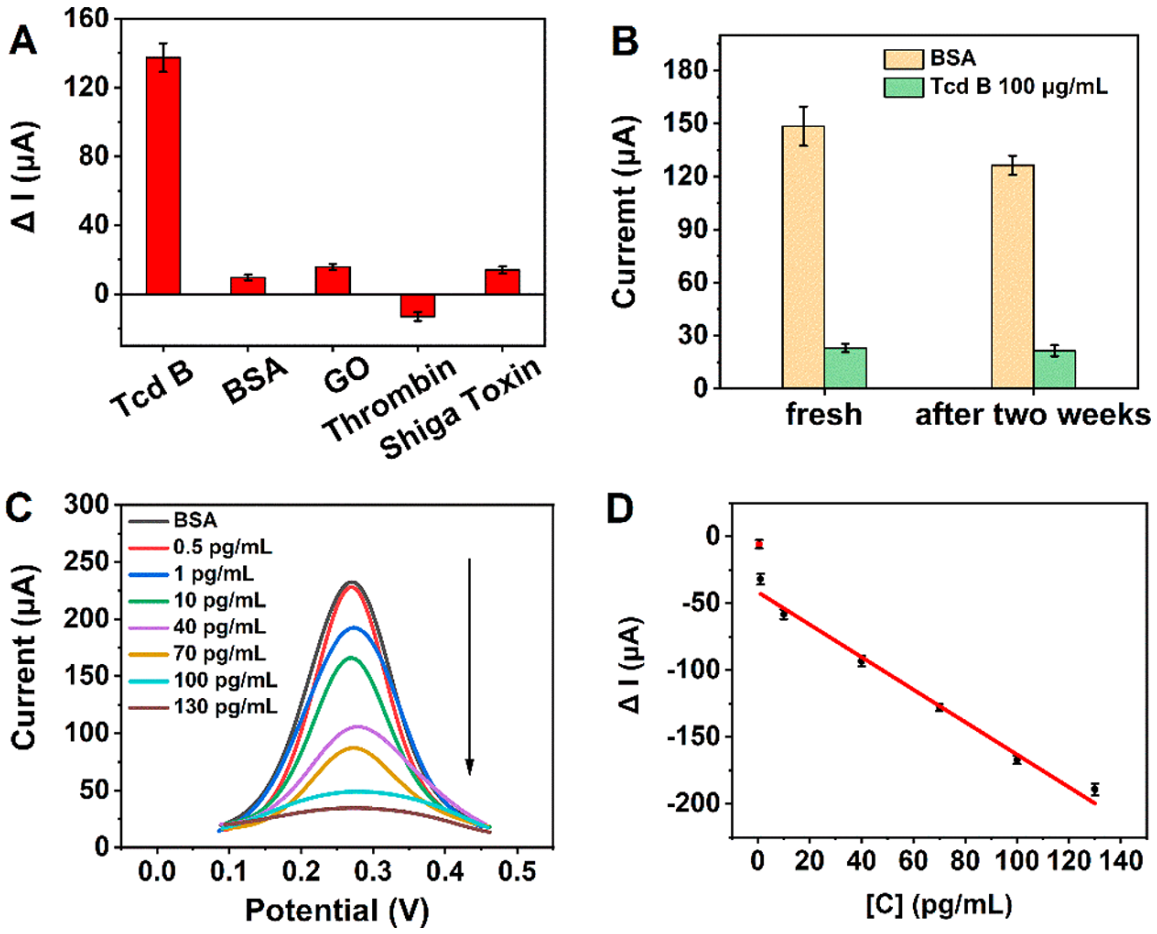


**Figure 3.7:** (A) Specificity of the immunosensor based on the PU nanospiked gold electrode. (B) Repeatability and stability of the immunosensor. (C) DPV plot of the immunosensor after incubating with different concentrations of Tcd B solution. (D) Linear regression curve of ΔI to different concentrations of Tcd B.

Table 1 Comparison of reported *C. difficile* toxin electrochemical detection methods with this work

| Method | Analyte | LOD | Reference |
|---|---|---|---|
| Differential pulse voltammetry | Tcd B | 0.7 pg/mL | [66] |

| | | | |
|---|---|---|---|
| Electrochemical impedance spectroscopy | Tcd A/B | 0.61 pg/mL for TcdA; 0.60 pg/mL for TcdB | [78] |
| Differential pulse voltammetry | Tcd B | 0.5 pg/mL | This work |

3.5 Conclusion

In this work, PU nanospiked electrodes were fabricated by soft lithography. Results of SEM, CV and DPV experiment proved its good morphology and electrochemical performance. Then, PU nanospiked electrode-based label-free electrochemical immunosensor for *C. difficile* toxin B detection was developed. DPV was used as a detection technology for *C. difficile* toxin B detection and it revealed that the immunosensor has good specificity, repeatability and stability. Although in a label-free style, the limit of detection for toxin B was 0.5 pg/ml. With the increase of the concentration of toxin B from 1 pg/mL to 130 pg/mL, a linear relationship was observed between the peak current and toxin concentration. The linear regression equation was $\Delta$ Curr = -1.219 [C]-41.40, with a correlation coefficient $R^2$ of 0.9839. The signal was amplified about 6 times compared with flat PU electrode based immunosensor. Owing to the low cost and simple processing, the PU nanospiked electrode based immunosensor can be used a disposable electrochemical sensor for toxin B rapid detection.

## CHAPTER 4: A microfluidic device for study of vimentin effect on cell migration

### 4.1 Introduction

Cell migration and motility is important for many physiological and pathological processes, such as wound healing[79, 80] and cancer metastasis[81, 82]. The extracellular matrix (ECM) is an important component in providing mechanical support for tissues and cells, generating cell signals that are capable of affecting cell adhesion and migration, and establishing the cellular environment[11]. Cell migrating in vivo experience varying degree of confinement as the ECM microenvironment offers many tracks for cell migration, including tracks along ECM fibres or blood vessels, between connective tissue and the basement membrane of muscle, in the interstitial space or in the vasculature of organs[12]. The simplicity of the 2D flat surface showed limitation to mimic the track and does not faithfully capture the physiological behavior of cell migration *in vivo*. Thus, a 3D microchannel will elicit a more complicated environment with physiological cues containing mechanical cues[13], adhesive cues[14], ECM-bound cues[15] and topographical cues[16]. Many bioengineering models have been built for the study of cell migration, such as polydimethylsiloxane (PDMS) microfluidic devices[17], 3D hydrogels[18], and microcontact printed islands[19]. The PDMS microfluidic device currently has the most potential as it is capable of providing precise control[20] of mechanical, physical, chemical and topographic cues.

The cell cytoskeleton is a group of dynamic proteins that are important for increasing cell adhesion, regulating cell shape and motility, and maintaining cell integrity. The cell cytoskeleton is composed of microtubules, actin filaments, and intermediate filaments. Vimentin is a component of type III intermediate filament protein existing in motile mesenchymal cells, including fibroblasts, macrophages[83], and metastasis cancer cells. There is evidence that vimentin is involved in the regulation of cell morphology, adhesion, and motility. Overexpression of vimentin is observed in various types of cancers including prostate cancer, lung cancer, malignant melanoma, and breast cancer, which links overexpression of vimentin to the invasiveness of cancer[84]. This correlation can be explained, as vimentin is a marker for the epithelial-to-mesenchymal transition (EMT) process[85], a process that occurs during cancer metastasis. Vimentin expression is also correlated with the wound healing process. Vimentin-knockout mice are defective in the directional migration of fibroblasts and capacity of wound healing[86, 87]. Fibroblasts from the embryos of these mice are incapable of translocation, and the reintroduction of vimentin rescues

the motility of these cells. Vimentin knockdown was shown to attenuate the migration of fibroblasts[88] and cancer cells[89, 90]. Mendez et al[91] showed in 2D experiment that expression of vimentin can induce cells to adopt a mesenchymal shape and increase motility. The roles of vimentin in cytoskeleton organization, cell morphology, and motility on flat 2D substrates have been studied extensively[91-93]. However, fibroblasts often migrate *in vivo* in an extracellular matrix that is intrinsically 3D; hence, the role of vimentin in 3D setting is less well understood.

To address how vimentin regulates cell migration in a 3D setting, a microfluidic device with constriction microchannels coated with collagen type I was designed and developed. Previous investigations reported that collagen promotes 3T3 fibroblast cell migration accompanying the production of matrix metalloproteinases (MMP) and ROS[94]. Collagen I was shown to be able to initiate human dermal fibroblast migration without growth factors[95]. Thus, we assume that a collagen coated PDMS surface may serve as a good substrate to study cell migration.

Protrusions of 3T3 and 3T3 vim- cell inside channel were also observed and studied. Protrusions of cell front are highly dynamic structures which provide sustained forward force for cell migration[96]. Migrating cells extend different types of plasma membrane protrusions[97] including lamellipodia, filopodia, blebs and invadopodia. Actin cytoskeleton and regulators activated by signaling pathways allow cells to respond dynamically to ECM environment. The mode of cell migration can be classified by the morphology of leading edge and types of structure forming the leading edge[98, 99]. There is a wide diversity in the types of protrusions, while the type of protrusion can be used to define a specific mode of cell migration.

The microfluidic device was then integrated with a cell culture chamber on a microscope, which assures that the 3T3 fibroblast cells and 3T3 vimentin- cells can be cultured and imaged inside the microfluidic device for up to 12 h. High-resolution, real-time images were captured for cell migration inside collagen-coated microchannel. Cell morphology changes and membrane fluctuations were observed under the microscope, which can provide insight into the mechanisms of the cell migration process.

### 4.2 Microfluidic device design, fabrication and operation

Microfabrication is finding increasing application to study cell migration in confined environment. The microfabricated assays include: micropatterned lines or islands, micropost assays and microchannel device. Microchannel devices have shaft-like cell culture chamber and

rectangular microchannels. Cells may be laterally confined by all four microchannel walls but free to move forwards and backwards. Early studies of cell migration in microchannels examined the effect of varying channel width on cell migration speed. Irimia et al[100] studies the spontaneous migration of MDA MB 231 breast cancer cell in PDMS microchannels with height from 3-12 $\mu m$ and width from 6-100 $\mu m$. The cell migration speed in 3 $\mu m$ height and 25 $\mu m$ width channel was highest. Microfluidic device can be designed with complex channel geometries. A microchannel decision tree was designed with semicircular pattern and circular pattern[101]. When cells encounter a 90 degree split to 10 and 3 $\mu m$ wide channels, more than 90% of the cells choose the wider channel, a trend that holds when actomyosin contractility is inhibited by application of blebbistatin. If the 3.3μm-wide channel is placed in a path collinear to the original channel, the percentage of cells choosing the wider path drops to 68% and, interestingly, to only 33% when cells are treated with blebbistatin, suggesting that actomyosin contractility has a role in environmental sensing. Because of the easy manipulation of chemical and physical gradient in microfluidic device, many studies were done to study the effect of chemical gradient[102] and voltage gradient[103] on cell migration.

4.2.1 Design of microfluidic device

Microchannels fabricated for the study of cell migration during physical confinement are typically straight, shaftlike spaces ranging in cross-sectional area from ~20 $\mu m^2$ to greater than 1000 $\mu m^2$. To model 3D cell motility, we designed microfluidic devices with micro channel width ranging from 3 $\mu m$ to 20 $\mu m$. The channel height was designed to be 10 $\mu m$ to impose cell in 3D wall environment. Microchannels are designed mainly to mimic *in vivo* confinement environment, meanwhile the channels enabled convenient diffusion of oxygen and nutrients for 3D cell culture on chip. Porous artificial ECM scaffolds can be created to promote cell adhesion and growth. By surface coating with ECM proteins such as collagen, fibronectin, and laminin, biomimetic scaffolds with superior effectiveness for cell seeding and distribution can be attained. Thus, the PDMS channels were precoated with collagen I before cell seeding and cell behavior were compared between PDMS non-coated channel and collagen-coated PDMS channel.

4.2.2 Fabrication of PDMS microfluidic device

Photolithography, also called UV lithography, generates desired pattern on substrate surface through exposure of regions of light-sensitive material to ultraviolet (UV) light.

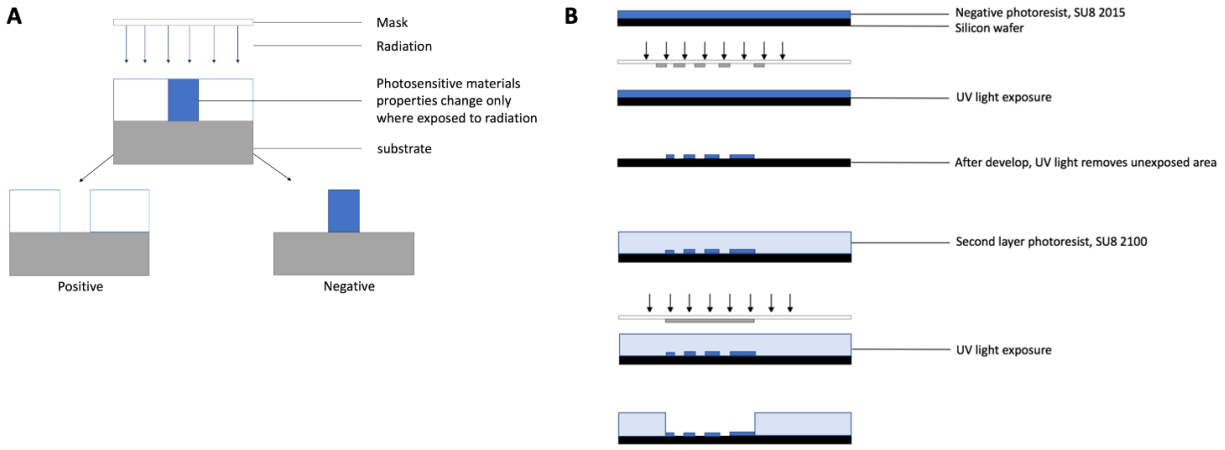


**Figure 4.1:** Photolithography process (A) positive and negative photoresist (B) Photolithography process of negative photoresist

As it is shown in the Figure 4.1A above, two types of photoresist (positive and negative photoresist) will undergo two transformations upon exposure to light. When light illuminates a positive photoresist, the exposed region break down and further be removed by photoresist developing solution. A negative photoresist, on the other hand, becomes crosslinked upon exposure to UV light, thus the part not exposed to light will be removed. Figure 4.1B is showing the photolithography process using SU-8 negative photoresist. In the first step, substrate silicon wafer is coated with a layer of photoresist. Then a photomask patterned with opaque material and desired design was placed on top of the substrate and photoresist, followed by irradiation of UV light. The unexposed area then can be removed with a developing solution. The SU-8 photoresist material shows stable mechanical, thermal and chemical characteristics, it can be patterned to make microstructures with high aspect ratio. Photolithography was widely accepted for microfabrication because of the high resolution down to 2 μm, especially for many biomedical applications. However this technique requires clean room facilities which makes it less accessible.

Soft lithography is a rapid prototyping approach to transfer pattern to microscale and nanoscale structure and to fabricate devices on planar, curved and flexible substrates. Soft lithography patterning techniques includes microcontact printing ($\mu$CP)[104], replica molding (REM)[105],

microtransfer molding[106], solvent-assisted micromolding (SAMIM)[107], phase-shifting edge lithography[108], nanotransfer printing[109] and decal transfer lithography[110]. Current stage of soft lithography usually relies on the master fabricated by photolithography. Once the master is available, most of the soft-lithography fabrication can be done without cleanroom set up.

The fabrication of a microfluidic device usually combines the photolithography and the soft-lithography technique, Figure 4.2 below outlines the four major steps.

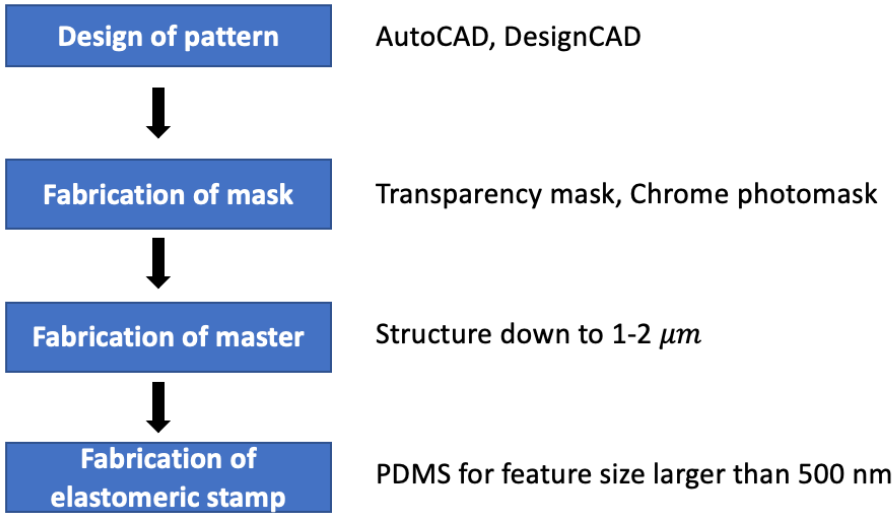


**Figure 4.2:** Fabrication process of a microfluidic device

Fabrication of master is the most critical step in the fabrication process. The writing step using EBL system usually take 2-4 hours depending on the pattern feature, exposure time, size of writing field and density of writing objects. Microfabrication technique enabled great control of size, morphology, topography and functionality of the devices. Because of the great biocompatibility and transparency of the PDMS material, the PDMS microfluidic device have been able to contribute immensely to cell biology field.

In our experiment, PDMS microchannels were fabricated using standard photolithography and soft-lithography process. The microchannel design was first drawn by AutoCAD, then the pattern was transferred to a chrome-on-glass photolithography mask (Advance Reproductions Corp). To prepare masters, SU-8 2010 and SU-8 2100 epoxy-negative photoresists (Microchem Corp.) were applied by spin coating (Laurell Technologies Corp.) onto silicon wafers in two steps. The first layer of SU-8 2010 was spread at 3500 rpm for 30s with acceleration of 300 rpm/second to a final thickness of 10 µm. The SU-8 2010 photoresist

was prebaked at 95 °C for 2 min, exposed to 145 mJ/cm$^2$ UV radiation through a chrome mask for 7 s, post-baked at 95 °C for 4.5 min and subsequently developed using SU-8 developer for about 3 min. The silicon wafer was then dried with first layer pattern using pressurized inert gas. The second layer of SU-8 2100 was then spread onto the wafer at 2200 rpm for 30 s with acceleration of 300 rpm/second. The wafer was prebaked at 65 °C for 5min and 95 °C for 15 min. After exposure, the wafer was post baked at 65 °C for 4 min and 95 °C for 10 min, and subsequently developed with SU-8 developer for 9 min.

After completing the steps, the silicon wafer photomask was fabricated and to be used for the following PDMS soft lithography. PDMS solution mixer was obtained by mixing prepolymer (Sylgard 184) with cross-linker (Dow Corning) in a 10:1 ratio (by weight), then poured onto the as fabricated silicon wafer. After degassing in vacuum for 1h, it was incubated at 80 °C for 1 h. After the curing process, the PDMS device can be peeled off the silicon wafer and bonded to a glass slide using oxygen plasma. Right after the oxygen plasma treatment, it was flushed with a solution of 70% (vol/vol) ethanol in deionized water (di$H_2O$), followed by rinsing with sterile di$H_2O$ for sterilization. Channels were then rinsed with phosphate buffered saline (PBS) and coated with surface ligands by pumping in 10 μg/mL solution of collagen I (BD Biosciences, Franklin Lakes, NJ) in PBS and incubating for 1 h at 37 °C. Channels were then washed 3× with PBS, filled with cell culture media, and incubated at 37 °C for at least 30 min before seeding cells. The images of microchannels were captured by a 20X microscope (Figure 4.3B), which confirmed the channel widths of 5 μm and 10 μm, and channel length of 50 μm.

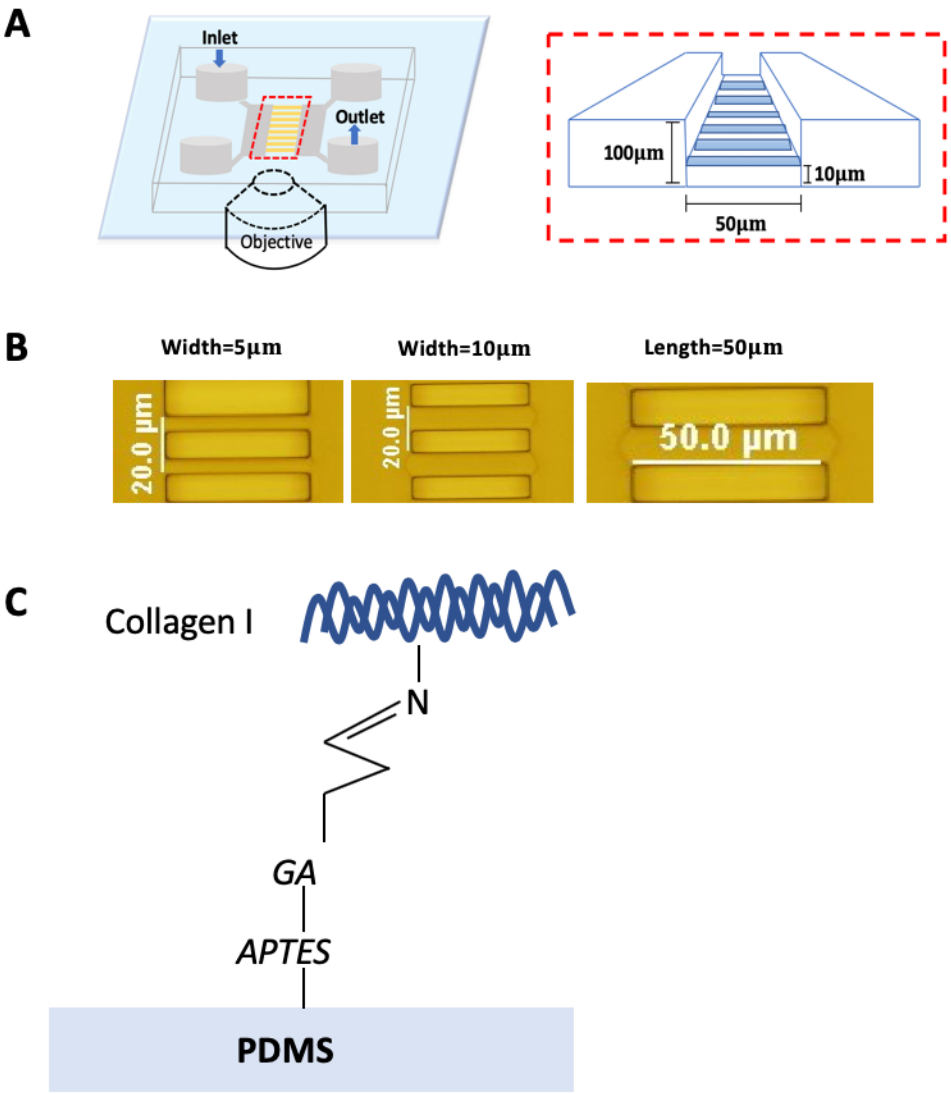


**Figure 4.3:** (A) schematics of microfluidic device (B) microscope images of microchannels (C) schematic diagram of collagen immobilization on PDMS surfaces

4.3 Cell migration study inside the as-fabricated microfluidic device

4.3.1 Effect of collagen coating on cell directional migration

One major problem for cell cultures in PDMS microfluidic devices is cell detachment from the PDMS surface, where cells grew poorly on the native PDMS surface. Surface modification by ECM proteins such as fibronectin[111] and collagen[112] have shown to significantly increase cell viability. In our experiment, 3T3 fibroblast cells were seeded on the PDMS surface and collagen I monolayer coated PDMS surface, while cell passage through microchannels was recorded by

time-lapse imaging. To determine if collagen coating influences cell persistent and directional movement, we compared the cell passage rate (numbers of cells crossed channel/numbers of cells entered channel) between two types of 3D matrix microchannels. As is shown in Figure 4.4, after collagen coating, both 3T3 fibroblast and 3T3 vimentin- (3T3 vimentin knockdown) cells showed a significant increase in the percentage of cells that passed through the channel. After collagen coating, the rate of cells moving backward inside the channel largely decreased and thus the rate of cell passage increased. The results indicate that in the 3D matrix, a monolayer of collagen can significantly promote cell directional migration inside the channel.

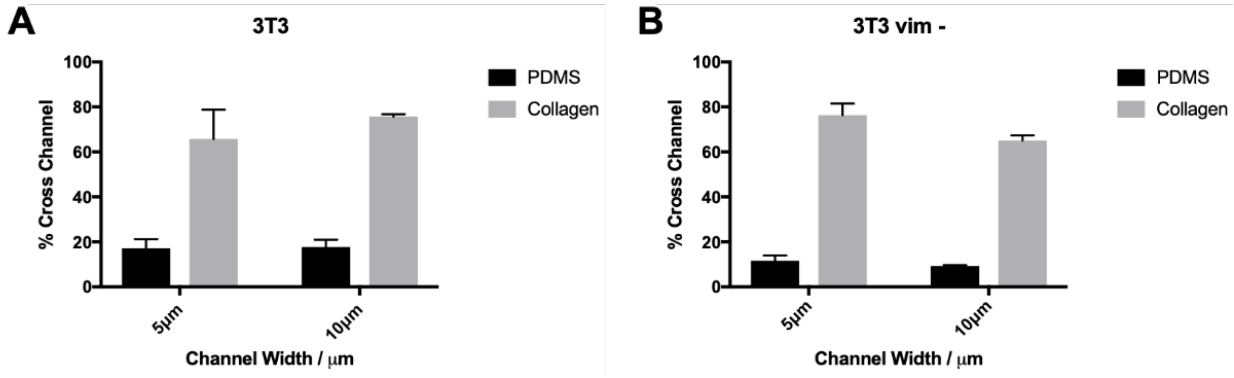


**Figure 4.4:** Effect of surface collagen I coating on cell persistent migration Before and after monolayer coating of collagen (A) Percentage of 3T3 fibroblast cells crossed 5$\mu$m and 10$\mu$m width channel (B) Percentage of 3T3 vimentin knockdown fibroblast cells crossed 5$\mu$m and 10$\mu$m width channel

4.3.2 Effect of vimentin on cell migration

Although it is well acknowledged that vimentin knockdown or knockout attenuates the migration of fibroblasts[2] and that motile and invasive cell lines express higher levels of vimentin, it has not been demonstrated in a 3D *in vitro* environment yet. To test the hypothesis, we designed microchannels with different channel widths (5$\mu$m and 10 $\mu$m) under a confinement height of 10 $\mu$m. 3T3 fibroblast and 3T3 vimentin- cells were seeded on collagen I-coated microfluidic device in the cell chamber then spontaneously entered into the channel without any constant chemical gradient. Cell motion was tracked by time-lapse imaging over 12 hr. Figure 4.5A shows the whole process of a cell entering into and exiting out of the channel. Cells enter

into microchannel by protruding its leading edge and making a contact with the channel wall, followed by squeezing and moving forward inside the channel.

The migration velocity of 3T3 fibroblast and 3T3 vim- cell were then compared. As shown in Figure 3B, the speed of 3T3 fibroblast cells is much faster than 3T3 vim- fibroblast cells. This result demonstrates that the expression of vimentin knockdown would impair fibroblast cell migration, which explains why vimentin-knockdown mice showed impaired wound healing abilities.

The effect of channel width on cell migration velocity was also shown in Figure 4.5B. Both 3T3 and 3T3 vim- cells showed higher migration velocity in the 5 $\mu$m width channel compared to 10 $\mu$m width channel. Decreasing channel width will increase the confinement level on the cell inside channel, moderate confinement of cells with length scales greater than the size of nucleus is shown to increase the cell speed[113]. A Microchannel based device for study of MDA-MB-231 cancer cell migration showed that cell exhibited higher migration velocity in narrower channel[114]. Cells are more "committed" to move through narrower channel than wider channels.

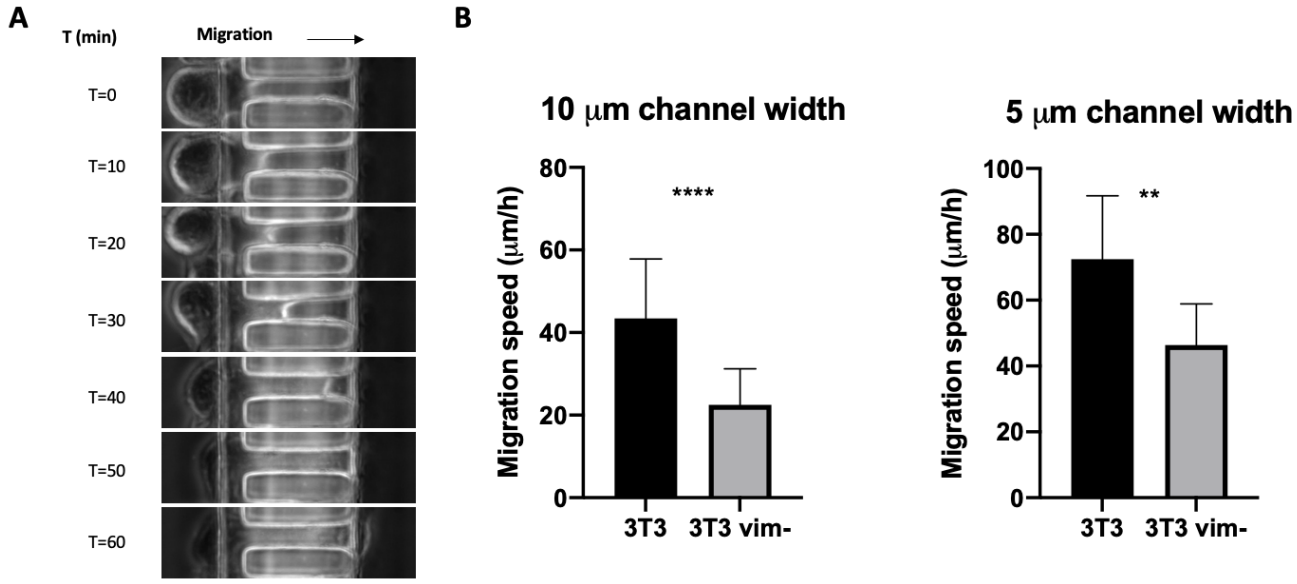


**Figure 4.5:** (A) Phase-contrast time-lapse images of a cell moving through channel coated with collagen-I. (B) Effect of vimentin on cell motility migration speed of 3T3 and 3T3 vim- cells in channel. Effect of channel width migration speed of both cell line in 5 $\mu$m and 10 $\mu$m width channel. (45-60 cells per condition, N= 3+ experiments). Denotation ****, $p < 0.0001$; **, $p < 0.01$.

### 4.3.3 Effect of vimentin on cell leading edge morphology

There is great diversity in the types of protrusions where the type of protrusion can be used to define a specific mode of cell migration. Lamellipodia-based migration is characterized by thin veil-like actin-rich extensions at the leading edge. Lamellipodia-based 3D cell migration was found in cancer cells and primary fibroblast cells. A study carried out in a 3D collagen matrix identified that human foreskin fibroblasts use lamellipodia migration in non-linear elasticity and can switch to lobopodian-based migration in linear elasticity[115]. This reveals that the modes of 3D cell migration can be governed by the 3D extracellular matrix. Another study was performed on migrating 3T3 fibroblasts constrained to a specific area using micropatterned polyelectrolyte self-assembly[116]. Cell migration in confined channels is regulated by cytoskeleton organization. Cells are fixed and stained when their cell leading edge is inside the channel. It is generally accepted that the propulsive actions of the cell body moving forward are dynamic traction forces at the leading edge[117]. Analysis of traction force in polarized migrating 3T3 fibroblast cells indicated that strong inward tractions were localized at the leading edge, lateral protrusion, and sometimes at the trailing edge of the cell[118]. Many in vitro studies performed on 2D surfaces[119, 120] have demonstrated that cells migrate by generating lamellipodial protrusions. The protrusions are caused by actin polymerization coupled with cell–matrix adhesion. Similarly, the degree of adhesion and RhoA signaling can uniquely identify the mode of 3D migration[121], which can be classified by different types of leading edge protrusions.

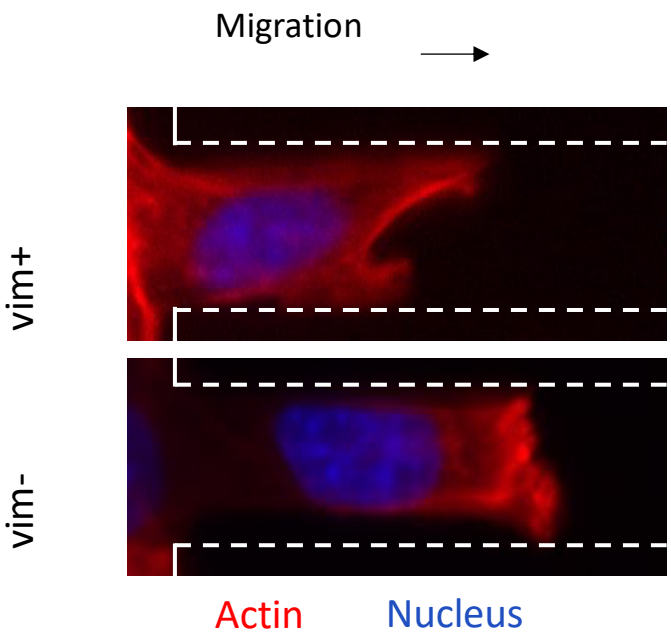


**Figure 4.6:** Leading edge morphology inside microchannel of 3T3 cell and 3T3 vim- cell

In our experiments, cells were fixed and stained after entry into the channel. Actin was stained as red and the nucleus was stained as blue. Leading-edge morphology of 3T3 fibroblasts and 3T3 vim- cells were observed to be different inside the channel (Figure 4.6). 3T3 fibroblast cells exhibit typical fan-like leading edge lamellipodia, which can be explained as the effect of vimentin on actin organization. 3T3 vim- cells project different leading-edge structures, which are blunt-ended lobopodian protrusions. This means that 3T3 vim- cells are unable to establish the polarity required for motility, which could explain the inhibition of motility. Thus, the regulation of vimentin may act as a molecular signal that modulates the actin-based machinery responsible for moving cells.

## 4.4 Conclusions

In conclusion, a microfluidic device with collagen-coated 3D microchannels was fabricated to study the effect of vimentin on cell migration and leading-edge protrusions. Cell passage rate through channels increased significantly after collagen coating of the microchannel, which provided a physiological-similar setting for this study. This device also revealed that interactions between the microchannel wall and cells inside microchannels are critical for cell 3D migration. Using this microchannel assay, vimentin knockdown cells showed lower cell motility

characterized by lower migration speed inside microchannel, proving that vimentin can promote fibroblast cell directional migration in a 3D microenvironment. Moreover, 3T3 vim- cells showed blunt-ended lobopodian protrusions different from typical fan-like lamellipodia protrusions in 3T3 fibroblast cells. This distinction demonstrated that vimentin expression regulates actin cytoskeleton organization and affects cell motility.

## CHAPTER 5: Development of Electrochemical 6-well plate with embedded gold electrode

### 5.1 Introduction

Electrochemical biosensor is one of most popular biosensors applied in food safety, environmental monitoring and biomedical diagnostics. It possesses the advantages of low cost, simplicity, easier to be miniaturized and mass fabricated. They also can be used as point-of-care (POC) devices at home or doctor's office [122]. Microfluidic devices are designed for handling analytical process with several advantages, such as short time for analysis, reduction of reagent costs, miniaturization, improvement of repeatability, portability and biocompatibility [123, 124]. Combine electrochemical sensor and microfluidic devices have a great attraction for both chemical and biomedical analytes. Hence, great effort about microfluidic devices integrated with electrochemical biosensor are reported [125-127]. Usually, the reported electrochemical microfluidic devices are made of silicon or glass substrate and polydimethylsiloxane (PDMS) cover with a special channel. A silicon or glass-based mold is required for preparing the PDMS cover. The fabrication process relies on photolithography or e-beam lithography, which are time-consuming, need relatively expensive equipment, and typically require a clean room environment.

In order to transfer this technology from the fundamental research to a day-life technology, it urgently needs to be disposable and reasonably less expensive. Polymer microfluidic device, due to their several merits, such as easier microfabrication and low-cost, fill these needs [128]. Even though extensive research has been carried out of polymer microfluidic device, rarely of the research activities integrated an electrochemical biosensor. The IDE array elements were fabricated on a polyethylenenaphtalate (PEN) substrate by Lakey and coworkers. Monolithic integration of three-material electrodes for electrochemical detection on poly (methyl methacrylate) (PMMA, also called acrylic) substrates were reported by Liu's group. However, both of them are used photolithography to prepare the electrode. And our results demonstrated that the PMMA is not good for depositing Cr/Au film (Cr film as an adhesive layer). The common tape can easily peel off the Cr/Au film. A good polymer substrate or polymer microfluidic device for electrode fabrication not yet extensively explored and demonstrated.

In this paper, PMMA, polyethylene terephthalate (polyester, PET), and glycol modified polyethylene terephthalate (PETG) are explored as substrate for fabricating the electrochemical biosensor. PETG-based microfluidic devices with embedded channels and gold film electrode

(GFE) are developed by the proposed simple, straightforward process, low cost and mass-producible method and sealed by a reversible tape-based mechanism. The electrochemical stability, morphology and long term EIS test ability of the device are investigated. Both redox ions and redox organic compounds are used to prove the electrochemical performance of the device. Owing to their low cost, PETG-based microfluidic devices integrated with electrochemical sensor can be used for disposable electrochemical sensor.

## 5.2 Fabrication and characterization of gold film electrode on different substrates

### 5.2.1 Gold sputtering onto PET, PMMA and PETG substrates

Three polymer substrates including PMMA, p ethylene terephthalate (polyester, PET), and glycol-modified polyethylene terephthalate (PETG) are explored for preparing electrochemical microfluidic devices. 10 nm Cr and 100 nm Au films were sputtered on the PETG microfluidic devices using ATC ORION sputtering system (AJA International, Inc.) Then, the PET-PDMS mask was removed from the PETG microfluidic device after sputtering and the device was connected to a printed circuit board (PCB) using copper wires and conductive silver glue (Fig. 1E/G). Three electrodes are then fabricated on the PETG microfluidic device. Different metal films can be selected, such as gold (Au), silver (Ag) and platinum (Pt). All these metal films need to use chromium (Cr) as an adhesion layer. As a proof of concept, all three electrodes are fabricated using Cr/Au film in this paper. The sputtering step is also a batch process since multiple devices are sputtered at the same time without any additional cost of time or coating materials. Such batch fabrication processes help to increase the throughput of the device fabrication, decrease the cost of each device, and provide a potential for commercialization.

Initially, the PMMA sheet was selected as the substrate for preparing the microfluidic device. However, it was found that the Cr/Au film cannot adhere to the PMMA substrate well. Especially when using tape as a cover, the tape can easily peel off the Cr/Au film sputtered on the PMMA substrate. To look for a suitable substrate, three other different polymer substrates including white PET (McMaster-Carr, 8597K92), transparent PET (Professional Plastics, SPETCL. 125RTM), transparent PETG (McMaster-Carr, 85815K16) are explored. The results show that the Cr/Au film has some adhesion to PET (transparent), but it is not robust. By comparison, the adhesion of Cr/Au to the PETG (transparent) was excellent. The tape peel-off tests were carried out on silicon-Cr/Au film, glass-Cr/Au film, PETG-Cr/Au film, PET-Cr/Au

film, and PMMACr/Au film (Figure 5.1). It was demonstrated that the silicon-Cr/Au film, glass-Cr/Au film and PETG-Cr/Au film cannot be peeled off by tape. PET-Cr/Au film and PMMA-Cr/Au film can be peeled off by a tape. The results proved excellent electrochemical stability of PETG-Cr/Au film. PETG is a type of low-temperature thermoplastic sheet/film with favorable thermoformability, machining performance, and chemical resistance. It is also a type of very cost-effective polymer substrate. Furthermore, PETG not only has noticeable toughness, enough stiffness to maintain the fluidic channel geometry, optical clarity for imaging, and high manufacturability but also is an environmentally friendly and healthy plastic resin. The results revealed that PETG is an excellent polymer substrate for developing plastic electrochemical devices, flexible electrochemical sensors and polymer microfluidic systems.

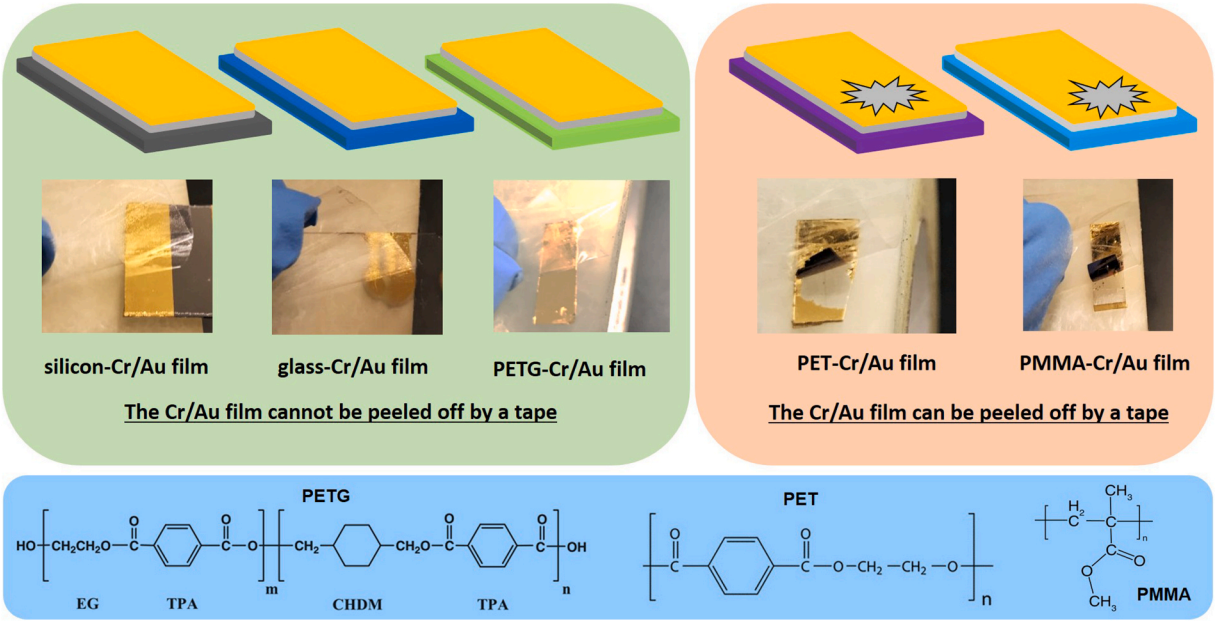


**Figure 5.1:** Stability of Cr/Au film on silicon, glass, PETG, PET, and PMMA substrate using a common tape (Scotch, 3M) to peel the film and chemical structures of PETG, PET and PMMA. CHDM:1,4-cyclohexane dimethanol. EG: Ethylene glycol. TPA: Terephthalic acid.

5.2.2 Electrochemical stability of the GFE on the PET, PMMA and PETG substrates

A conventional cell with a three-electrode configuration was used to test the electrochemical performance of different substrate-based GFE. The working electrode was GFE on the PETG, PET, and PMMA. Platinum wire and Ag/AgCl (saturated KCl) were used as the counter electrode and the reference electrode, respectively. The stability of the GFE on the PETG, PET

and PMMA substrates were evaluated by cyclic voltammetry with 200 scans in 1 M KCl containing 5 mM K3 [Fe(CN)6 ]/K 4 [Fe(CN)6 ]. Although the results show good stability of the GFE on both PETG and PET. The GFE on the PET substrate can be peeled off by water flushing after the multiloop CV test.

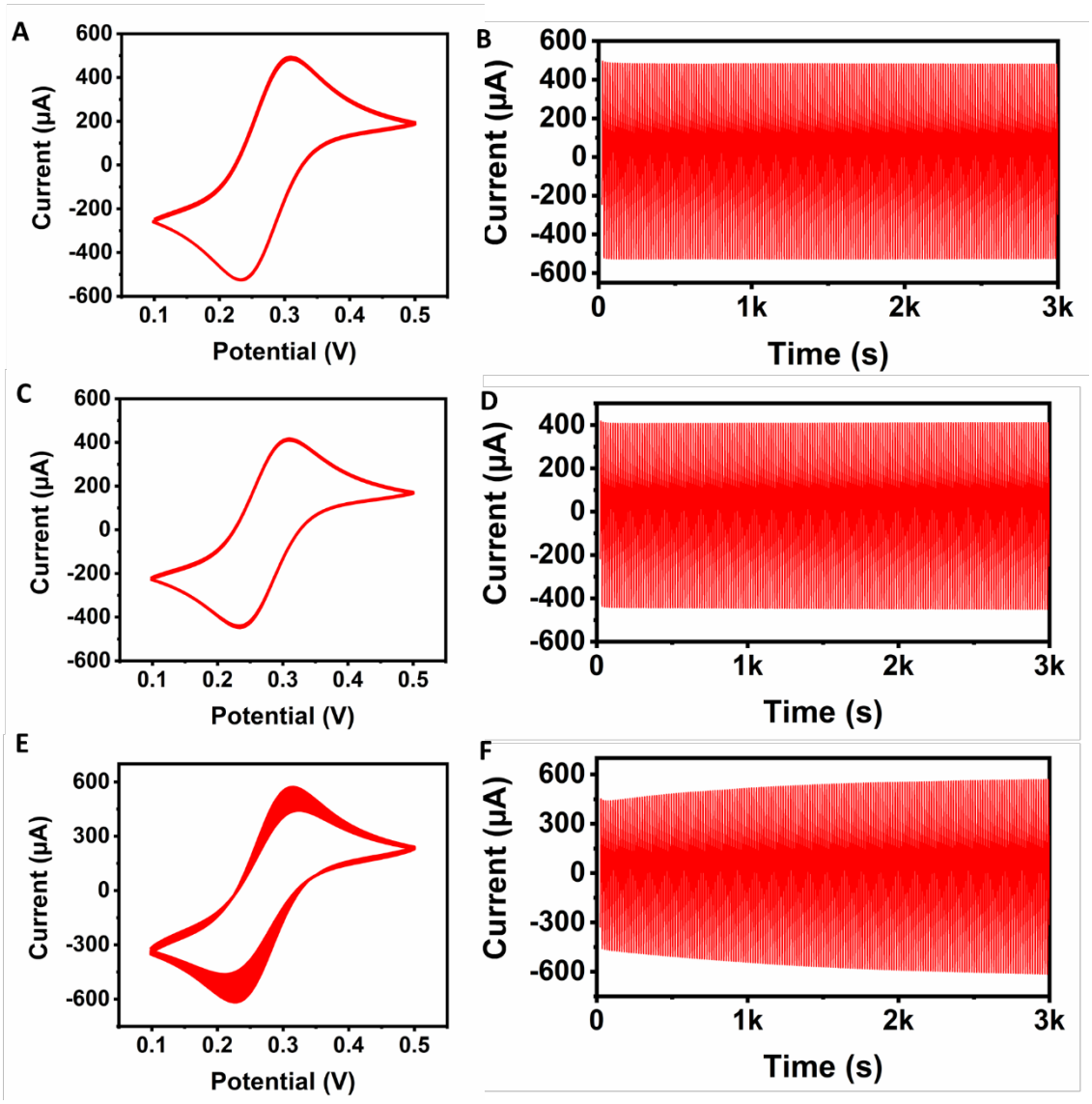


**Figure 5.2:** CV plots and plots of current to time of bare GFE on the PETG (A/B), PET (C/D), and PMMA (E/F) substrates in 1 M KCl containing 5 mM K3 [Fe(CN)6 ]/K 4 [Fe(CN)6 ], with a scan rate of 50 mV/s, 200 scans.

5.3 Preparation of flexible electrochemical sensor on the PETG film

Nowadays, flexible electrochemical sensors are the most popular and draw great attention to health monitoring. Because of the good adhesion of PETG substrate and Cr/Au film, a flexible electrochemical sensor with three electrodes are fabricated on PETG film (Figure 5.3 A/B/C). The stability of the flexible electrochemical sensor was evaluated by CV with 100 scans (Figure 5.3D) in 1 M KCl containing 5 mM K3 [Fe(CN) 6 ]/K4 [Fe(CN)6 ]. The results show excellent stability. It proves that the PETG is a novel polymer substrate for the fabrication of flexible electrochemical sensors.The CV responses of the mixture solution of DA and AA were recorded at the flexible Au electrode (Figure 5.3E). The oxidation peak at about 0.4 V occurred and oxidation peak current increased with increasing dopamine concentration, which is consistent with the CV on bare GFE on PETG-based substrate. This demonstrated the electroactive performance of the flexible Au electrode toward dopamine as well.

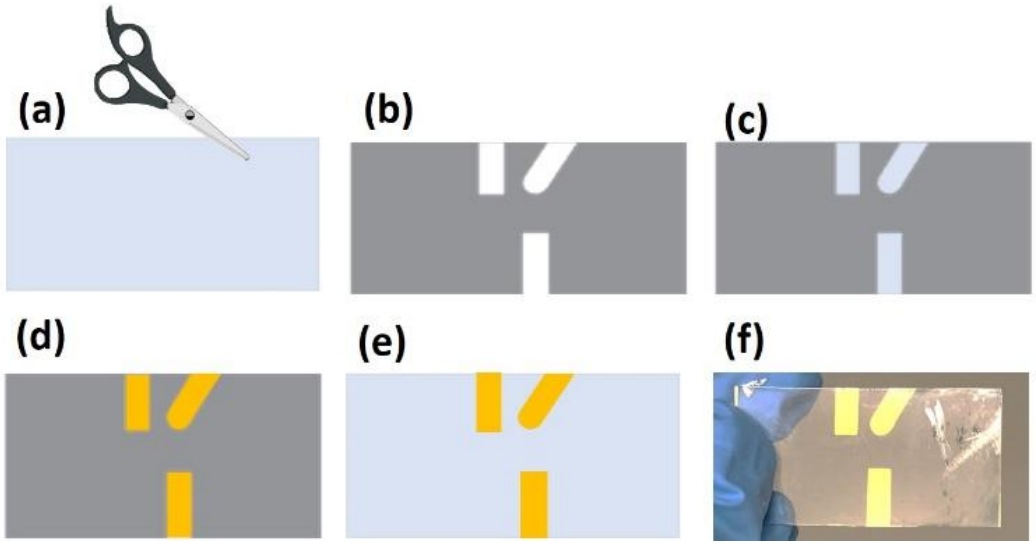


**Figure 5.3:** Schematic diagrams to illustrate the preparation of flexible electrochemical sensors on the PETG film. (a) Use a scissor to cut the PETG film into a rectangle with a size of 38 mm × 20 mm. (b) Design a PET mask by AutoCAD software and prepare it by VLS-4.60 Universal Laser Systems. (3) Use the double-sided tape to bind the PETG film and PET mask. (d) Sputter 10 nm Cr and 100 nm Au films on the PETG film using ATC ORION sputtering system (AJA International, Inc.) (e) Carefully remove the PET mask and then get the flexible electrochemical sensors. (f) An image of a prepared flexible electrochemical sensor.

## 5.4 Preparation of electrochemical 6-well chip for future point-of-care use

PETG is a type of copolymer of PET and ethylene glycol. It is a transparent amorphous thermoplastic with stable thermomechanical properties and has been employed in biomedical medical devices [129, 130]. It is also one type of excellent polymer substrate for fabricating the chrome/gold (Cr/Au) film electrode [131]. Herein, PETG is used as the substrate to prepare the Cr/Au film electrode and chrome/silver (Cr/Ag) film electrode. Usually, the reported electrochemical devices use silicon or glass as substrates [132, 133]. Compared with fragile silicon wafer and glass, PETG has better machining performance and can be a good alternative substrate for fabricating electrochemical devices. It was cut into small rectangles with a size of 40 mm × 28 mm using a band saw (Figure 5.4A). PET mask (Figure 5.4B) was designed by AutoCAD software and prepared by VLS-4.60 Universal Laser Systems. The double-sided tape was used to bond the PETG sheet and PET mask reversibly (Figure 5.4C). Cover the reference electrode area with tape and sputter 10 nm Cr and 100 nm Au films on the PETG sheet using ATC ORION sputtering system (AJA International, Inc.) (Figure 5.4D/E). Then, use tapes cover the WE and CE area and sputter 10 nm Cr and 300 nm Ag films on the PETG sheet (Figure 5.4F/G). Carefully remove the PET mask and the PETG sheet with electrodes was prepared (Figure 5.4H/K).

Acrylic mold with wells was designed by AutoCAD software and prepared by VLS-4.60 Universal Laser Systems. Every well can contain 60 μL solution. It was bonded to the PETG sheet using double-sided tape (Figure 5.4I). Finally, The PETG/acrylic device was connected to a printed circuit board (PCB) using copper wires and conductive silver glue (Figure 5.4L). The electrochemical wells can be sealed with tape.

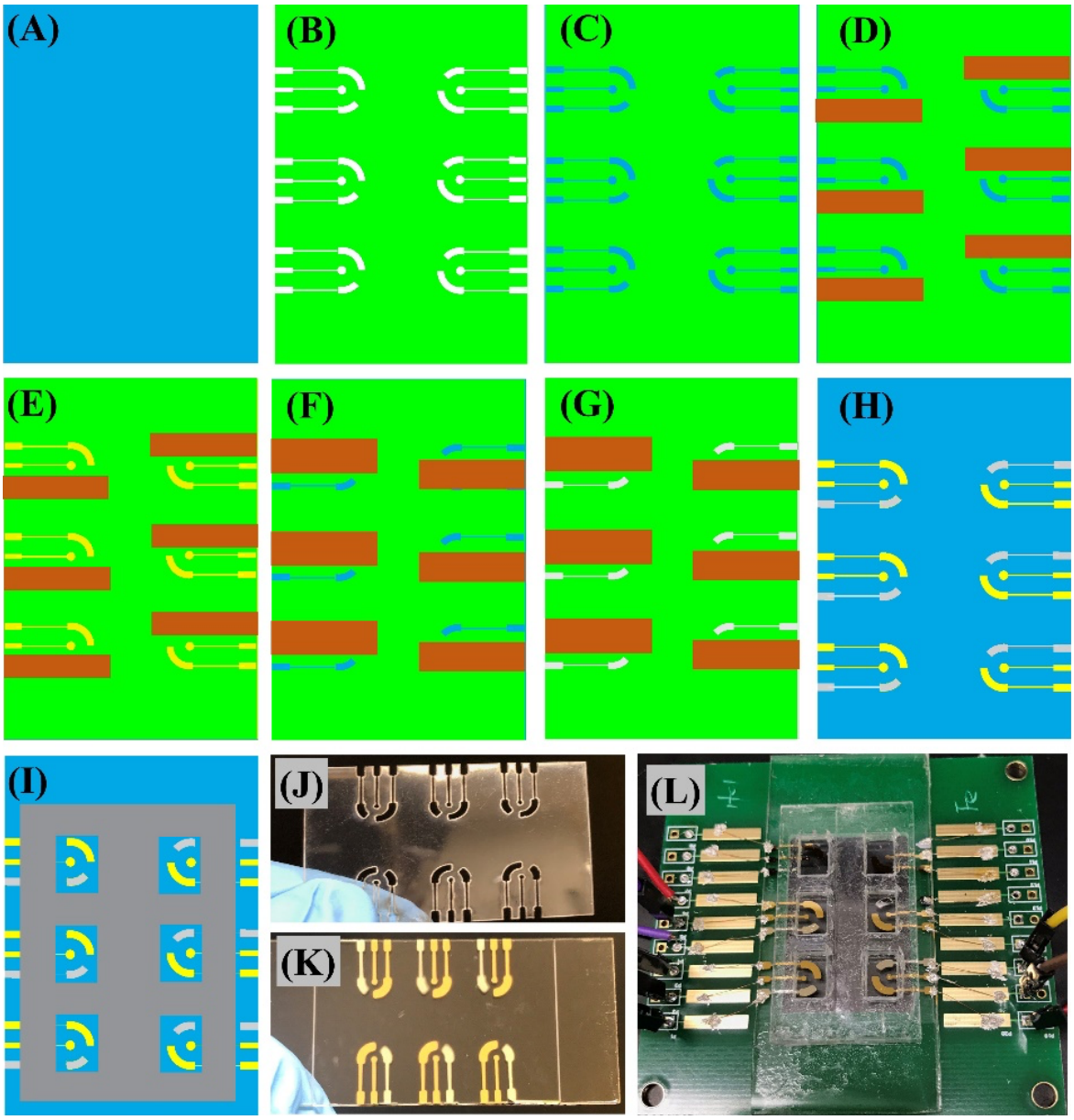


**Figure 5.4:** Schematic diagrams to illustrate the preparation of electrochemical 6-well plates. (A) PETG sheet with a size of 40 mm × 28 mm. (B) PET mask. (C) Use the double-sided tape to bond the PETG sheet and PET mask. (D) Use tapes to cover the RE area. (E) Sputter 10 nm Cr and 100 nm Au films on the PETG sheet. (F) Use tapes to cover the WE and CE area. (G) Sputter 10 nm Cr and 300 nm Ag films on the PETG sheet. (H) Carefully remove the PET mask and then get the electrodes on the PETG sheet. (I) Use double-sided tape to bond the acrylic mold with wells and PETG sheet. (J) Image of PET mask. (K) Image of PETG sheet with 6 groups of electrodes. (L) Image of the prepared electrochemical 6-well plates.

## CHAPTER 6: Cancer metastasis on chip technology development

### 6.1 Mechanical cues in tumor microenvironment

Tumor formation and progression is influenced by two key factors: genetic/epigenetic changes in tumor cells and the rearrangement of the components of the tumor microenvironment (TME) through mutual and dynamic crosstalk. TME is a complex system consisting of tumor cells, stromal cells, immune cells, and extracellular matrix (ECM). The crosstalk between tumor cells and their neighboring microenvironment is shown to influence tumor formation and maintenance.

As increasing focus have been put on interaction between cancer cell and stromal cell and ECM matrix, ECM matrix was shown to play a vital role in cancer initiation, progression, metastasis and anti-cancer drug efficacy. Cancer cells react to physical cues in ECM through cell mechanotransduction with behaviors such as spreading, migration and differentiation, and can thereby initiate major pathologies such as metastasis and fibrosis[134]. Cell mechanotransduction include three necessary steps: mechanotransmission, mechanosensing, and mechanosignaling[135]. When the applied force is transmitted to mechanosensory structure and transduced into a biochemically detectable signal by cell mechanosensory structures, the mechanotransmission and mechanosensing can trigger a specific intracellular signaling response termed as mechanosignaling. A typical example is the increased stiffness in solid tumor such as colon cancer and breast cancer. This have been widely used by clinicians for cancer diagnosis and therapeutic applications. Physical components in ECM can affect cancer cell adhesion, migration, proliferation, apoptosis and survival. For example, cancer cells preferentially migrate to lesser stiffness matrix and cell migration speed is affected by stiffness. Recent studies have investigated the role of physical cues such as physical forces, confinement, flow and stiffness and replicate them in *in vitro* cell culture model. While ECM properties can change cellular behavior, cancer cells themselves can in turn remodel the ECM and create a microenvironment that promotes cancer metastasis.

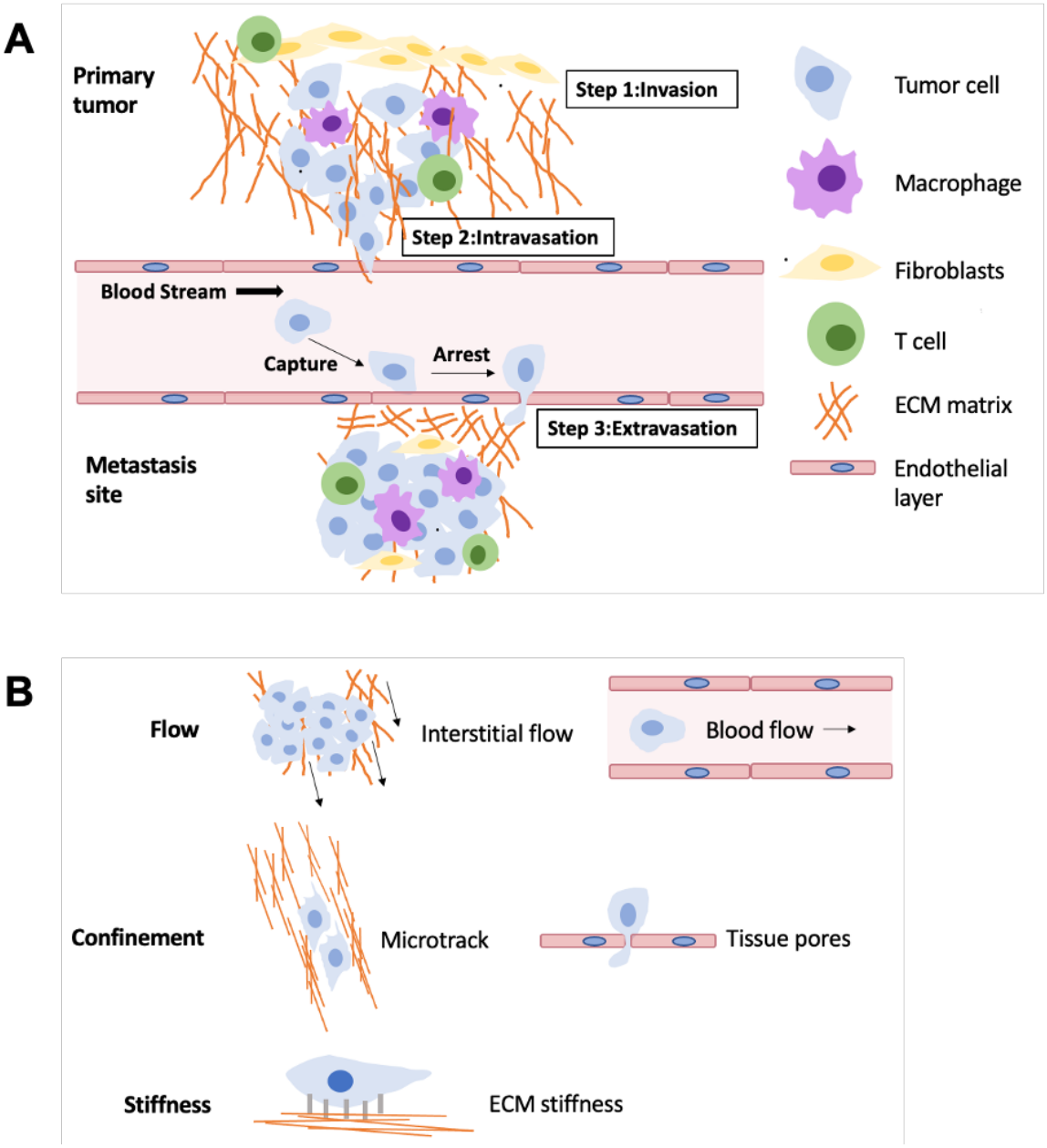


**Figure 6.1:** (A) Illustrated Overview of the Metastatic Cascade. Schematic showing the essential steps in metastasis. (B) Mechanical cues in tumor microenvironment

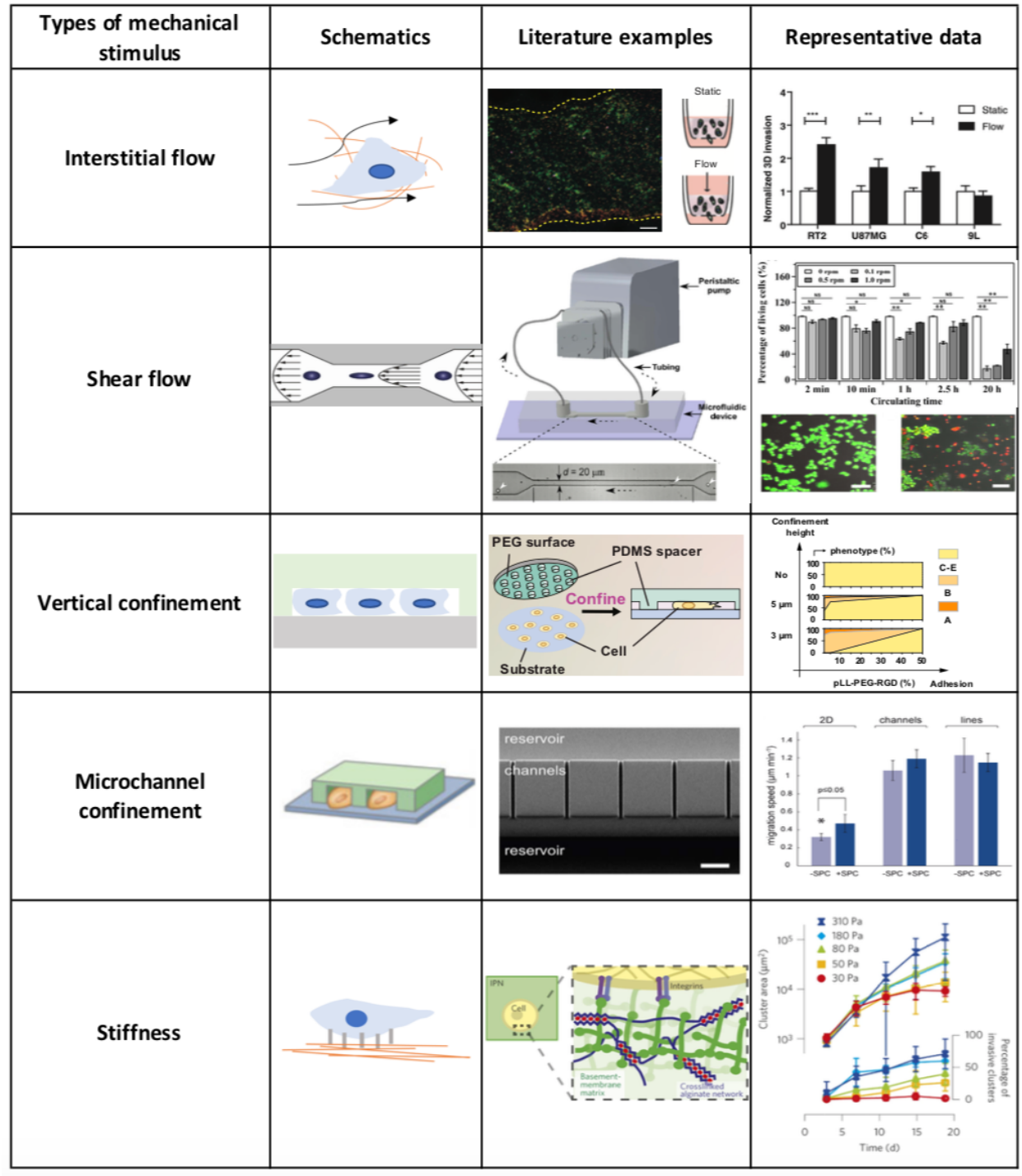


**Figure 6.2:** Modeling of mechanical cues in tumor microenvironment on chip

6.1.1 Shear flow

Liquid flow on cancer on chip system induced fluid shear stress on cancer or tumor cultured on chip, thus called shear flow. Fluid shear stress, defined as the internal fractional force between

adjacent layers of fluid of viscosity moving at different velocities, has units of force per area (N $m^{-2}$) or dynes per square centimeter (dyn $cm^{-2}$). The shear stress in blood flow vary between 1-4 dyn $cm^{-2}$ in the venous circulation and 4-30 dyn $cm^{-2}$ in the arterial circulation[136], up to 30 dyn $cm^{-2}$ in interstitial area between bone and tissues.

Extravasation of tumor cell from blood vessel requires cell adhesion to the vessel wall through specific bonds. The shear force exerted on cell will influence the residence time and adhesive force. leukocytes require a threshold shear stress to tether to and role on endothelial cells at sites of inflammation and injury. Increasing flow initially decrease cell rolling velocity, after the optimal wall shear stress is reached, cell rolling velocity increase with flow increasing[137]. Circulating tumor cells in blood vessel can be captured and arrested at endothelial cell membrane by specific receptor-ligand binding.

The elevated interstitial fluid flow and interstitial fluid pressure at tumor margin has been documented in virtually all solid malignant tumors. High interstitial fluid pressure(IFP) is a prognostic factor for cervical cancer patients, patients with high IFP are more likely to recur and die of progressive disease[138].Tumor IFP can be high as capillary pressure range from 10-40 mm Hg while normal tissue pressure range from -2-0 mm Hg[139]. IFP elevation in tumor can be attributed to high tumor blood vessel permeability, dense ECM of tumor interstitial space and low lymphatic drainage[140]. In the clinical setting, chemotherapy, bevacizumab[141] and paclitaxel[142] have been shown to reduce the IFP of rectal and breast tumors. Elevated IFP has been implicated as the physical barrier for transport of macromolecules[143] and biopharmaceuticals in the tumor microenvironment, thus lowering the IFP might be a useful approach to improve anticancer drug penetration into tumor. There are already certain compounds known to lower tumor interstitial fluid pressure such as VEGF antagonist and PDGF antagonist.

Interstitial fluid flow may also affect tumor microenvironment and promote tumor progression. Fibroblast-to-myofibroblast transition is usually induced by secretion of TGF-$\beta$1 by tumor cells, it was showed that[144] low levels of interstitial flow itself can also induce the transition and collagen alignment by simply exposing fibroblasts to interstitial flow. TGF- $\beta$1 secreted by blood platelets or tumor cells exist in biologically inactive(latent) form, meaning it must be activated before it acting on cells. In vitro and in vivo experiments demonstrated that

TGF- $\beta 1$ can be activated by shear stress[145]. Interstitial flow can also promotes vascular fibroblast and myofibroblast cell motility via upregulation of MMP-1[146]. In addition to induce fibroblast-to-myofibroblast transition and collagen alignment**,** interstitial flow also affect stromal stiffening. As interstitial flow drives matrix tension and pull on cell-ECM matrix, cells respond by aligning and stiffening the ECM, thus cause the stiffening of tumor stroma. Flow was shown to have direct effects on cancer cell invasiveness. Cancer cells utilize interstitial flow to create and amplify chemokine CCL21 gradients[147], thus drive invasion in the flow direction.

| Cancer model | Description of flow | Experimental setup | Finding | Reference |
|---|---|---|---|---|
| MDA MB 231 breast cancer cell | Interstitial flow, (3 $\mu m/s$ and 0.3 $\mu m/s$) | Cells cultured in a microfluidic device | Breast cancer cells cultured in 3D aligned parallel to flow streamlines when exposed to interstitial flow | |
| MDA_MB-435S human melanoma with human fibroblasts | Interstitial flow(0.5 $\mu m/s$) | Cells cocultured in collagen matrix | Synergistic increase in cancer cell invasion with flow and fibroblasts | Shieh et al[148] |
| MCF7 and ZR75-1 breast carcinoma | Interstitial flow (0.2 $\mu m/s$) | Cells cultured in collagen matrix | Interstitial flow induced cancer cell invasion and this could be explained by CCR7 ligand created under flow. | Shields et al[147] |
| RT2 and eGFP-RT2 glioma cells | Interstitial flow (0.7 $\mu m/s$) | Cell cultured in 8um pore cell culture inserts | CXCR4 was activated in response to flow which promotes glioma cell motility | Munson et al[149] |

| | | | | |
|---|---|---|---|---|
| Macrophage | Interstitial flow ($3\ \mu m/s$) | Cultured in microfluidic device | Interstitial flow polarizes macrophages toward a M2-like phenotype via integrin/Src mechanotransduction pathway | Ran et al[150] |

6.1.2 Stiffness

Stiffness varied greatly in human body, ranging from very soft environment (Young's modulus, E= ~20Pa) to very rigid environment (E= ~GPa). Clinicians have been using palpation or magnetic resonance elastography to diagnosis tumor for decades, given the increased tissue stiffness is a classic characteristic of solid tumor[151]. A typical example is human breast cancer, breast cancer stromal tissue exhibit an elastic modulus which is 10-fold stiffer than normal mammary tissue. Computational modeling have found that the stiffness of a solid tumor must exceed 1.5 times of surrounding tissue in order to continue to expand[152]. Human breast tumors are often fibrotic and fibrosis increases tumor malignancy. Elevated collagen crosslinking can stiffen ECM and induce tissue fibrosis[153]. Lysyl oxidase(LOX) enzymes are soluble mediators that catalyze the covalent crosslinking of fibrous collagen. Thus, using LOX inhibition to disrupt ECM stiffening is a potential therapeutic strategy[154]. Celecoxib(Celebrex) is a clinically approved drug for inflammatory disease treatment, it is shown to decrease collagen deposition and inhibit tumor growth in a mouse model of breast cancer[155]. Increasing stiffness have been shown to induce malignant phenotype. High matrix stiffness drives epithelial-mesenchymal transition through promoting translocation of an essential mechanomediator TWSIT1[156]. An invasive and malignant phenotype was shown to be accompanied by a shift toward higher stromal stiffness during human breast tumor progression. Increased tissue stiffness modulates microRNA expression to drive tumor progression by reducing levels of tumor suppressors PTEN[157]. Acerbi et al[151] found that the ECM stiffness and cellular mechanosignaling were the highest at the invasive front of breast cancer stroma. They also established that stroma stiffness and the level of cellular TGF beta signaling positively correlated with each other. Another study[158] showed that matrix stiffness alone is sufficient for activation of intracellular-signaling

pathways with pancreatic stellate cells, encouraging the cells to produce excess collagen. This mechanosensing process also forms positive-feedback loop, where pancreatic stellate cells continue to secrete collagen to make the matrix stiffer. At the same time, researchers found that increasing matrix stiffness not only promote cancer cell invasiveness but also induce expression of biomarkers in solid cancers[159]. Moreover, biochemical signaling in cancer cells can in turn modulate matrix stiffness. Secretion of matrix metalloproteinases (MMPs) and lysyl oxidase (LOX) in cancer cells will enhance deposition of collagen and cross linking[160], thus increasing matrix stiffness. Lamin-A conformation and expression are mechanosensitive in response to changes in stiffness in tissue culture cells[159, 161]. A downstream pathway of matrix stiffness, the RA pathway[162], can regulate lamin-A transcription.

ECM stiffening stimulates cells to generate higher intracellular actomyosin contractility and exert stronger traction forces on their surroundings. Cells are able to detect and respond distinctly to change in stiffness through cell-specific combination of integrin receptors[163]. Integrin cluster together to activate adaptor proteins of focal adhesions and downstream signaling molecules. 3T3 fibroblast cells consistently migrate in the direction of increasing stiffness by adaptably regulate their contractility in accord with substrate stiffness[164]. Fibroblasts on soft substrate had no stress fibers compared to fibroblasts on stiff substrate that have articulated stress fibers[165]. By culturing 3T3 control and vimentin knockdown fibroblast cell on PAA gels with stiffness values ranging from 2-20kPa, vimentin knockdown cells were less responsive to change in stiffness[166]. Diffusive and dynamic adhesion proteins were observed on soft gels (E ~1kPa). In contrast, stable focal adhesion proteins were observed on stiff gels (E ~30-100kPa)[167]. ECM stiffening and collagen cross linking promoted cell focal adhesions and enhanced PI3K signaling, which induce the invasion of a pre-malignant epithelium[159].

### 6.1.3 Confinement

The microenvironment offers many tracks for confined cell migration, including tracks along ECM fibres along or with blood vessels, between connective tissue and the basement membrane of muscle, in the interstitial space or in the vasculature of organs. Cells migrating in vivo experience varying degree of confinement as the cross-sectional area of in vivo pores/channels vary[168] from 10 to >400μm². The *in vivo* importance of these tracks is substantiated by many observations in mouse and human tumor cells. In an orthotopic mouse model of breast cancer

MTLn3, using multiphoton laser scanning microscopy, tumor cells were observed to preferentially migrate along collagen fibers[169]. Cancer cells escape from primary site and eventually flow to the capillaries of organs in body. Lung and liver capillaries, typically 3-8 μm, were known very efficient at arresting flow of cancer cells[170]. Glioma cells mainly migrate along blood vessels, when injected into brain, vast majority of glioma cells move in contact with blood vessels[171]. More importantly, white matter tracks and perivascular space in brain have shown to work as "highways" for glioma cell migration[172], which is regarded as main causes of poor therapeutic outcome.

Time-lapse imaging studies conducted *in vivo* and *ex vivo* showed that tumor cell undergo remarkable shape and volume change during metastasis. Quantitative 3D imaging in vivo showed enhanced fluorescent human gliomas undergo periodic changes in cellular volume (~33%) when migrating through cerebral parenchyma[173], enabling these cells to fit through narrow spaces in brain. Similar magnitude occurs when glioma cells migrated across transwell barrier size of 3-8$\mu m$. Cancer cells in the capillaries have the ability to elongate to fit the width of confinement. A study done on HT-1080 fibrosarcoma cells[174] showed that the average length of the major axis of cancer cells increased about 4 times to their normal length, the length of nuclei increased about 1.6 times. The nuclei of HT-1080 cells adopted hourglass deformations with diameter of 3-7 $\mu m$, these morphological signatures were distinct from the ellipsoid nuclear shape[175].

An investigation of mammalian tumor cell migration in confining environment showed that confinement induces nuclear envelope rupture and compromises DNA integrity[176]. Nuclear envelope rupture may result in genomic instability, which then may promote cancer progression. Moreover, as nucleus is considered as a physical obstacle, mechanisms that actively help cells to deform nucleus and transmigrate confinement may be essential for cell locomotion[177]. The overexpression of membrane protein SUN2 lowed lamin-A level, decreased nucleus stiffness and produced nucleus rounding[178].

Mechanism of cancer metastasis migration mode were demonstrated different between unconfined and confined environment. Confinement was shown[179] to alter the relationship between cell contractility and velocity, which then induce different types of protrusion thus different migration mode. Cancer cell migration on 2D unconfined surface are highly dependent

on actomyosin contractility, it doesn't necessarily play a role in cell migration inside 3D confinement environment[180]. Hung et al [175] demonstrate that a Piezo1dependent intracellular calcium increase negatively regulates protein kinase A (PKA) as cells transit from unconfined to confined environment. While in vitro studies of cell migration on 2D surfaces have established that cells use actin polymerization coupled with cell-matrix adhesion to generate thin and wide lamellipodial protrusions during migration, imaging of cell migration in 3D models revealed that lamellipodia based migration is only one of multiple migration strategies. Confined cell migration modes including pseudopodial, lobopodial, bleb-based, protrusion-based and osmotic engine migration are distinguished by differences in cell morphology, the extent of adhesion to ECM and mechanics of leading-edge protrusion. More importantly, mode switching have been observed in both cancer cell lines and normal fibroblasts, cell use different modes of migration depending on the physical properties of ECM, the degree of extracellular proteolysis and soluble signaling factors. For example, transition of slow mesenchymal cells to a fast ameboidal motion have been observed in cancer cell migration in 3D confined environment[181]. Switching from lamellipodia-based mesenchymal mode to the amoeboid or rounded form after extracellular proteolysis is inhibited were observed in breast cancer cell line.

Confinement stimulus is capable of initiating and regulating intracellular signaling events. Cells tune the signaling input to achieve an optimal balance between RAC1 and RHOA-myosin II signaling, such that there is a strong RAC1 output for efficient cell locomotion on unconfined 2D surfaces and a strong RHOA–myosin II output for confined migration[182]. It was recently reported[183] that confinement of A375 cells induces an increase in intracellular calcium levels via the stretch-activated cation channel PIEZO1. This confinement-induced increase in intracellular calcium levels negatively regulates the activity of protein kinase A (PKA) via a phosphodiesterase 1 (PDE1) dependent pathway. Different mechanisms of how cell sense and adapt to different physical microenvironment were proposed and remain to be determined.

## 6.2 In vitro model for vertical confinement control

### 6.2.1 Current approaches for vertical confinement control

Vertical confinement externally applying compressive forces on cells sandwiched between two surfaces. Cells can migrate laterally but confined at basal and apical surfaces. Cell can be dispersed and vertically confined by lowering a pillared PDMS array against cell, the

confinement height is defined by the height of pillars[184]. Liu et al[185] used a micro-spacer with controlled height and varying adhesion strength by controlling the ratio of pLL-PEG and pLL-PEG-RGD on surface. They observed that fibroblast cells experienced mesenchymal-to-amoeboid transition (MAT) when they switch from low 2D adhesion environment to 3D confinement environment. This method can enable vertical confinement down to height of $3\mu m$ with accuracy of 100nm over large areas[186]. Vertical confinement can also be recapitulated using compliant gels on cells. Polyacrylamide (PAA) hydrogels are widely used to study *in vitro* the effect of the mechanical environment on cell behavior. PAA gels are nearly purely elastic, with the shear storage modulus several orders of magnitude larger than the loss modulus. The storage modulus of the gel is determined by the concentration of polymerized acrylamide and the degree of cross-linking. Over the last two decades, protocols have been optimized to tune PAA gels for a range of different stiffnesses suitable for cell culture. The use of these materials has shed light on the involvement of the cellular microenvironment in controlling cell motility, cell cycle, spreading, and differentiation. In contrast to PAA gels, which are elastic, soft biological tissues are viscoelastic and, thus, characterized by both a storage and an appreciable loss modulus. Until recently, only the storage modulus of tissues could be reproduced by classical PAA gels *in vitro*. In order to reproduce more precisely the mechanical properties of biological tissues, we developed a method to make viscoelastic PAA gels that reproduce both the storage and loss moduli of biological tissues.

### 6.2.2 Preparation of PAA gel/Collagen substrate

We fabricated polyacrylamide (PAA) gel disks with embedded with fluorescent using the following protocol. The surface of 25 mm × 25 mm square glass coverslips (VWR, Radnor, PA) were cleaned and silanized with 1% 3-aminopropyl-trimethoxysilane solution (Alfa Aesar, Haver Hill, MA) for 10 min and then treated with 0.5% glutaraldehyde (Amresco, Solon, OH). Round glass coverslips with a diameter of 18 mm (VWR) were plasma cleaned and coated with 0.1 μm fluorescent (580 nm/605 nm) beads (Life Technologies, Carlsbad, CA) on the surface. Stock solutions of acrylamide and bis-acrylamide mixture were made by mixing an appropriate amount of 40% acrylamide (Bio-Rad, Hercules, CA) and 2% bis-acrylamide (Bio-Rad, Hercules, CA) in HEPES buffer (50 mM pH = 8.2). The final concentration of acrylamide and bisacrylamide in the mixtures were varied to generate gels of Young's moduli $E$= 2 kPa, 7.5 kPa, 13 kPa, 20 kPa, and 40 kPa, respectively. After degassing 500 μL of the mixture, 5 μL of 10% ammonium persulfate

(Amresco) and 1.5 μL of N,N,N′,N′-tetramethylethylenediamine (Amresco) were added to initiate the acrylamide polymerization. Immediately after the initiators were added, 25 μL of the solution was taken out and sandwiched between the bead-coated round coverslip and the glutaraldehyde coated square coverslip. After 15 min of polymerization, PAA gels form between the coverslips. The gel and coverslips system were then submerged in cold HEPES buffer for 30 min. The round coverslip was then carefully removed, resulting in a gel disk of 18 mm in diameter and approximately 100 μm in thickness attached on the 25 mm × 25 mm square coverslip. The fluorescent beads are embedded uniformly within a 2 μm thin layer below the gel surface.

The distribution of fluorescent beads embedded in PAA gel was characterized by confocal microscopy using Leica SP5 confocal microscope with an HPX Plan Apo 63× Oil immersion objective lens (Leica Microsystems Inc., IL). Before subjected to confocal imaging, 2 μm beads were sparsely deposited onto the gel to enable identification of the top gel surface. A 60 μm confocal stack with 50 nm step size was then acquired from 15 μm above the gel surface to 45 μm inside the gel. The centroids of beads were tracked using ImageJ.

The stiffness (Young's Modulus) of gel disks was measured by nanoindentation using Atomic Force Microscopy. All measurements were performed utilizing an MFP-3D-BIO atomic force microscope (Asylum Research, Santa Barbara, CA) and DNP cantilevers (Bruker, Camarillo, CA) with a nominal spring constant 0.06 N/m. Gel rigidity values were extracted from the recorded AFM force-distance curves by fitting it to the Hertz model using a custom MATLAB routine.

Collagen type I was crosslinked to the PAA gel surface using sulfo-SANPAH. The gels were submerged under 1 mg/mL sulfo-SANPAH (G-Biosciences, St. Louis, MO) solution and placed 2 in. below an 8 W ultraviolet UV lamp (Hitachi F8T5 – 365 nm) and irradiated for 8 min. The gels were then washed with PBS buffer and soaked with 0.1 mg/mL rat-tail collagen type I (BD Bioscience, San Diego, CA) for 8 h at 4°C. After collagen coating, the gels were rinsed with PBS buffer. The collagen-coated gels were placed in culture medium and incubated for 15 min at 37°C before used for TFM experiments.

6.2.3 Cell seeding and cell culture inside PAA/collagen gel coated glass slides

30min before plating cells, immerse the PAA/collagen gel coated glass slides in cell media and incubate at 37℃. This step ensures that gels are at 37℃ and soaked in media when cells are plated. Remove enough media so that gels will be hydrated but not immersed. Cells were then plated in a small volume at about 500 $\mu L$ to maximize cellular adhesion. After 2 h or once cells start to spread, add another PAA/collagen gel coated glass slide on top, then apply the vacuum force to leave two glass slides in close contact.

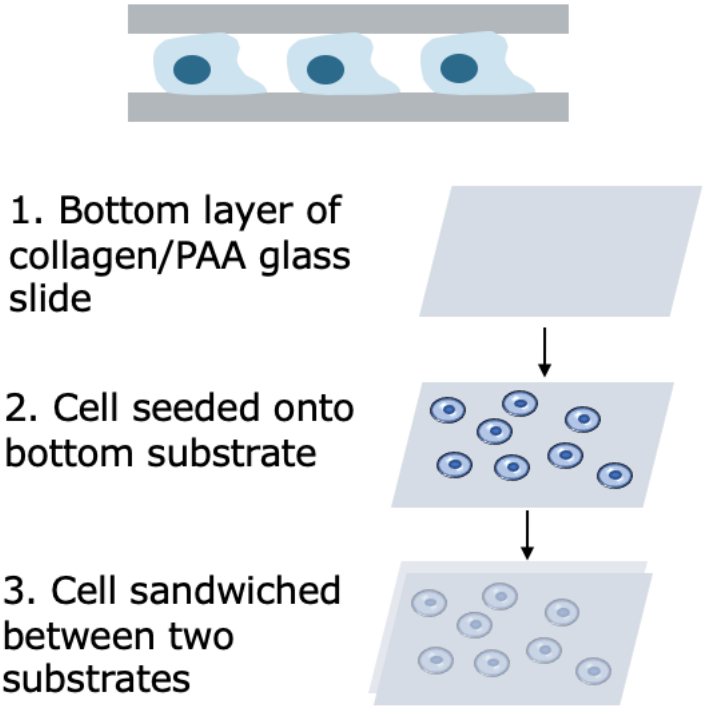


**Figure 6.3:** Cell sandwiched between two PAA/collagen gel coated substrates

6.2.4 Measurement of vertical confinement length

Traction force microscopy (TFM) was performed on an IX3 Olympus microscope (Olympus, PA) with a 40× NA Plan Apo air objective lens (Olympus). Cells were Sandwiched between PAA substrates for 16–24 h. For each cell, a phase contrast image of the cell and a fluorescent image of the beads in the gel substrate were acquired using a QIClick CCD camera (QImaging, BC, Canada) with SlideBook software (Intelligent Imaging Innovations, CO). Because different color of fluorescent beads were coated on top and bottom substrates, by measuring the z plate length of each layer, confinement height can be determined and calculated as about 5 $\mu m$.

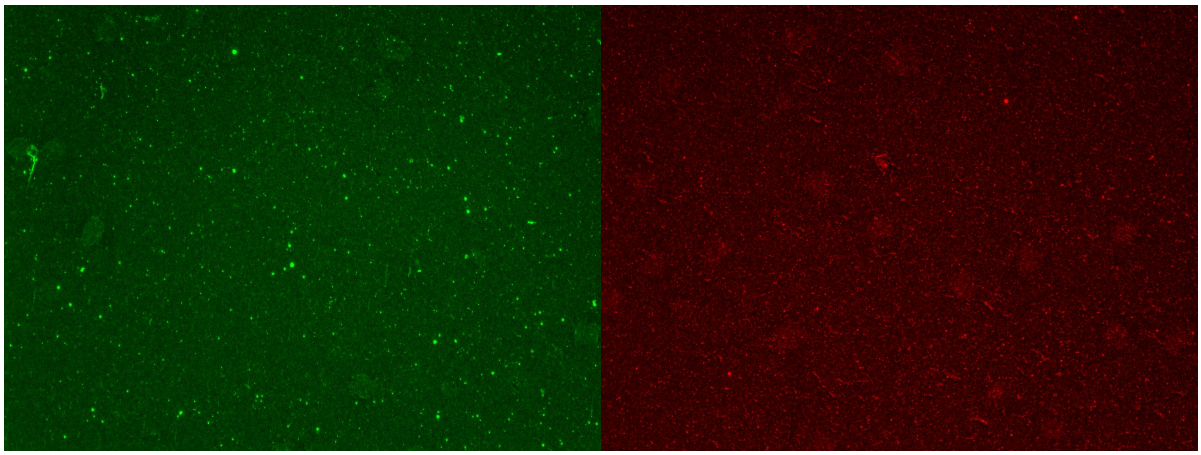

**Figure 6.4:** bottom layer at z=9555.39 (Green) Top layer at z=9560.29 (Red)

6.3 Gene expression in breast cancer cells in response to confinement

Cytokine profiling provides valuable information for inflammatory stimulus, cancer progression and disease diagnosis. Cytokine detection and measurement as biomarker is important for quantitative analysis of small amount of cytokine and cytokine network. The cytokine family includes interleukins(ILs), interferons(IFNs), tumor necrosis factors(TNFs), transforming growth factors(TGFs), mesenchymal growth factors, adipocytokines and hematopoietic growth factors[187]. In-depth knowledge of tumor microenvironment and cancer development have revealed that immune cells can have contrasting effects during interaction with cancer cells[188]. While immune reactions are mediated by cytokines produced by either immune cells or tumor cells, detection of sets of cytokines have drawn researchers interest and provides a platform for cancer immunology therapy. Hematogeneous metastasis can occur via a cascade of circulating tumor cell adhesion events to the endothelial lining of the vasculature, i.e. the metastatic cascade. Interestingly, the pro-inflammatory cytokines IL-6 and TNF-α, which play an important role in potentiating the inflammatory cascade, are significantly elevated in breast cancer patients. Despite their high metastatic potential, human breast carcinoma cells MDA-MB-231 lack interactions with E-selectin functionalized surfaces under physiological shear stresses. We hypothesized that the *in vitro* physical confinement model could induce a phenotypic switch that allows MDA-MB-231 cells to respond to the mechanical stimulus on chip. qPCR assay were utilized to investigate the phenotypic changes of MDA-MB-231 cells with various treatments.

6.3.1 PCR protocol

Thaw the template RNA on ice; the kit components should be immediately placed on ice after thawing at room temperature. Each solution should be vortexed to mix, and centrifuge briefly prior to use.

**Cdna synthesis: Reverse transcription reaction:**

1. Set up the reaction on ice according the following table.

| Reagent | 10 µl Reaction |
|---|---|
| RNA template | x µl (1pg-1µg) [a] |
| 5×EasyQuick RT MasterMix[b] | 2 µl |
| RNase-Free Water | Up to 10 µl |

Note: a. If the total RNA is greater than 1 µg, scale up the reaction system. b. 5×EasyQuick RT MasterMix contains EasyQuick reverse transcriptase, RNase Inhibitor, Random 6 mers, Oligo dT Primer, dNTPs EasyQuick RT Buffer etc.

2. Vortex to mix well; Briefly centrifuge to collect all the solution to the bottom of the tube.
3. Incubate at 37°C for 15 minutes then incubate at 85°C for 5 minutes. Note: a. For downstream regular PCR, incubate at 37°C for 30-50 minutes. b. For templates with complex secondary structure, or high GC content, increase the temperature for reverse transcription to 50°C to increase the reverse transcription efficiency.
4. After the reaction is done, briefly centrifuge, then put on ice. For long time storage, please put it in -20°C.

**Note: for real-time PCR reaction, the volume of reverse transcription product should NOT exceed the 1/10 volume of the total PCR reaction**

**Qpcr with CW0955S FastSYBR Mixture, 5 ml (500 rxns)**

The following protocol is an example of conventional PCR reaction system and condition. The actual protocol should be improved and optimized based on the template, primer structure and the size of the target.

1. PCR reaction system for low Rox:

| Reagent | 20 µl | Final Conc. |
|---|---|---|
| 2× FastSYBR Mixture | 10 µl | 1x |
| Forward Primer, 10 µM | 0.4 µl | 0.2 µM |
| Reverse Primer, 10 µM | 0.4 µl | 0.2 µM |
| DNA template | 1 µl | |
| $ddH_2O$ | Up to 20 µl | |

**Note:**

1) Usually 0.2 µM of primer concentration gives better results, and the final concentration of primers should be between 0.1 and1.0 µM.

2) Usually the amount of DNA template is 10-100 ng for genomic DNA or 1-10 ng for cDNA. Template can be gradient diluted to optimize.

3) The recommended reaction volume is 20 µl, and the reaction volume can also be scaled up or down according to actual experimental requirements.

2. PCR reaction program:

It is recommended to use two-step PCR reaction program. This program uses ABI7500 qPCR machine as an example. If a good result cannot be obtained due to the low Tm of the primers, try a three-step PCR program.

| Procedure | Temperature | Time |
|---|---|---|
| Pre-denaturation | 95°C | 20 sec |
| Denaturation | 95°C | 3 sec |
| Annealing/Extension | 60°C | 30 sec |
| Melting curve analysis | | |
| | 95°C | 15 sec |
| | 60°C | 1 min |
| | 95°C | 15 sec |

| | | |
|---|---|---|
| | 60°C | 15 sec |

**Note: 1**) The annealing temperature should be between 60-64°C. If there is non-specific reaction, increase the annealing temperature.

2) This program uses ABI7500 qPCR machine as an example. The melting curve analysis should be set according to the procedure recommended by qPCR instrument used.

6.3.2 Expression level of IL-6, TNF-a and CSF-1

qRT-PCR analysis was performed to assess Il-6, TNF-a and CSF-1 mRNA expression in MCF-10A and MDA-MB-231 cell. Pro-inflammatory cytokines have been linked to poor prognosis in metastatic breast cancer patients with elevated IL-6 and TNF-α cytokine in their blood plasma. As it is shown in the Figure 6.5 below, we confirmed the higher expression of IL-6 and TNF-a in MDA-MB-231 cells than in MCF-10A cells. Moreover, physical confinement were shown to alter the gene expression of IL-6 and TNF-a in MDA-MB-231 cell line. Elevated level of pro-inflammatory IL-6 and TNF-a expression in MDA-MB-231 cell line after physical confinement treatment may indicate that physical confinement can change the phenotype of cancer cells, which may contribute to the higher metastasis potential of MDA-MB-231.

A

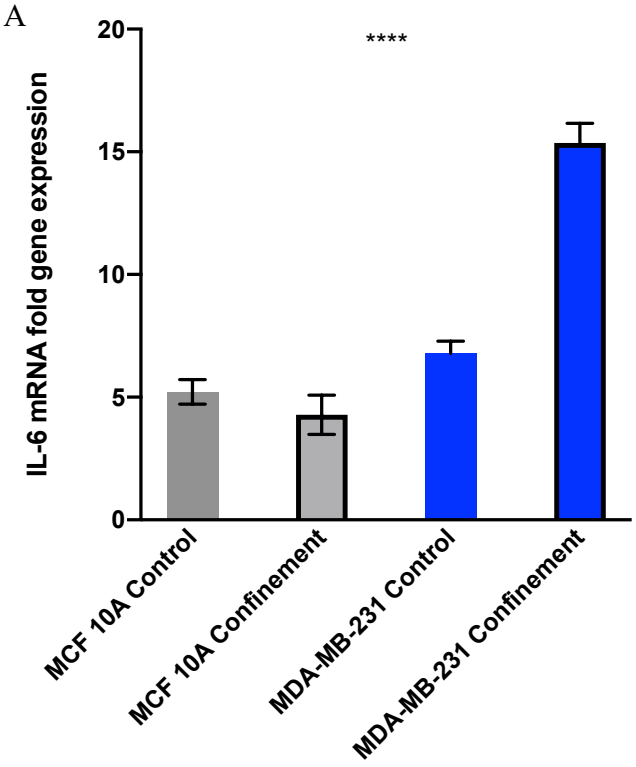
****
IL-6 mRNA fold gene expression
20
15
10
5
0
MCF 10A Control
MCF 10A Confinement
MDA-MB-231 Control
MDA-MB-231 Confinement

B

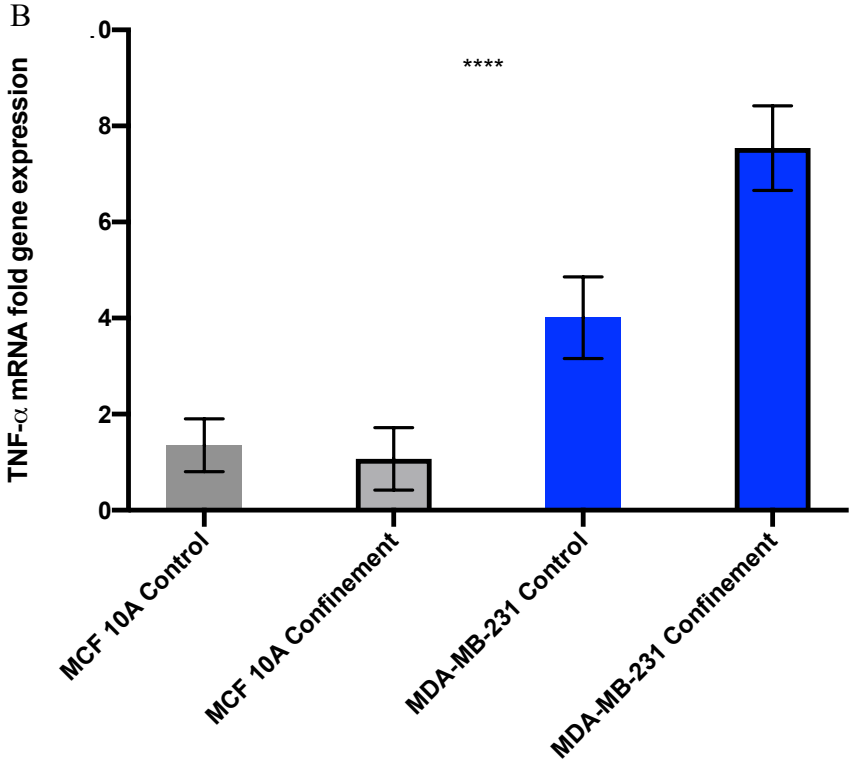
****
TNF-α mRNA fold gene expression
10
8
6
4
2
0
MCF 10A Control
MCF 10A Confinement
MDA-MB-231 Control
MDA-MB-231 Confinement

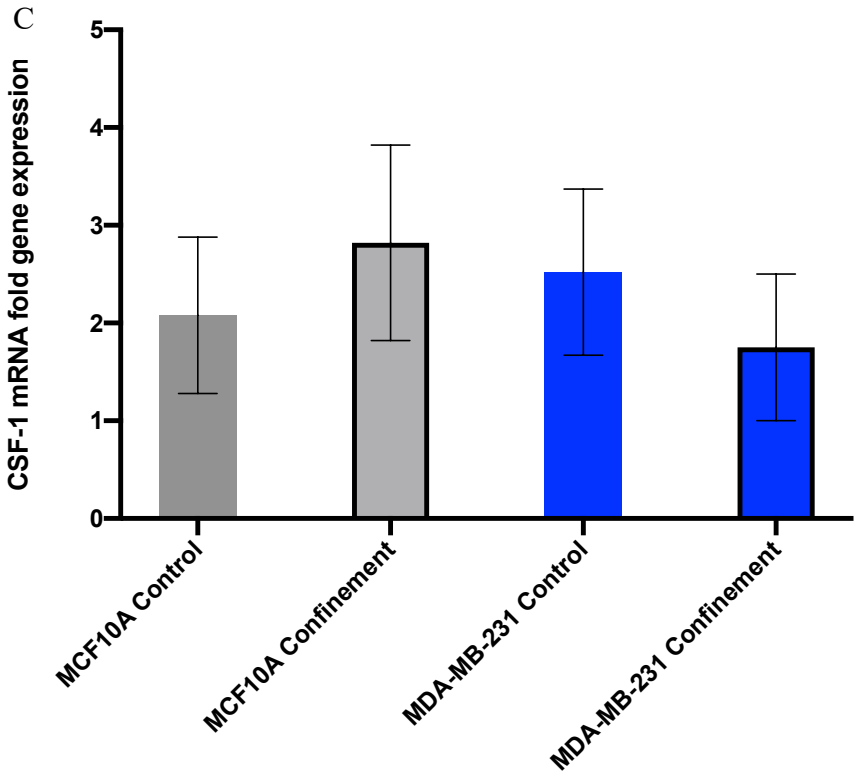


**Figure 6.5:** qPCR analysis of MCF-10A and MDA-MB-231 cells subject to physical confinement (A) IL-6 mRNA fold expression change (B)TNF-a mRNA fold expression change (C) CSF-1 mRNA fold expression change

6.3 MXene/PB/AuNPs based electrochemical immunosensor for IL-6 detection

6.3.1 Synthesis of $V_2AlC$(Mxene), Mxene/PB, Mxene/PB/AuNPs

The MXene were synthesized by immersing the MAX phase powders slowly in a HDPE jar contained an aqueous hydrofluoric acid, HF (48% Macron Fine Chemicals – Avantor Performance Materials, Center Valley, PA, USA) solution with a certain concentration at RT. Then, a Teflon coated magnet was put in the jar and the jar was moved to a stir plate, and stirred at a speed of 400 rpm for a specific time at RT. Afterword, the solution with the reacted powders were moved to centrifuging vials, and centrifuged. The concentrated HF solutions were decanted and fresh deionized (DI) water was added to wash the powders from HF and reaction products, and centrifuged again. The washing step was repeated many times till the pH of the top liquid reached values higher than 4. Finally, the washed powders were vacuum filtered to facilitate drying at RT. The HF concentrations and reaction times were 48% for 92 h, and 30% for 18 h,

for $V_2AlC$ and $Ti_3AlCN$, respectively. Delamination of $V_2AlC$ procedure was followed through experimental part in a paper published by Nanda et al[189].

The in-situ synthesis of $V_2AlC$ (Mxene)/Prussian Blue (PB) is as follows: In a typical procedure, 500 µL delaminated Mxene solution prepared above were mixed with 500 µL 2.5mM $FeCl_3/K_3[Fe(CN)_6]$ solution and stirring for 2 h. Then add 5 µL PDDA in and keep stirring for another 1 h. Remove the supernatant and leave the sediment in tube, and then add 500 µL $H_2O$. Centrifuge and wash 2 times.

Mxene/PB/AuNPs were synthesized by adding 300 µL 0.1% $HAuCl_4$ to Mxene/PB solution and then centrifuge to get the sediment Mxene/PB/AuNPs.

6.3.2 Immunosensing interface for detection of IL-6

Construction of the immobilization process of Il-6 antibody, BSA and IL-6 antigen on AuE was characterized by CV and DPV (Figure 6.6). Figure 6.6B showed the differential pulse voltammograms obtained at bare Au electrode, cystamine dihydrochloride modified AuE, IL-6 Ab fixed on cystamine dihydrochloride modified AuE, BSA filling non-specific binding sites and IL-6 Antigen conjugated electrode. As we can see, the peak current gradually decreased during each immobilization step.

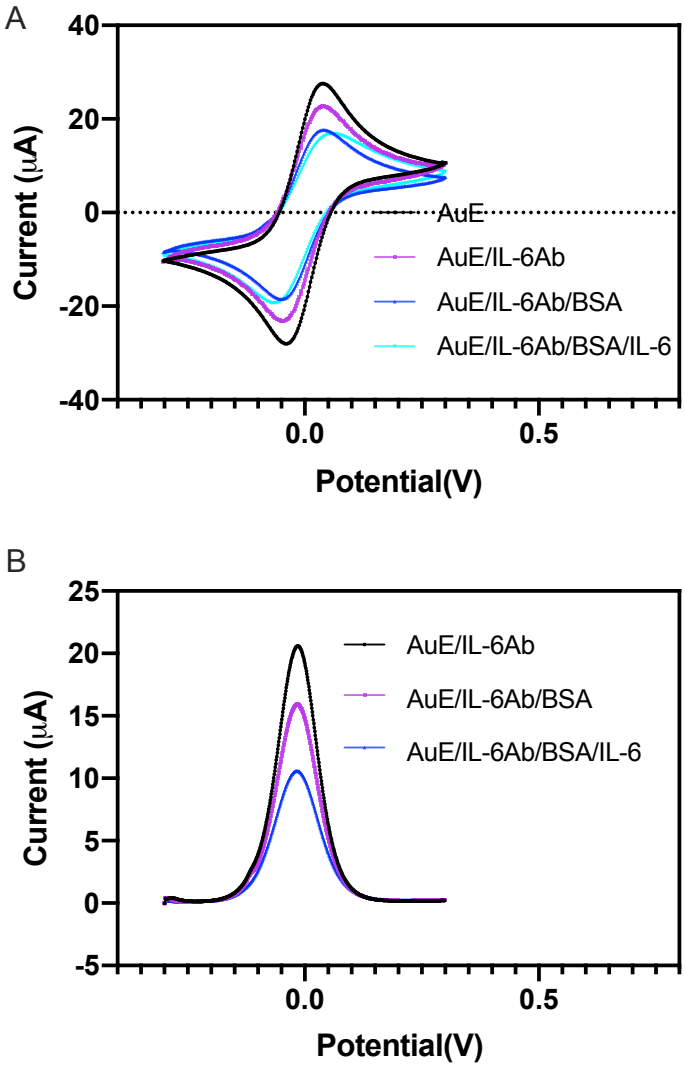


Figure 6.6: (A) CV of AuE immobilization process (B) DPV of AuE immobilization process

6.4 Summary

In summary of this chapter, an in-vitro vertical confinement model was built for cell culture. Followed PCR analysis showed increased mRNA expression level of IL-6 and TNF-a. A electrochemical immunosensor was then developed for detection of IL-6 using Mxene nanomaterial as the probe material.

## CHAPTER 7: Highlights of research, limitations and future outlook

New advancements in nanomaterials, nanofabrication and microfabrication technique have enabled development of biosensor integrated with microfluidic device for point-of-care diagnosis, cancer metastasis study, cancer-on-chip and cancer in vitro detection. Though devices based on electrochemical biosensors rarely have been used in clinical patients, they have shown great potential and achieved great progress. This dissertation provided a focused and systematic way of design and development of biosensor and microfluidic device, aiming to develop a real robust point-of-care devices for future in-vivo study and clinical uses. In this chapter, key achievements of each projects will be highlighted, as well as highlight significant limitations.

Nanomaterial synthesis and usage as the electrode material was shown to promote electrochemical sensor analytical performance. In the non-enzymatic glucose sensor project covered in Chapter 2, Cu-CuO nanoparticles were synthesized by electrodeposition method and act as the electroactive species toward glucose oxidation. The Cu-CuO/TNT electrode based non-enzymatic glucose sensor showed a wide linear detection range between 0.2-80 mM which is much superior to many other glucose sensors. However, a big limitation of non-enzymatic glucose sensor is the alkaline operating conditions in testing which will limit its use in human body. Future research is required to fully understand the sensing mechanisms of different materials and to explore techniques such as 3D printing to produce glucose sensors. Disposable printed electrode for direct electrochemical sensing will help in reducing cost while increasing usage simplicity. It is also foreseeable that the next generation of glucose biosensor will not only to monitor glucose levels but also be able to respond to changing cues, predicting trends and helping in managing glucose levels.

Besides synthesis of nanomaterials, nanostructured surface was shown to increase the sensitivity of the electrode. As discussed in chapter 3, nanostructured PU was fabricated by a rapid prototyping method, which greatly increase the stability of electrode and resolve the challenge of nanomaterials stability issue. The future trends and challenges for disposable biosensor will include: (1) miniaturization and use with portable devices, which may be enable by combining with handheld electrochemical station (2) integration of next generation recognition element such as aptamers and peptides for detecting new targets (3) combining with therapeutic systems, known as theranostics.

Batch fabrication method of electrochemical sensors on PETG substrate was then developed and discussed in chapter 4. Gold sputtering was used to sputter 10 nm Cr and 100 nm Au film on the PETG surface, which achieved fine control of thickness and high repeatability. PETG based electrochemical sensor can serve as future flexible biosensor due to the nature of PETG. The primary challenge is to achieve electrode with high mechanical stability. The relevant field is shifting toward the mass production and industrial manufacturing of electrochemical sensor.

Microfluidic device have emerged as a powerful tool for cell migration and cancer metastasis study. In chapter 5, we designed and fabricated a microfluidic device to mimic the in vivo physical confinement environment and use it for cell migration study. Although this device was developed to only investigate the cell migration behavior under confinement, there are other aspects can be further explored: (1) microfluidic device can be used to study how biochemical or cellular factors affect cell migration or cancer cell invasion. It is capable to study cancer cell migration in response to biochemical gradient or in co-culture with tumor-associated macrophages (2) microfluidic device can be used as "metastasis-on-a-chip" platform for future investigation of cancer extravasation. Multi-organ devices can be developed with multiple cancer cell migration pathways leading to cell cultures of different downstream organs. It can be used to identify metastatic specificity and drug targets and to perform drug screening for personalized medicine. To fully utilize the advantages of the *in vitro* microfluidic device over current *in vivo* systems, these devices should incorporate immune cells, primary human cells and ECM environment. A microfluidic device with the balance between capturing the complexity of the metastatic cascade and ability to be mass produced could revolutionize cancer treatment and could allow drug investigation and screening in a high-throughput approaches for managing cancer metastasis.

In conclusion, future POC diagnosis and cancer metastasis on chip can only be enable by combining the technology advances in material, biosensor and microfluidic device field. The construction of biosensor platforms using the technology of microfluidics allows for a high degree of integration that facilitates per se the development of a compact, small-sized device with all the instrumentation required, built in a portable and manageable format. The various examples presented herein indicate that these device architectures can successfully and efficiently merge chemical and biological elements to produce sensors for reliable high-throughput analyses in almost any operational environmental at acceptable costs. Future

perspectives should focus on bring microfluidic biosensor for application of cancer metastasis on-chip diagnosis and therapeutic treatment.

## References


1. X. Jiang, J. Hu, A. M. Lieber, C. S. Jackan, J. C. Biffinger, L. A. Fitzgerald, B. R. Ringeisen and C. M. Lieber, Nano Letters **14** (11), 6737-6742 (2014).
2. H. Jin, C. Guo, X. Liu, J. Liu, A. Vasileff, Y. Jiao, Y. Zheng and S.-Z. Qiao, Chemical Reviews **118** (13), 6337-6408 (2018).
3. W. Putzbach and N. J. Ronkainen, Sensors **13** (4), 4811-4840 (2013).
4. R. M. Lequin, Clinical Chemistry **51** (12), 2415-2418 (2005).
5. S. Liu, D. Leech and H. Ju, Analytical Letters **36** (1), 1-19 (2003).
6. S. Guo and E. Wang, Analytica Chimica Acta **598** (2), 181-192 (2007).
7. X.-P. Zhao, F.-F. Liu, W.-C. Hu, M. R. Younis, C. Wang and X.-H. Xia, Analytical Chemistry **91** (5), 3582-3589 (2019).
8. I. Álvarez-Martos and E. E. Ferapontova, Analytical Chemistry **88** (7), 3608-3616 (2016).
9. A. M. Oliveira-Brett, J. A. P. Piedade, L. A. Silva and V. C. Diculescu, Analytical Biochemistry **332** (2), 321-329 (2004).
10. H. Suzuki, K. Tabata, Y. Kato-Yamada, H. Noji and S. Takeuchi, Lab on a Chip **4** (5), 502-505 (2004).
11. C. Frantz, K. M. Stewart and V. M. Weaver, Journal of cell science **123** (Pt 24), 4195-4200 (2010).
12. M. J. Bissell and D. Radisky, Nature Reviews Cancer **1** (1), 46-54 (2001).
13. D. Wirtz, K. Konstantopoulos and P. C. Searson, Nature Reviews Cancer **11** (7), 512-522 (2011).
14. A. Berzat and A. Hall, EMBO J **29** (16), 2734-2745 (2010).
15. J. M. Muncie and V. M. Weaver, Curr Top Dev Biol **130**, 1-37 (2018).
16. D. Hoffman-Kim, J. A. Mitchel and R. V. Bellamkonda, Annual review of biomedical engineering **12**, 203-231 (2010).
17. T. N. TruongVo, R. M. Kennedy, H. Chen, A. Chen, A. Berndt, M. Agarwal, L. Zhu, H. Nakshatri, J. Wallace, S. Na, H. Yokota and J. E. Ryu, Journal of Micromechanics and Microengineering **27** (3) (2017).
18. M. W. Tibbitt and K. S. Anseth, Biotechnol Bioeng **103** (4), 655-663 (2009).
19. C. D. Paul, W.-C. Hung, D. Wirtz and K. Konstantopoulos, Annual Review of Biomedical Engineering **18** (1), 159-180 (2016).
20. T. Fujii, Microelectronic Engineering **61-62**, 907-914 (2002).
21. C. Wyatt Shields Iv, C. D. Reyes and G. P. López, Lab on a Chip **15** (5), 1230-1249 (2015).
22. H.-L. Gou, X.-B. Zhang, N. Bao, J.-J. Xu, X.-H. Xia and H.-Y. Chen, Journal of Chromatography A **1218** (33), 5725-5729 (2011).
23. K. Loutherback, J. D'Silva, L. Liu, A. Wu, R. H. Austin and J. C. Sturm, AIP Adv **2** (4), 42107-42107 (2012).
24. W. Zhao, T. Zhu, R. Cheng, Y. Liu, J. He, H. Qiu, L. Wang, T. Nagy, T. D. Querec, E. R. Unger and L. Mao, Advanced Functional Materials **26** (22), 3990-3998 (2016).
25. E. P. Furlani, Journal of Physics D: Applied Physics **40** (5), 1313-1319 (2007).
26. Y. Song, B. Lin, T. Tian, X. Xu, W. Wang, Q. Ruan, J. Guo, Z. Zhu and C. Yang, Analytical Chemistry **91** (1), 388-404 (2019).

27. B. Zribi, E. Roy, A. Pallandre, S. Chebil, M. Koubaa, N. Mejri, H. M. Gomez, C. Sola, H. Korri-Youssoufi and A.-M. Haghiri-Gosnet, Biomicrofluidics **10** (1), 014115 (2016).
28. F. H. Cincotto, E. L. Fava, F. C. Moraes, O. Fatibello-Filho and R. C. Faria, Talanta **195**, 62-68 (2019).
29. L. Li, Y. Wang, L. Pan, Y. Shi, W. Cheng, Y. Shi and G. Yu, Nano Letters **15** (2), 1146-1151 (2015).
30. A. Martín, J. Kim, J. F. Kurniawan, J. R. Sempionatto, J. R. Moreto, G. Tang, A. S. Campbell, A. Shin, M. Y. Lee, X. Liu and J. Wang, ACS Sensors **2** (12), 1860-1868 (2017).
31. S. K. Jha, R. Chand, D. Han, Y.-C. Jang, G.-S. Ra, J. S. Kim, B.-H. Nahm and Y.-S. Kim, Lab on a Chip **12** (21), 4455-4464 (2012).
32. A. Koh, D. Kang, Y. Xue, S. Lee, R. M. Pielak, J. Kim, T. Hwang, S. Min, A. Banks, P. Bastien, M. C. Manco, L. Wang, K. R. Ammann, K.-I. Jang, P. Won, S. Han, R. Ghaffari, U. Paik, M. J. Slepian, G. Balooch, Y. Huang and J. A. Rogers, Science Translational Medicine **8** (366), 366ra165-366ra165 (2016).
33. A. Heller and B. Feldman, Chemical Reviews **108** (7), 2482-2505 (2008).
34. M. Butler, Applied Microbiology and Biotechnology **68** (3), 283-291 (2005).
35. C. C. Adley, Foods **3** (3), 491-510 (2014).
36. P. Zhang, D. Sun, A. Cho, S. Weon, S. Lee, J. Lee, J. W. Han, D.-P. Kim and W. Choi, Nature Communications **10** (1), 940 (2019).
37. A. Ahmadalinezhad, S. Chatterjee and A. Chen, Electrochimica Acta **112**, 927-932 (2013).
38. X. Zhou, X. Zheng, R. Lv, K. Dexian and Q. Li, Electrochimica Acta **107**, 164-169 (2013).
39. S.-L. Zhong, J. Zhuang, D.-P. Yang and D. Tang, Biosensors and Bioelectronics **96**, 26-32 (2017).
40. N. Pal, S. Banerjee and A. Bhaumik, Journal of Colloid and Interface Science **516**, 121-127 (2018).
41. J. Luo, S. Jiang, H. Zhang, J. Jiang and X. Liu, Analytica Chimica Acta **709**, 47-53 (2012).
42. H. Gao, F. Xiao, C. B. Ching and H. Duan, ACS Applied Materials & Interfaces **3** (8), 3049-3057 (2011).
43. J. Ryu, K. Kim, H.-S. Kim, H. T. Hahn and D. Lashmore, Biosensors and Bioelectronics **26** (2), 602-607 (2010).
44. A. S. Fauci and D. M. Morens, New England Journal of Medicine **366** (5), 454-461 (2012).
45. R. França, C. Da Silva and S. De Paula, European journal of clinical microbiology & infectious diseases **32** (6), 723-728 (2013).
46. D. Mabey, R. W. Peeling, A. Ustianowski and M. D. Perkins, Nature Reviews Microbiology **2** (3), 231 (2004).
47. M. L. Sin, K. E. Mach, P. K. Wong and J. C. Liao, Expert review of molecular diagnostics **14** (2), 225-244 (2014).
48. F. Cui, Z. Zhou and H. S. Zhou, Journal of The Electrochemical Society **167** (3) (2020).
49. L. Chen, S. Xu and J. Li, Chemical Society Reviews **40** (5), 2922-2942 (2011).
50. D. Yongabi, M. Khorshid, P. Losada-Pérez, K. Eersels, O. Deschaume, J. D'Haen, C. Bartic, J. Hooyberghs, R. Thoelen, M. Wübbenhorst and P. Wagner, Sensors and Actuators B: Chemical **255**, 907-917 (2018).

51. B. van Grinsven, K. Eersels, O. Akkermans, S. Ellermann, A. Kordek, M. Peeters, O. Deschaume, C. Bartic, H. Diliën, E. Steen Redeker, P. Wagner and T. J. Cleij, ACS Sensors **1** (9), 1140-1147 (2016).
52. M. Cieplak and W. Kutner, Trends in Biotechnology **34** (11), 922-941 (2016).
53. A. A. Lahcen and A. Amine, Electroanalysis **31** (2), 188-201 (2019).
54. K. Eersels, P. Lieberzeit and P. Wagner, ACS sensors **1** (10), 1171-1187 (2016).
55. N. R. Pollock, Journal of clinical microbiology **54** (2), 259-264 (2016).
56. S. S. Magill, J. R. Edwards, W. Bamberg, Z. G. Beldavs, G. Dumyati, M. A. Kainer, R. Lynfield, M. Maloney, L. McAllister-Hollod, J. Nadle, S. M. Ray, D. L. Thompson, L. E. Wilson and S. K. Fridkin, New England Journal of Medicine **370** (13), 1198-1208 (2014).
57. E. Saade, A. Deshpande, S. Kundrapu, V. C. K. Sunkesula, D. M. Guerrero, L. A. Jury and C. J. Donskey, Current Medical Research and Opinion **29** (8), 985-988 (2013).
58. F. Barbut, L. Surgers, C. Eckert, B. Visseaux, M. Cuingnet, C. Mesquita, N. Pradier, A. Thiriez, N. Ait-Ammar, A. Aifaoui, E. Grandsire and V. Lalande, Clinical Microbiology and Infection **20** (2), 136-144 (2014).
59. S. A. Kuehne, S. T. Cartman, J. T. Heap, M. L. Kelly, A. Cockayne and N. P. Minton, Nature **467**, 711 (2010).
60. D. Lyras, J. R. O'Connor, P. M. Howarth, S. P. Sambol, G. P. Carter, T. Phumoonna, R. Poon, V. Adams, G. Vedantam, S. Johnson, D. N. Gerding and J. I. Rood, Nature **458**, 1176 (2009).
61. C. Gateau, J. Couturier, J. Coia and F. Barbut, Clinical Microbiology and Infection **24** (5), 463-468 (2018).
62. M. J. T. Crobach, T. Planche, C. Eckert, F. Barbut, E. M. Terveer, O. M. Dekkers, M. H. Wilcox and E. J. Kuijper, Clinical Microbiology and Infection **22**, S63-S81 (2016).
63. L. Song, M. Zhao, D. C. Duffy, J. Hansen, K. Shields, M. Wungjiranirun, X. Chen, H. Xu, D. A. Leffler, S. P. Sambol, D. N. Gerding, C. P. Kelly and N. R. Pollock, Journal of clinical microbiology **53** (10), 3204-3212 (2015).
64. J. Sandlund, A. Bartolome, A. Almazan, S. Tam, S. Biscocho, S. Abusali, J. J. Bishop, N. Nolan, J. Estis, J. Todd, S. Young, F. Senchyna and N. Banaei, Journal of clinical microbiology **56** (11), e00908-00918 (2018).
65. A. Syahir, K. Usui, K.-Y. Tomizaki, K. Kajikawa and H. Mihara, Microarrays (Basel) **4** (2), 228-244 (2015).
66. Y.-S. Fang, S.-Y. Chen, X.-J. Huang, L.-S. Wang, H.-Y. Wang and J.-F. Wang, Biosensors and Bioelectronics **53**, 238-244 (2014).
67. S. Han, W. Liu, S. Yang and R. Wang, ACS Omega **4** (6), 11025-11031 (2019).
68. H. M. Moghaddam, H. Beitollahi, G. Dehghannoudeh and H. Forootanfar, Journal of The Electrochemical Society **164** (7), B372-B376 (2017).
69. H. Subak and D. Ozkan-Ariksoysal, Sensors and Actuators B: Chemical **263**, 196-207 (2018).
70. M. Thangamuthu, C. Santschi and O. J. F. Martin, Biosensors **8** (2), 34 (2018).
71. S. Kempahanumakkagari, K. Vellingiri, A. Deep, E. E. Kwon, N. Bolan and K.-H. Kim, Coordination Chemistry Reviews **357**, 105-129 (2018).
72. N. Baig, M. Sajid and T. A. Saleh, TrAC Trends in Analytical Chemistry **111**, 47-61 (2019).

73. H. Huo, M. Shen, S. M. Ebstein and H. Guthermann, J Mass Spectrom **46** (9), 859-864 (2011).
74. M. Y. Shen, C. H. Crouch, J. E. Carey and E. Mazur, Applied Physics Letters **85** (23), 5694-5696 (2004).
75. D. Qin, Y. Xia and G. M. Whitesides, Nat Protoc **5** (3), 491-502 (2010).
76. Q. Xu, B. T. Mayers, M. Lahav, D. V. Vezenov and G. M. Whitesides, Journal of the American Chemical Society **127** (3), 854-855 (2005).
77. R. Elshafey, A. C. Tavares, M. Siaj and M. Zourob, Biosensors and Bioelectronics **50**, 143-149 (2013).
78. Z. Zhu, L. Shi, H. Feng and H. Susan Zhou, Bioelectrochemistry **101**, 153-158 (2015).
79. J. Yang and R. A. Weinberg, Developmental Cell **14** (6), 818-829 (2008).
80. R. Horwitz and D. Webb, Current Biology **13** (19), R756-R759 (2003).
81. G. P. Gupta and J. Massagué, Cell **127** (4), 679-695 (2006).
82. P. Friedl and S. Alexander, Cell **147** (5), 992-1009 (2011).
83. N. Mor-Vaknin, A. Punturieri, K. Sitwala and D. M. Markovitz, Nature cell biology **5** (1), 59-63 (2003).
84. A. Satelli and S. Li, Cellular and molecular life sciences **68** (18), 3033-3046 (2011).
85. M. G. Mendez, S. I. Kojima and R. D. Goldman, The FASEB Journal **24** (6), 1838-1851 (2010).
86. B. Eckes, D. Dogic, E. Colucci-Guyon, N. Wang, A. Maniotis, D. Ingber, A. Merckling, F. Langa, M. Aumailley, A. Delouvee, V. Koteliansky, C. Babinet and T. Krieg, Journal of Cell Science **111** (13), 1897-1907 (1998).
87. B. Eckes, E. Colucci-Guyon, H. Smola, S. Nodder, C. Babinet, T. Krieg and P. Martin, Journal of Cell Science **113** (13), 2455-2462 (2000).
88. B. T. Helfand, M. G. Mendez, S. N. P. Murthy, D. K. Shumaker, B. Grin, S. Mahammad, U. Aebi, T. Wedig, Y. I. Wu, K. M. Hahn, M. Inagaki, H. Herrmann and R. D. Goldman, Molecular Biology of the Cell **22** (8), 1274-1289 (2011).
89. K. Vuoriluoto, H. Haugen, S. Kiviluoto, J. P. Mpindi, J. Nevo, C. Gjerdrum, C. Tiron, J. B. Lorens and J. Ivaska, Oncogene **30** (12), 1436-1448 (2011).
90. R. J. Paccione, H. Miyazaki, V. Patel, A. Waseem, J. S. Gutkind, Z. E. Zehner and W. A. Yeudall, Molecular Cancer Therapeutics **7** (9), 2894-2903 (2008).
91. M. G. Mendez, S.-I. Kojima and R. D. Goldman, FASEB J **24** (6), 1838-1851 (2010).
92. Y. Zhao, Q. Yan, X. Long, X. Chen and Y. Wang, Cell Biochemistry and Function: Cellular biochemistry and its modulation by active agents or disease **26** (5), 571-577 (2008).
93. Y. Messica, A. Laser-Azogui, T. Volberg, Y. Elisha, K. Lysakovskaia, R. Eils, E. Gladilin, B. Geiger and R. Beck, Nano letters **17** (11), 6941-6948 (2017).
94. E. Olaso, J.-P. Labrador, L. Wang, K. Ikeda, F. J. Eng, R. Klein, D. H. Lovett, H. C. Lin and S. L. Friedman, Journal of Biological Chemistry **277** (5), 3606-3613 (2002).
95. W. Li, J. Fan, M. Chen, S. Guan, D. Sawcer, G. M. Bokoch and D. T. Woodley, Molecular biology of the cell **15** (1), 294-309 (2004).
96. R. Ananthakrishnan and A. Ehrlicher, Int J Biol Sci **3** (5), 303-317 (2007).
97. T. Svitkina, Cold Spring Harb Perspect Biol **10** (1), a018267 (2018).
98. R. J. Petrie and K. M. Yamada, Journal of cell science **125** (Pt 24), 5917-5926 (2012).

99. K. M. Yamada and M. Sixt, Nature Reviews Molecular Cell Biology **20** (12), 738-752 (2019).
100. D. Irimia and M. Toner, Integrative Biology **1** (8-9), 506-512 (2009).
101. M. Mak and D. Erickson, Lab on a Chip **14** (5), 964-971 (2014).
102. J. Schwarz, V. Bierbaum, J. Merrin, T. Frank, R. Hauschild, T. Bollenbach, S. Tay, M. Sixt and M. Mehling, Scientific Reports **6** (1), 36440 (2016).
103. J. Li, L. Zhu, M. Zhang and F. Lin, Biomicrofluidics **6** (2), 24121-2412113 (2012).
104. A. Kumar and G. M. Whitesides, Applied Physics Letters **63** (14), 2002-2004 (1993).
105. Y. Xia, J. J. McClelland, R. Gupta, D. Qin, X.-M. Zhao, L. L. Sohn, R. J. Celotta and G. M. Whitesides, Advanced Materials **9** (2), 147-149 (1997).
106. X.-M. Zhao, Y. Xia and G. M. Whitesides, Advanced Materials **8** (10), 837-840 (1996).
107. E. Kim, Y. Xia, X.-M. Zhao and G. M. Whitesides, Advanced Materials **9**, 651-654 (1997).
108. J. A. Rogers, K. E. Paul, R. J. Jackman and G. M. Whitesides, Applied Physics Letters **70** (20), 2658-2660 (1997).
109. S. Jeon, E. Menard, J.-U. Park, J. Maria, M. Meitl, J. Zaumseil and J. A. Rogers, Advanced Materials **16** (15), 1369-1373 (2004).
110. W. R. Childs and R. G. Nuzzo, Journal of the American Chemical Society **124** (45), 13583-13596 (2002).
111. W. Zhang, D. S. Choi, Y. H. Nguyen, J. Chang and L. Qin, Scientific Reports **3** (1), 2332 (2013).
112. M. Nishikawa, T. Yamamoto, N. Kojima, K. Kikuo, T. Fujii and Y. Sakai, Biotechnol Bioeng **99** (6), 1472-1481 (2008).
113. J. Jacobelli, R. S. Friedman, M. A. Conti, A.-M. Lennon-Dumenil, M. Piel, C. M. Sorensen, R. S. Adelstein and M. F. Krummel, Nature Immunology **11** (10), 953-961 (2010).
114. A. W. Holle, N. Govindan Kutty Devi, K. Clar, A. Fan, T. Saif, R. Kemkemer and J. P. Spatz, Nano letters **19** (4), 2280-2290 (2019).
115. R. J. Petrie, N. Gavara, R. S. Chadwick and K. M. Yamada, J Cell Biol **197** (3), 439-455 (2012).
116. B. Chen, G. Kumar, C. C. Co and C.-C. Ho, Scientific Reports **3** (1), 2827 (2013).
117. S. Munevar, Y. Wang and M. Dembo, Biophysical journal **80** (4), 1744-1757 (2001).
118. S. Munevar, Y.-l. Wang and M. Dembo, Molecular Biology of the Cell **12** (12), 3947-3954 (2001).
119. J. B. Bard and E. D. Hay, The Journal of cell biology **67** (2PT.1), 400-418 (1975).
120. J. T. Parsons, A. R. Horwitz and M. A. Schwartz, Nature Reviews Molecular Cell Biology **11** (9), 633-643 (2010).
121. F. Grinnell and W. M. Petroll, Annual Review of Cell and Developmental Biology **26** (1), 335-361 (2010).
122. F. Cui, Z. Zhou and H. S. Zhou, Journal of The Electrochemical Society **167** (3), 037525 (2019).
123. G.-P. Nikoleli, C. G. Siontorou, D. P. Nikolelis, S. Bratakou, S. Karapetis and N. Tzamtzis, in *Nanotechnology and Biosensors* (Elsevier, 2018), pp. 375-394.
124. K. Lee, T. Yoon, H.-s. Yang, S. Cha, Y.-P. Cheon, L. Kashefi-Kheyrabadi and H.-I. Jung, Lab on a Chip (2020).

125. Y. Wang, J. Luo, J. Liu, S. Sun, Y. Xiong, Y. Ma, S. Yan, Y. Yang, H. Yin and X. Cai, Biosensors and Bioelectronics **136**, 84-90 (2019).
126. A. Fernández-la-Villa, D. F. Pozo-Ayuso and M. Castaño-Álvarez, Current Opinion in Electrochemistry **15**, 175-185 (2019).
127. E. L. Fava, T. A. Silva, T. M. d. Prado, F. C. d. Moraes, R. C. Faria and O. Fatibello-Filho, Talanta **203**, 280-286 (2019).
128. R. O. Rodrigues, R. Lima, H. T. Gomes and A. M. Silva, U. Porto Journal of Engineering **1** (1), 67-79 (2015).
129. I. G. Kim, S. Y. Hong, B. O. Park, H. J. Choi and J. H. Lee, Journal of Macromolecular Science, Part B **51** (4), 798-806 (2012).
130. Q. Shi, R. Xiao, H. Yang and D. Lei, Polymer-Plastics Technology and Materials **59** (8), 835-846 (2020).
131. F. Cui, H. Jafarishad, Z. Zhou, J. Chen, J. Shao, Q. Wen, Y. Liu and H. S. Zhou, Biosensors and Bioelectronics **167**, 112521 (2020).
132. L. Liu, Y. Xu, F. Cui, Y. Xia, L. Chen, X. Mou and J. Lv, Biosensors and Bioelectronics **112**, 86-92 (2018).
133. R. Wang, Y. Xu, H. Liu, J. Peng, J. Irudayaraj and F. Cui, Biomedical microdevices **19** (2), 34 (2017).
134. B. Cheng, M. Lin, G. Huang, Y. Li, B. Ji, G. M. Genin, V. S. Deshpande, T. J. Lu and F. Xu, Physics of Life Reviews **22-23**, 88-119 (2017).
135. K. A. Jansen, P. Atherton and C. Ballestrem, Seminars in Cell & Developmental Biology **71**, 75-83 (2017).
136. V. T. Turitto, Prog Hemost Thromb **6**, 139-177 (1982).
137. C. Zhu, T. Yago, J. Lou, V. I. Zarnitsyna and R. P. McEver, Ann Biomed Eng **36** (4), 604-621 (2008).
138. M. Milosevic, A. Fyles, D. Hedley, M. Pintilie, W. Levin, L. Manchul and R. Hill, Cancer Research **61** (17), 6400-6405 (2001).
139. C.-H. Heldin, K. Rubin, K. Pietras and A. Östman, Nature Reviews Cancer **4** (10), 806-813 (2004).
140. S. Ferretti, P. R. Allegrini, M. M. Becquet and P. M. McSheehy, Neoplasia **11** (9), 874-881 (2009).
141. C. G. Willett, Y. Boucher, E. di Tomaso, D. G. Duda, L. L. Munn, R. T. Tong, D. C. Chung, D. V. Sahani, S. P. Kalva, S. V. Kozin, M. Mino, K. S. Cohen, D. T. Scadden, A. C. Hartford, A. J. Fischman, J. W. Clark, D. P. Ryan, A. X. Zhu, L. S. Blaszkowsky, H. X. Chen, P. C. Shellito, G. Y. Lauwers and R. K. Jain, Nature Medicine **10** (2), 145-147 (2004).
142. A. G. Taghian, R. Abi-Raad, S. I. Assaad, A. Casty, M. Ancukiewicz, E. Yeh, P. Molokhia, K. Attia, T. Sullivan, I. Kuter, Y. Boucher and S. N. Powell, Journal of Clinical Oncology **23** (9), 1951-1961 (2005).
143. R. K. Jain, Cancer Research **47** (12), 3039-3051 (1987).
144. C. P. Ng, B. Hinz and M. A. Swartz, Journal of Cell Science **118** (20), 4731-4739 (2005).
145. J. Ahamed, N. Burg, K. Yoshinaga, C. A. Janczak, D. B. Rifkin and B. S. Coller, Blood **112** (9), 3650-3660 (2008).
146. Z.-D. Shi, X.-Y. Ji, H. Qazi and J. M. Tarbell, American Journal of Physiology-Heart and Circulatory Physiology **297** (4), H1225-H1234 (2009).

147. J. D. Shields, M. E. Fleury, C. Yong, A. A. Tomei, G. J. Randolph and M. A. Swartz, Cancer Cell **11** (6), 526-538 (2007).
148. A. C. Shieh, H. A. Rozansky, B. Hinz and M. A. Swartz, Cancer Research **71** (3), 790-800 (2011).
149. J. M. Munson, R. V. Bellamkonda and M. A. Swartz, Cancer Research **73** (5), 1536-1546 (2013).
150. R. Li, J. C. Serrano, H. Xing, T. A. Lee, H. Azizgolshani, M. Zaman and R. D. Kamm, Molecular Biology of the Cell **29** (16), 1927-1940 (2018).
151. P. A. Fasching, K. Heusinger, C. R. Loehberg, E. Wenkel, M. P. Lux, M. Schrauder, T. Koscheck, W. Bautz, R. Schulz-Wendtland, M. W. Beckmann and M. R. Bani, Eur J Radiol **60** (3), 398-404 (2006).
152. C. Voutouri, F. Mpekris, P. Papageorgis, A. D. Odysseos and T. Stylianopoulos, PLOS ONE **9** (8), e104717 (2014).
153. K. R. Levental, H. Yu, L. Kass, J. N. Lakins, M. Egeblad, J. T. Erler, S. F. T. Fong, K. Csiszar, A. Giaccia, W. Weninger, M. Yamauchi, D. L. Gasser and V. M. Weaver, Cell **139** (5), 891-906 (2009).
154. M. W. Pickup, H. Laklai, I. Acerbi, P. Owens, A. E. Gorska, A. Chytil, M. Aakre, V. M. Weaver and H. L. Moses, Cancer Research **73** (17), 5336-5346 (2013).
155. K. Esbona, D. Inman, S. Saha, J. Jeffery, P. Schedin, L. Wilke and P. Keely, Breast Cancer Research **18** (1), 35 (2016).
156. S. C. Wei, L. Fattet, J. H. Tsai, Y. Guo, V. H. Pai, H. E. Majeski, A. C. Chen, R. L. Sah, S. S. Taylor, A. J. Engler and J. Yang, Nature Cell Biology **17** (5), 678-688 (2015).
157. J. K. Mouw, Y. Yui, L. Damiano, R. O. Bainer, J. N. Lakins, I. Acerbi, G. Ou, A. C. Wijekoon, K. R. Levental, P. M. Gilbert, E. S. Hwang, Y. Y. Chen and V. M. Weaver, Nat Med **20** (4), 360-367 (2014).
158. A. J. Rice, E. Cortes, D. Lachowski, B. C. H. Cheung, S. A. Karim, J. P. Morton and A. del Río Hernández, Oncogenesis **6** (7), e352-e352 (2017).
159. K. R. Levental, H. Yu, L. Kass, J. N. Lakins, M. Egeblad, J. T. Erler, S. F. Fong, K. Csiszar, A. Giaccia, W. Weninger, M. Yamauchi, D. L. Gasser and V. M. Weaver, Cell **139** (5), 891-906 (2009).
160. X. Yang, S. K. Sarvestani, S. Moeinzadeh, X. He and E. Jabbari, Tissue Eng Part A **19** (5-6), 669-684 (2013).
161. A. M. Baker, D. Bird, G. Lang, T. R. Cox and J. T. Erler, Oncogene **32** (14), 1863-1868 (2013).
162. J. Swift and D. E. Discher, J Cell Sci **127** (Pt 14), 3005-3015 (2014).
163. B. Geiger, J. P. Spatz and A. D. Bershadsky, Nat Rev Mol Cell Biol **10** (1), 21-33 (2009).
164. Biophysics Journal **79(1): 144–152.** (2000).
165. T. Yeung, P. C. Georges, L. A. Flanagan, B. Marg, M. Ortiz, M. Funaki, N. Zahir, W. Ming, V. Weaver and P. A. Janmey, Cell Motility **60** (1), 24-34 (2005).
166. M. T. Ho Thanh, W. Linthicum, S. Ambady and Q. Wen, Bulletin of the American Physical Society **62** (2017).
167. .
168. K. Wolf, S. Alexander, V. Schacht, L. M. Coussens, U. H. von Andrian, J. van Rheenen, E. Deryugina and P. Friedl, Semin Cell Dev Biol **20** (8), 931-941 (2009).

169. E. Sahai, J. Wyckoff, U. Philippar, J. E. Segall, F. Gertler and J. Condeelis, BMC Biotechnology **5** (1), 14 (2005).
170. A. F. Chambers, A. C. Groom and I. C. MacDonald, Nature Reviews Cancer **2** (8), 563-572 (2002).
171. V. Montana and H. Sontheimer, The Journal of Neuroscience **31** (13), 4858-4867 (2011).
172. J. Chen, Renée M. McKay and Luis F. Parada, Cell **149** (1), 36-47 (2012).
173. S. Watkins and H. Sontheimer, The Journal of Neuroscience **31** (47), 17250-17259 (2011).
174. K. Yamauchi, M. Yang, P. Jiang, N. Yamamoto, M. Xu, Y. Amoh, K. Tsuji, M. Bouvet, H. Tsuchiya, K. Tomita, A. R. Moossa and R. M. Hoffman, Cancer Research **65** (10), 4246-4252 (2005).
175. W. C. Hung, J. R. Yang, C. L. Yankaskas, B. S. Wong, P. H. Wu, C. Pardo-Pastor, S. A. Serra, M. J. Chiang, Z. Gu, D. Wirtz, M. A. Valverde, J. T. Yang, J. Zhang and K. Konstantopoulos, Cell Rep **15** (7), 1430-1441 (2016).
176. C. M. Denais, Gilbert, R. M., Isermann, P., McGregor, A. L., te Lindert, M., Weigelin, B., Davidson, P. M., Friedl, P., Wolf, K., & Lammerding, J. , Science **352(6283), 353–358** (2016).
177. M. Raab, M. Gentili, H. de Belly, H.-R. Thiam, P. Vargas, A. J. Jimenez, F. Lautenschlaeger, R. Voituriez, A.-M. Lennon-Duménil, N. Manel and M. Piel, Science **352** (6283), 359-362 (2016).
178. J. Swift, I. L. Ivanovska, A. Buxboim, T. Harada, P. C. Dingal, J. Pinter, J. D. Pajerowski, K. R. Spinler, J. W. Shin, M. Tewari, F. Rehfeldt, D. W. Speicher and D. E. Discher, Science **341** (6149), 1240104 (2013).
179. M. Tozluoglu, A. L. Tournier, R. P. Jenkins, S. Hooper, P. A. Bates and E. Sahai, Nat Cell Biol **15** (7), 751-762 (2013).
180. P. S. Raman, C. D. Paul, K. M. Stroka and K. Konstantopoulos, Lab Chip **13** (23), 4599-4607 (2013).
181. M. D. Welch, Cell **160** (4), 581-582 (2015).
182. W.-C. Hung, S.-H. Chen, C. D. Paul, K. M. Stroka, Y.-C. Lo, J. T. Yang and K. Konstantopoulos, Journal of Cell Biology **202** (5), 807-824 (2013).
183. W.-C. Hung, J. R. Yang, C. L. Yankaskas, B. S. Wong, P.-H. Wu, C. Pardo-Pastor, S. A. Serra, M.-J. Chiang, Z. Gu, D. Wirtz, M. A. Valverde, J. T. Yang, J. Zhang and K. Konstantopoulos, Cell Reports **15** (7), 1430-1441 (2016).
184. Y.-J. Liu, M. Le Berre, F. Lautenschlaeger, P. Maiuri, A. Callan-Jones, M. Heuzé, T. Takaki, R. Voituriez and M. Piel, Cell **160** (4), 659-672 (2015).
185. Y. J. Liu, M. Le Berre, F. Lautenschlaeger, P. Maiuri, A. Callan-Jones, M. Heuze, T. Takaki, R. Voituriez and M. Piel, Cell **160** (4), 659-672 (2015).
186. S. Wong, W.-h. Guo, I. Hoffecker and Y.-l. Wang, in *Methods in Cell Biology*, edited by M. Piel and M. Théry (Academic Press, 2014), Vol. 121, pp. 3-15.
187. J. A. Owen, J. Punt and S. A. Stranford, *Kuby immunology*. (WH Freeman New York, NY, USA:, 2013).
188. D. G. DeNardo and L. M. Coussens, Breast Cancer Research **9** (4), 212 (2007).
189. M. Naguib, R. R. Unocic, B. L. Armstrong and J. Nanda, Dalton Transactions **44** (20), 9353-9358 (2015).